DEVELOPMENT AND CHARACTERIZATION OF ALL SOLID-STATE LI-ION BATTERIES

PhD. Thesis

Kamil Burak DERMENCİ

Eskişehir 2018

DEVELOPMENT AND CHARACTERIZATION OF ALL SOLID-STATE LI-ION BATTERIES

Kamil Burak DERMENCİ

PhD THESIS

Programme in Materials Science and Engineering
Supervisor: Prof. Dr. Servet TURAN

Eskişehir
Anadolu University
Graduate School of Sciences
August 2018

FINAL APPROVAL FOR THESIS

This thesis titled “Development and Characterization of All-Solid State Li-ion Batteries” has been prepared and submitted by Kamil Burak DERMENCİ in partial fullfillment of the requirements in “Anadolu University Directive on Graduate Education and Examination” for the Degree of Doctor of Philosophy (PhD) in Material Science and Engineering Department has been examined and approved on 08/08/2018.

Committee Members	**Title Name Surname**	**Signature**
Member (Supervisor)	: Prof. Dr. Servet TURAN	.....
Member	: Prof. Dr. Ender SUVACI	.....
Member	: Prof. Dr. M. Kadri AYDINOL	.....
Member	: Prof. Dr. Tayfur ÖZTÜRK	.....
Member	: Prof. Dr. Sebahattin GÜRMEN	.....

Prof. Dr. Ersin YÜCEL

Director of Graduate School of Sciences

ABSTRACT

DEVELOPMENT AND CHARACTERIZATION OF ALL SOLID-STATE LITHIUM ION BATTERIES

Kamil Burak DERMENCİ

Department of Materials Science and Engineering
Anadolu University, Graduate School of Sciences, August 2018

Supervisor: Prof. Dr. Servet TURAN

Garnet type $Li_7La_3Zr_2O_{12}$ (LLZO) solid electrolytes are considered as a potential candidate for replacing traditional organic electrolytes. However, their performance is not yet approaching organic-based liquid electrolytes. The studies on the performance enhancement have focused more on crystal chemistry and lithium kinetics, but not enough studies were carried out to elucidate sintering behavior. The dissertation covers LLZO synthesis conditions in terms of Al content, heating rate and precursor type. Then, a potential sintering mechanism related to sintering temperature is introduced. Li detection in electron microscopy techniques and air stability of the LLZO samples are discussed by using ToF-SIMS attached FIB-SEM. In the Citrate-Nitrate LLZO synthesis, the effect of Zirconium source and anionic species on the cubic phase stabilization of LLZO is covered.

The thermodynamically favored precursors are also determined and the impurities in the structure have been successfully determined with the use of high-sensitivity Lithium maps in LLZO by using ToF-SIMS attached to Xe ion-source FIB-SEM. In Citrate-Nitrate synthesis, the negative influence of nitrate ions on cubic phase stabilization of LLZO is also for the first time shown. The highest bulk conductivity, 0.211 mS/cm, is reached by solid-state synthesized LLZO sintered at 1200 °C for 12 hours.

Keywords: Solid electrolytes, $Li_7La_3Zr_2O_{12}$, Li detection, Citrate-Nitrate

ÖZET

KATI-HAL LİTYUM-İYON PİLLERİN ÜRETİMİ VE KARAKTERİZASYONU

Kamil Burak DERMENCİ

Malzeme Bilimi ve Mühendisliği Anabilim Dalı
Anadolu Üniversitesi, Fen Bilimleri Enstitüsü, Ağustos 2018

Danışman: Prof. Dr. Servet TURAN

Garnet tipi $Li_7La_3Zr_2O_{12}$ (LLZO) katı elektrolitleri, geleneksel organik elektrolitlerin yerine potansiyel bir aday olarak kabul edilir. Fakat gösterdikleri performans organik esaslı sıvı elektrolitlere henüz yaklaşamamaktadır. Performansı artırıcı yönde yapılan çalışmalar daha çok kristal kimyası ve lityum hareket kinetikleri üzerine yoğunlaşmakla beraber, sinterleme davranışları aydınlatmak üzerine yeterli çalışma yapılmamıştır. Tez, katı hal ve çözelti tabanlı LLZO sentezini kapsamaktadır. Öncelikle, katı hal sentezinde, LLZO sentez koşullarının; Al içeriği, ısıtma hızı ve başlangıç hammadde tipi açısından optimizasyonu araştırılmış ve sinterleme sıcaklığının fonksiyonu olarak potansiyel bir sinterleme mekanizması önerilmiştir. Elektron mikroskobu teknikleriyle Lityum tespiti ve LLZO örneklerinin havada kararlılığı ToF-SIMS ekli FIB-SEM ile çalışılmıştır. Sitrat-Nitrat LLZO sentezinde, Zirkonyum kaynağı ve anyonik türlerin LLZO'nun kübik faz kararlılığı üzerindeki etkisi ele alınmıştır.

Termodinamik açıdan tercih edilen başlangıç hammaddelerinin belirlenmiş ve ToF-SIMS ekli ve Xe iyon kaynaklı FIB-SEM kullanılarak LLZO'da yüksek hassasiyetli Lityum haritaların oluşturularak ile yapıdaki safsızlıklar başarıyla belirlenmiştir. Sitrat-Nitrat sentezinde, nitrat iyonlarının LLZO'nun kübik faz stabilizasyonu üzerindeki negatif etkisi de ilk kez gösterilmiştir. 0.211 mS/cm ile en yüksek iletkenlik 1200 °C'de 12 saat katı hal reaksiyonu ile sinterlenmiş LLZO örneklerinde elde edilmiştir.

Anahtar Sözcükler: Katı elektrolitler, $Li_7La_3Zr_2O_{12}$, Li tespiti, Sitrat-Nitrat

ACKNOWLEDGEMENTS

Starting from my BSc years in Istanbul Technical University, there are so many people who have added something to my life and have always been guided by their knowledge and experience. Unfortunately, it is not possible to thank all of them individually. I offer my deepest thanks to Prof. Dr. Servet TURAN. He has guided during laboratory work, provided the best working environment as possible as he can. I can share our smallest complaints without hesitation. In other words, he was literally a "supervisor". I'd also express my gratitude to my thesis progress jury (Prof. Dr. M. Kadri AYDINOL and Prof. Dr. Ender SUVACI) for their valuable contributions and encouragement.

I'd especially like to thank Prof. Dr. Alpagut KARA, Mr. Mustafa ÇOBANCI, Mr. Orhan ÇETİN and Ceramic Research Center for providing a comfortable environment for characterization methods such as dilatometer, thermal analysis and XRF. I'd also like to thank Mrs. Hana Tesařová and Mr. Tomáš Šamořil from TESCAN ORSAY HOLDING for ToF-SIMS attached FIB-SEM analysis.

I would like to express my deepest gratitude to Anadolu University – Scientific Research Project Unit for providing a financial support with a Grant No: 1502F070 making it possible to build an Electrochemical Cell Systems Laboratory within Material Science & Engineering Department.

I know that without collaboration, an important part of the thesis wouldn't be possible. Therefore, I'd also like to thank Onur KAKİLLİ, Eren ÇEKİÇ, Cem Eren ÖZBİLGİN, Tayfun KOÇAK, Musah ABDULAI, Can TATLISU, Tunç YANIK, O. Kağan ENNİ, A. Furkan BULUÇ and all ST-AR Battery Research Group members and candidates.

I should add that the working environment plays a crucial role for academic researches. For that reason, I'm grateful to the MatSE family for their kind hospitality and optimism.

I couldn't deny my family's financial and motivational support during my thesis. I offer my biggest thanks to my father Hazim DERMENCİ, my mother Hayriye DERMENCİ and my sister, Begüm DERMENCİ. My fiancée!! I dedicated this thesis to you.

Kamil Burak DERMENCİ

08.08.2018

STATEMENT OF COMPLIANCE WITH ETHICAL PRINCIPLES AND RULES

I hereby truthfully declare that this thesis is an original work prepared by me; that I have behaved in accordance with the scientific ethical principles and rules throughout the stages of preparation, data collection, analysis and presentation of my work; that I have cited the sources of all the data and information that could be obtained within the scope of this study, and included these sources in the references section; and that this study has been scanned for plagiarism with “scientific plagiarism detection program” used by Anadolu University, and that “it does not have any plagiarism” whatsoever. I also declare that, if a case contrary to my declaration is detected in my work at any time, I hereby express my consent to all the ethical and legal consequences that are involved.

Kamil Burak DERMENCİ

TABLE OF CONTENTS

TITLE PAGE ..... **i**

FINAL APPROVAL FOR THESIS ..... **ii**

ABSTRACT ..... **iii**

ÖZET ..... **iv**

ACKNOWLEDGEMENTS ..... **v**

STATEMENT OF COMPLIANCE WITH ETHICAL PRINCIPLES AND RULES ..... **vi**

TABLE OF CONTENTS ..... **vii**

LIST OF TABLES ..... **ix**

LIST OF FIGURES ..... **x**

INDEX OF ABBREVIATIONS AND SYMBOLS ..... **xiii**

1. ALL SOLID-STATE LI-ION BATTERIES **1**

1.1. Inorganic Solid Electrolytes **7**

1.2. All Solid-State Li-ion Battery Assembly **11**

1.3. Motivation and Structure of the Dissertation **11**

2. OPTIMIZING THE SYNTHESIS CONDITIONS OF SOLID-STATE REACTION SYNTHESIZED $Li_7La_3Zr_2O_{12}$ **13**

2.1. Motivation **13**

2.2. Experimental **15**

2.3. Results & Discussion **16**

2.3.1. Thermal behavior of precursor powders **16**

2.3.2. Determination of existing phases after calcination **17**

2.3.3. Microstructural evaluation **19**

2.3.4. The effect of sintering time on the electrical conductivity of 30 mole % Al containing LLZO **26**

2.3.5. The effect of heating rate on solid-state synthesis of $Li_7La_3Zr_2O_{12}$ **30**

3. A THERMODYNAMIC POINT OF VIEW FOR SELECTING PRECURSORS FOR SOLID STATE $Li_7La_3Zr_2O_{12}$ SYNTHESIS **35**

3.1. Motivation **35**

3.2. Experimental **36**

3.3. Results & Discussion 37
3.3.1. Thermodynamic Calculations 37
3.3.2. Characterization of $Li_7La_3Zr_2O_{12}$ by using thermodynamically favored precursors 39
3.4. Conclusion 49

4. A NOVEL DENSIFICATION MODEL FOR $Li_7La_3Zr_2O_{12}$ 50
4.1. Motivation 50
4.2. Experimental 51
4.3. Results & Discussion 52
4.4. Conclusion 57

5. LI DETECTION BY USING MICROSCOPY TECHNIQUES 58
5.1. Motivation 58
5.2. Experimental 60
5.3. Results & Discussions 61
5.4. Conclusion 68

6. AIR STABILITY ASSESSMENTS OF $Li_7La_3Zr_2O_{12}$ BY FIB-SEM COMBINED TOF-SIMS 70
6.1. Motivation 70
6.2. Experimental 71
6.3. Results & Discussion 71
6.4. Conclusion 76

7. SOLUTION BASED SYNTHESIS OF $Li_7La_3Zr_2O_{12}$ 77
7.1. Motivation 77
7.2. Experimental 78
7.3. Results & Discussion 79
7.3.1. Citrate-Nitrate Approach 79
7.3.2. A modified Citrate-Nitrate method for $Li_7La_3Zr_2O_{12}$ synthesis 94
7.4. Conclusion 96

8. CONCLUSION & FUTURE REMARKS 99

REFERENCES 102

RESUME

LIST OF TABLES

Table 1.1. *Melting point and dielectric constant of organic solvents*.....6
Table 2.1. *SEM-EDS point analysis from the polished surfaces* 22
Table 2.2. *DC conductivities of 30 mole % Al containing LLZO pellets sintered at 1150 °C for 12, 24 and 36 hours*.....29
Table 2.3. Heating rates of solid-state reaction synthesized LLZO.....30
Table 3.1. *A brief overview of Li, La, Zr and Al sources used in the synthesis of LLZO through solid-state reaction related methods* 35
Table 3.2. *Gibbs Free Energy and Enthalpy change calculations for oxide formation reactions of LiOH, Li_2CO_3, $LiNO_3$, $La(OH)_3$ and $Al(OH)_3$* 38
Table 3.3. *Bulk conductivities of pellets sintered with Gibbs Free Energy mixture (σ_{dG}) and Enthalpy mixture (σ_{dH}) between 1000 and 1200 °C*.....47
Table 4.1. *Measured Archimedes density and radial shrinkage values for all sintering conditions*.....54
Table 7.1. *Calculated ionic conductivities of 20 - 40 mole % Al containing cubic LLZO powders*.....92
Table 7.2. *Comparison of 30 mole % Al containing LLZO samples synthesized via different methods*.....92
Table 7.3. *Nitrate ion contribution of each precursor used for solution-based LLZO synthesis*.....94
Table 7.4. *Quantitave analysis of Citrate-Nitrate synthesized LLZO by using RIR Method* 96

LIST OF FIGURES

Figure 1.1. *The capacity and potentials of battery electrode materials [7]* 3
Figure 1.2. *Crystal structure of Perovskite type solid electrolytes [13]* 8
Figure 1.3. *Crystal structure of NASICON type solid electrolytes [13]* 9
Figure 1.4. *Crystal structure of LISICON type solid electrolytes [13]* 9
Figure 1.5. *Crystal structure of Garnet type solid electrolytes [13]* 10
Figure 2.1. *TG and DTG curves of mixed precursor powders* 16
Figure 2.2. *XRD patterns of the pellets sintered at 1150 (a) and 1230°C (b) for 12h without Al addition* 18
Figure 2.3. *XRD patterns of 20 mole % Al containing LLZO pellets sintered at 1100°C for 12 h (a), 24 h (b) and 1150°C for 12 h (c), 24 h (d); 25 mole % Al containing LLZO pellets sintered at 1100°C for 12 h (e), 24 h (f) and 1150°C for 12 h (g), 24 h (h); 30 mole % Al containing LLZO pellets sintered at 1100°C for 12 h (i), 24 h (j) and 1150°C for 12 h (k) and 24 h (l)* 19
Figure 2.4. *BSE images obtained from 20 mole % Al containing LLZO pellets sintered at 1100°C for 12 h (a), 24 h (b) and 1150°C for 12 h (c), 24 h (d); 25 mole % Al containing LLZO pellets sintered at 1100°C for 12 h (e), 24 h (f) and 1150°C for 12 h (g), 24 h (h); 30 mole % Al containing LLZO pellets sintered at 1100°C for 12 h (i), 24 h (j) and 1150°C for 12 h (k) and 24 h (l)*.....21
Figure 2.5. *BSE-SEM image and SEM-EDS mapping of pellet sintered at 1100 °C for 24 h*.....23
Figure 2.6. *EDS point analysis taken from two different regions having a different contrast*.....24
Figure 2.7. *Secondary electron images obtained from the fractured surfaces of the pellets containing: a) 20 mole %, b) 25 mole % and c) 30 mole % Al sintered at 1100 °C for 12 h*.....25
Figure 2.8. *Secondary electron images obtained from the fractured surfaces of the pellets of 30 mole % Al containing LLZO sintered at 1150 °C for: a) 12 h b) 24 h and c) 36 h* 27
Figure 2.9. *TG/DTG curves of powders after calcination at (a) 900 °C (b) 980 °C (b)* 31
Figure 2.10. *TG curve of precursor powders at 5 and 10 °C/min heating rates*.....32

Figure 2.11. *XRD patterns of LLZO powders after calcination at 1000 °C for 6 hours with 2, 5 and 10 °C/min* 33
Figure 3.1. *TG/DTA plots of powder mixtures prepared based on Gibbs Free Energy and Enthalpy change calculations*.....40
Figure 3.2. XRD *patterns of wet and dry mixed precursors for solid-state LLZO synthesis* 41
Figure 3.3. *XRD patterns of powders after calcination and pellets sintered at 1000 °C, 1100 °C and 1200 °C* 43
Figure 3.4. *Unpolarized micro-Raman spectrum of LLZO sintered at 1000 °C to 1200 °C for 12 hours*.....44
Figure 3.5. *Secondary electron images taken from the fractured surface of the samples sintered from Gibbs Free Energy and Enthalpy change mixture at 1000 °C (a), 1100 °C (b) and 1200 °C (c) for 12 hours*.....45
Figure 3.6. *Nyquist Plots of LLZO samples sintered at 1200 °C for 12 hours*.....47
Figure 3.7. *Arrhenius plot of LLZO sintered at 1200 °C for 12 hours*.....49
Figure 4.1. *Thermal expansion behavior of LLZO* 52
Figure 4.2. *Archimedes densities and radial shrinkage percentages of LLZO sintered at 1000, 1100 and 1200 °C* 53
Figure 4.3. *Fractured surface SEM images of LLZO sintered at 1000, 1100 and 1200 °C*.....55
Figure 4.4. *LLZO densification model as a function of temperature* 56
Figure 5.1. *XRD pattern of 30 mole % Al containing LLZO pellet sintered at 1100 °C for 24 hours* 62
Figure 5.2. *The polished (upper side) and fractured surface (lower side) images of 30 mole % Al containing LLZO pellet sintered at 1100 °C for 24 hours*.....63
Figure 5.3. *Elemental intensity maps from ToF-SIMS acquisition with Ga and Xe ion sources* 65
Figure 5.4. *Ga and Xe ion projection range into Lithium* 66
Figure 5.5. *(a) Collision depth profiles and (b) the number of vacancies produced from Ga and Xe ions in Lithium target*.....67
Figure 6.1. *SE images of (a) freshly polished (b) 1-week air exposed LLZO pellet*.....72
Figure 6.2. *BSE image of air exposed LLZO sample cross section view* 73
Figure 6.3. *SE images of 1-week air exposed LLZO samples before (a) and after (b) FIB excavation* 74

Figure 6.4. *Positive and negative mass spectra aquired from ToF-SIMS*.....75
Figure 7.1. *Citrate-Nitrate synthesis flowchart*.....80
Figure 7.2. *XRD patterns of LLZO powders synthesized by using $ZrOCl_2$ with different amount of Al addition (LZO: Li_2ZrO_3, LaAO: $LaAlO_3$, LaZO: $La_2Zr_2O_7$, ZO: ZrO_2) –All the other peaks in 0Al and 10Al belong to tetragonal; in 20Al, 30Al and 40Al belong to cubic LLZO phase*.....81
Figure 7.3. *XRD patterns of LLZO powders synthesized by using $ZrO(NO_3)_2$ with different amount of Al addition. (LCO: Li_2CO_3, LaO: La_2O_3, LLAO: $La_2Li_{0.5}Al_{0.5}O_4$) The remaining peaks belong to tetragonal LLZO. No cubic phase formation.*.....82
Figure 7.4. *Zr-O bonds in both tetragonal and cubic unit cell (upper side) and Zr coordinations (lower side) of tetragonal (t-LLZO) and cubic (c-LLZO) crystal structures along [100] direction.*.....84
Figure 7.5. *The XRD pattern of 4 mole HNO_3 per 1 mole LLZO added sample with the use of $ZrOCl_2$ precursor when calcined at 1000 °C for 6 hours*.....85
Figure 7.6. *TGA-FTIR analysis of evolved gases*.....86
Figure 7.7. *Evolved gas analysis from TGA-FTIR: a) temperature distribution of CO_2 release based on 2360 cm^{-1} b) IR spectrum at 346 °C and c) at 538 °C*...87
Figure 7.8. *SEM images of powders synthesized by $ZrOCl_2$ precursor: a) without Al addition, b) 10, c) 20, d) 30 and e) 40 mole % Al containing LLZO compositions after calcination at 1000 °C for 6 hours.* 89
Figure 7.9. *Nyquist plots of 20, 30 and 40 mole % Al stabilized cubic LLZO (20Al: 20-$ZrOCl_2$; 30Al: 30-$ZrOCl_2$; 40Al: 40-$ZrOCl_2$)* 91
Figure 7.10. *Dilatometer curve of LLZO samples synthesized via solid-state and Citrate-Nitrate methods*.....93
Figure 7.11. *Modified flowchart of solution-based LLZO synthesis by using La_2O_3 as a La source*.....95
Figure 7.12. *XRD patterns of calcined powders by using $La(NO_3)_3$ and La_2O_3 precursors between 700-800 °C calcination temperature for 6 hours*....97

INDEX OF ABBREVIATIONS AND SYMBOLS

DC	: Direct Current
DEC	: Diethylene Carbonate
DTA	: Differential Thermal Analysis
E_a	: Activation Energy
EC	: Ethylene Carbonate
EIS	: Electrochemical Impedance Spectroscopy
eV	: Electron-Volt
EV	: Electrical Vehicle
FIB-SEM	: Focused Ion Beam – Scanning Electron Microscopy
HEV	: Hybrid Electrical Vehicle
k	: Boltzmann Constant
kW	: Kilowatt
LLZO	: $Li_7La_3Zr_2O_{12}$
R	: Gas constant
SEI	: Solid-Electrolyte Interphase
T	: Temperature
TGA	: Thermogravimetric Analysis
ToF-SIMS	: Time-of-Flight Secondary Ion Mass Spectroscopy
V	: Volt
XRD	: X-Ray Diffraction
ΔG	: Gibbs Free Energy Change
ΔH	: Enthalpy Change
ρ	: Density
σ	: Conductivity

1. ALL SOLID-STATE LI-ION BATTERIES

Renewable energy and battery technologies nowadays become very important to reduce carbonaceous fuel usage in the field of energy and for the global need of energy storage [1-3]. Portable and reusable energy storage units are the most important concepts for the efficient energy consumption. Additionally, safe and long lasting service life are main expectations on the next generation battery technology [4]. In the light of above-mentioned expectations, lithium ion secondary batteries are the most promising candidates.

Secondary batteries can be divided into 4 groups that are Lead acid batteries, Nickel-Cadmium batteries, Nickel Metal Hydride batteries and Lithium ion batteries. In widely known Lead-acid batteries, lead electrodes and sulphuric acid electrolyte. Anodic reaction of Lead acid batteries is;

$$Pb_{(s)} + (SO_4)^{2-}{}_{(aq)} \rightarrow PbSO_{4(s)} + 2e^- \qquad E_a=0.35\ V \qquad (1.1)$$

where the cathodic reaction is;

$$PbO_{2(s)} + (SO_4)^{2-}{}_{(aq)} + 4H_3O^+{}_{(aq)} + 2e^- \rightarrow PbSO_{4(s)} + 6H_2O \qquad E_c=1.70\ V \qquad (1.2)$$

Because of using Lead based electrodes and sulphuric acid electrolytes, they are named as Lead acid batteries. Other type of secondary batteries is called Nickel-Cadmium Batteries and based on coupling cadmium metal and nickel oxyhydroxide (NiOOH) and immersed in KOH electrolyte. Anodic and cathodic reactions of Ni-Cd batteries are as follows:

$$Cd_{(s)} + 2OH^-{}_{(aq)} \rightarrow CdOH_{2(s)} + 2e^- \qquad E_a=0.82\ V \qquad (1.3)$$

$$NiOOH_{(s)} + 2H_2O_{(l)} + 2e^- \rightarrow 2Ni(OH)_{2(s)} + 2OH^-{}_{(aq)} \qquad E_a=0.48\ V \qquad (1.4)$$

In 1920s and 1930s, Zn-NiOOH batteries were present. Due to the very low cycle life, Zn-NiOOH batteries did not attract more interest. Minimum of 500 charge-discharge cycles are required to meet expectations of battery market. For electric

vehicle (EV) applications, minimum of 1000 cycle needed, whereas, 20000 cycles required for aerospace applications.

In 1989, Nickel-Metal Hydride (Ni-MH) battery found a place in the battery market. As it can be understood from its name, only anode material is different from the Ni-Cd batteries. Ni-Cd battery uses Cd anode whereas the Ni-MH uses hydride alloys. Anodic and cathodic reactions of Ni-MH battery is shown below:

$$MH_{(s)} + OH^-_{(aq)} \rightarrow H_2O + e^- + M \qquad E_a=0.72\ V \qquad (1.5)$$

$$NiOOH_{(s)} + 2H_2O_{(l)} + 2e^- \rightarrow 2Ni(OH)_{2(s)} + 2OH^-_{(aq)} \qquad E_a=0.48\ V \qquad (1.6)$$

Production of Ni-MH battery nearly doubled the energy density compared to Ni-Cd batteries and become available for the aerospace applications. However, Ni-MH is less durable than Ni-Cd and shows high self discharge behaviour, poor cycling ability and lower shelf life [5, 6].

In 1970s, Lithium based batteries have started to attract researchers because of its low density and high electropositive behaviour. Lithium shows 3860Ah/kg specific capacity. In comparison with Pb that has 260 Ah/kg, lithium allows very high electrode potentials that make it indispensible for secondary battery technology. The first prototypes of lithium batteries are presented from Exxon, Moli Energy and Taridan. They were able to reach 230W/kg specific power by changing cathode materials. On the other hand, lithium foil anode and organic electrolytes used in such batteries caused safety problems. Metallic Lithium anode reacts with organic electrolytes and decomposes.

The first prototype of Li-ion battery from Sony was commercially released in 1991. Lithium ion battery is based on the transportation of Li^+ ions between electrodes during charging or discharging. It contains, in most cases, carbon-based anode and lithium metal oxide cathode where metal is Co, Mn, Ni. Insertion or intercalation of Li^+ ions stores energy in the battery by following anodic and cathodic reactions.

$$Li_xC \rightarrow C + xLi^+ + xe^- \qquad E_a=2.9\ V \qquad (1.7)$$

$$Li_{1-x}CoO_2 + xLi^+ + xe^- \rightarrow LiCoO_2 \qquad E_a=1.2\ V \qquad (1.8)$$

In Figure 1.1, the capacity and potential values of battery electrode materials used in Li-ion batteries are presented [7].

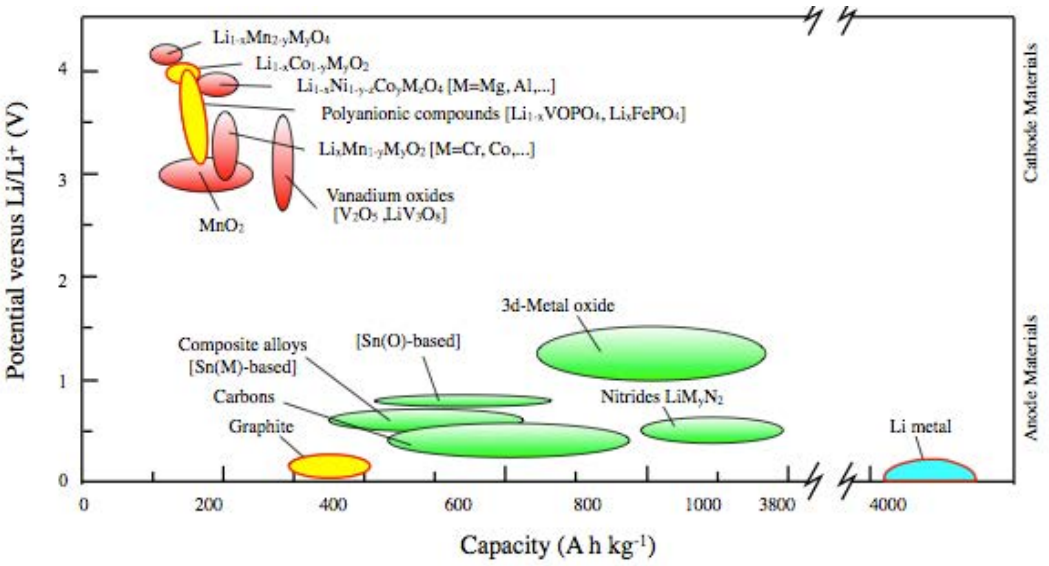

Figure 1.1. *The capacity and potentials of battery electrode materials [7]*

As it can be seen from the Figure 1.1, cathode materials of lithium metal oxides, lithium metal phosphates, vanadium oxides have high potentials but low capacities. Anode materials such as carbon-based materials, composite alloys, 3d-metal oxides, lithium metal nitrides as well as Lithium have low potentials but high capacities. To obtain high energy from the battery, the difference between anode and cathode materials are as high as possible in the potential point of view. However, battery capacity is limited by the lowest electrode capacity, so anode and cathode materials should have similar capacity and the limiting electrode capacity is as high as possible. Layered structure of graphite and lithium cobalt oxide ($LiCoO_2$) makes Li^+ intercalation easier; the volume change in crystal structure during intercalation is lowered. As a result of this, the cycle life of the battery is increased and high potential difference and high energy density is provided [6]. Li-ion batteries can find varying applications from laptops to cell phones because of their high energy densities. On the other hand, Li-ion batteries cannot meet the battery market expectations especially H/EV and high temperature applications due to cost and safety disadvantages [3, 8]. Usually, one cell is not enough to reach high power (20-35 kW) required for HEV. Because of that, more than one cell should be connected in series or parallel in order to reach the expected values. Connection in series resulted in an increase in potential and power. However, US Department of Energy (DoE) has limitation of 400V for cells connected in series.

The reason of this is the possibility of non-operating cells in the system. If the cell is non-operating, electrolyte may degrade or electrodes act as a capacitor that results in the formation of unwanted gases and causing safety issues [6].

Additionally, electrolyte properties must also be taken into consideration. For example, widely used liquid $LiPF_6$ - organic carbonate electrolytes have high vapour pressure and flammable. They are also harmful for environment and human health. To provide safer service conditions, attempts are mainly based on more stable solid-electrolyte interface (SEI) formation by additives, increasing the thermal stability, preventing the overcharging and using another types of Lithium salts. All of the above mentioned approaches provide safer service conditions, but, loss of specific energy is observed. The potential range that Li-ion electrodes are stable with electrolyte (electrochemical window) is one of the critical parameters for the safer service [3, 9]. Moreover, acting battery electrodes as a capacitor could cause serious safety problems. Electrodes collect charge and the battery system shows local charge accumulation. That results in even only one bad cell, a dramatical potential drop in the EV battery module. Energy density and battery materials are the focal points of battery safety issues. Higher energy density obtained, higher safety risks. A bad cell or short circuit in high energy density Li-ion batteries could generate significant heat in the system. If the battery temperature exceeds 130°C, lithium and organic electrolytes shows exothermic reaction which causes on explosion or flaming.

In the light of above mentioned issues concerning safer service conditions, there are 4 notions to be taken into consideration that are overcharging, overheating, electrical short circuit and physical abuse of battery. If the battery is fully charged, Li^+ ions completely deintercalated from the positive electrode and the completely delithiated electrode structure would chemically instable. That structure gives heat which could cause explosion to become stable. Using phosphate-based cathodes (e.g. $LiFePO_4$) instead of oxide based cathodes (e.g. $LiCoO_2$) is offered to improve safety due to overcharging, because the oxidation of Fe^{2+} ions to Fe^{3+} ions during delithiation is more stable than the oxidation of Co^{3+} ions to Co^{4+} ions. Short circuits are dangerous because of forming rapid temperature increases. They can be seen either at inner side of the battery or outer side of the battery. Internal short circuits must strictly be avoided due to difficulties of repairing. Physical abuse of batteries such as dropping and throwing may also cause unexpected short circuits [6].

Electrolytes in the Li-ion batteries provide the ionic conductivity between anode and cathode. Ionic conductivity can be described as transportation mechanism of ions by means of diffusion. During charging of Li-ion battery system, Li^+ ions are forced to move from cathode towards anode and during discharging, Li^+ ions move towards anode. External electric field and concentration gradient are two main driving forces for ionic conductivity. The relationship between ionic conductivity and diffusivity is given as follows:

$$\sigma = \frac{q_i^2 c_i}{k_B T} D_i \tag{1.9}$$

where σ is the ionic conductivity; D_i is the diffusivity; q_i is the charge of ions, c_i is the ion concentration; T is the temperture and k_B is the Boltzmann constant. External electric field and concentration gradient has strong impact on diffusivity, so when electric field and concentration gradient changes, ionic conductivity changes. Electrolytes can be divided into 3 main subgroups that are organic, ionic liquid and solid state electrolytes [10].

Organic electrolytes are the most common electrolyte type found in battery market. They consist of organic cations and carbonate anions. Organic electrolytes show high ionic conductivity (1-11 S/cm) but their stability is low and easily flammable. An intermediate phase forms by the use of highly reactive negative electrode such as Lithium. The intermediate phase which is often called Solid-Electrolyte Interphase (SEI), blocks chemical reactions between electrode material and electrolyte as well as transportation of ions. Table 1.1 presents widely used organic solvents in the Li-ion battery electrolyte. Usually, electrolytes contain two or more of solvents to improve performance. Despite the fact that none of these solvents are stable at 5V, solutions of EC and DMC is stable [10, 11].

Ionic liquid electrolytes composed of high ion concentration are non-flammable and non-toxic electrolytes. Conduction phenomenon in ionic liquids is based on the transportation of ions. They have low vapour pressure, which is directly related to the energy needed to break the bonds, high thermal and electrochemical stability. Because of their high viscosity, ionic conductivity of ionic liquids is 3-4 times lower than organic electrolytes.

Table 1.1. *Melting point and dielectric constant of organic solvents*

Solvent	Melting Point (°C)	Dielectric Constant	Solvent	Melting Point (°C)	Dielectric Constant
Diethyl Carbonate (DEC)	-74.3	2.8	Acetonitrile (AN)	-48.9	36
Ehyl Methyl Carbonate (EMC)	-53	64.9	Ethylene Carbonate (EC)	36.4	53
Propylene Carbonate (PC)	-48.8	39	Tetrahydrofuran (THF)	-108.5	7.4
Butyrolacrone (GBL)	-43.5	34	Dimethyl Carbonate (DMC)	4.6	3.1

Researches are mainly focused on factors affecting viscosity (Van der Waals and Coulombic forces, ion shape etc.) Besides its relatively low ionic conductivity (in the range of mS/cm), ionic liquids have high tendency to form SEI [10, 11].

Solid-state electrolytes have significant advantages over liquid electrolytes such as simple design, resistance to shock and vibration, pressure and temperature variations, wide electrochemical stability window and improved safety. Different types of solid-state electrolytes are polymeric gels (solvent free polymers), inorganic solid compounds and inorganic glasses. On the other hand, solid state electrolytes have poor contact with electrodes [9, 10]. For polymer electrolytes, ionic conductivity is in the range of 10^{-4} – 10^{-8} S/cm, however for inorganic crystals and glasses, ionic conductivity ranges are 10^{-3} – 10^{-11} S/cm and 10^{-3} – 10^{-9} S/cm respectively [10].

The ionic mobility in polymeric gels was provided by motion of polymers. Ions can be transported when polymer segments move significant distance, which is directly related to glass transition temperature (T_g). When the temperature is above T_g, polymers show fast ionic conduction.

Concentration gradient (driving force for diffusion), as it's mentioned earlier, one of the important parameters that affect ionic conduction. Diffusion in condensed materials and grain boundary diffusion has strong impact on diffusion mechanism in ionic conductors. Diffusion in condensed materials can be explained by two phenomena of vacancy (defect)-mediated diffusion and non-vacancy (defect)-mediated diffusion. An example of defect-mediated diffusion is Schottky pairs. A group of metals and

alloys contains Schottky pairs, which are composed of cation vacancy and anion vacancy. Schottky pairs have relatively low ionic conductivity and high activation energy due to the movement of vacancies. On the other hand, non-defect-mediated diffusion mechanism is based on Frenkel pairs that are the combination of cation vacancy and cation interstitial. Motion of interstitial cations is the primary source for ionic conduction. That is the main reason of why ionic conductivity is higher than defect-mediated diffusion. Low activation energy can be seen in Frenkel disorder. Lithium ions, due to their small radius, diffuse by interstitial non-defect-mediated diffusion mechanism. To reach realistic results, it is also important to take grain boundary diffusion into consideration. Grain boundary is the interface between two crystals (called grains). Crystallographic orientation, composition, lattice dimensions and bonding state may differ in each crystal. Grain boundaries are low migration barriers. They have defect-mediating diffusion due to the incomplete bonding and disorder. Thus, diffusivity is higher than grains [10]. Several researchers studied to improve ionic conduction of solid electrolytes used in Li-ion batteries. Most of their work can be classified by three main approaches of changing electrolyte types, modifying existing electrolytes and offering novel 2D-3D battery structure in order to decrease the Li^+ ion transport distance.

1.1. Inorganic Solid Electrolytes

Inorganic solid electrolytes are attracted great interest because of their relatively high ionic conductivity and relatively low electronic conductivity among other solid electrolytes. Besides, grain boundary resistance is quite low when using polycrystalline materials are used [12]. Solid electrolytes that show Li^+ ion conductivity are Perovskite, NASICON, LISICON and Garnet type electrolytes.

Perovskite structure of AB_3 general formula, as shown in Figure 1.2, has excellent tolerance for ion substitution on both A and B sites resulting in large vacancy concentrations.

For Li ion conductors 1/6th of Li^+ ions substitutes into various A-deficient compositions. Lithium conductivity depends on Lithium and vacancy concentrations on A sites, the degree of cation ordering, the size and symmetry of the unit cell. The highest conductivity is measured as $1.5x10^{-3}$ S/cm for $La_{2/3-x}Li_{3x}TiO_3$ where x = 0.11. Perovskite type electrolytes are not useful in combination with very reducing anode

materials due to strongly enhanced Ti^{4+} reduction which increases electronic conductivity dramatically [12, 13].

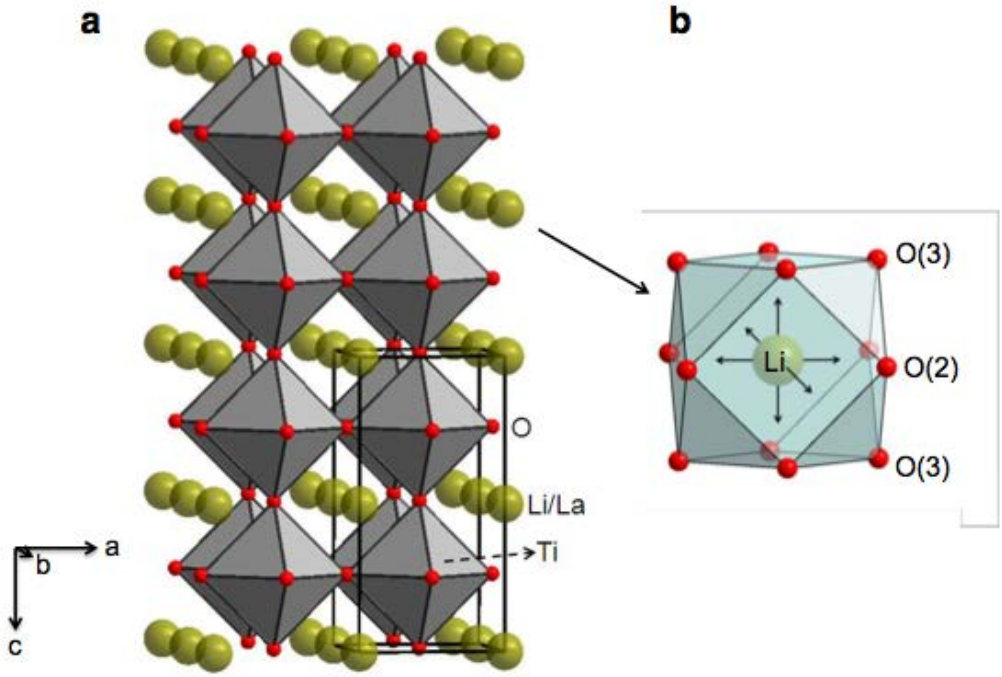

Figure 1.2. *Crystal structure of Perovskite type solid electrolytes [13]*

First Na-SuperIonic CONductor (NASICON) type crystal $NaA_2(PO_4)_3$ (A=Ge, Ti, Zr) was defined in 1968. General composition of Li^+ conducting NASICON is $Li_{1+x}M_2(PO_4)_3$ where $0<x<3$ and presented schematically in Figure 1.3. $Li_{1.3}Al_{0.3}Ti_{1.7}(PO_4)_3$ (LATP) shows ionic conductivity of $3x10^{-3}$ S/cm at ambient temperature. NASICON electrolytes, same as perovskite, are highly unstable with very reductive anode materials such as Lithium metal because of the reduction of Ti^{+4} [12, 13].

LIthium SuperIonic CONductors (LISICON) have an ABO_4 composition and they are known as γ-Li_3PO_4 in which B tetrahedra share corners with clusters of three AO_4 tetrahedra (Figure 1.4). Typical example of LISICON electrolytes is $Li_{14}ZnGe_4O_{16}$ which Li and Zn at A sites and Ge or V at B sites. They are highly reactive with Lithium metals and CO_2, which negatively affects on the ionic conductivity.

Garnet type electrolytes with general formula of $Li_5La_3M_2O_{12}$ (M=Ta, Nb) show relatively high ionic conductivity (in the range of 10^{-4} - 10^{-5} S/cm) among other solid

electrolytes and become a hot prospect for All-Solid State Li-ion Batteries. They have high decomposition potential of 6V against Li.

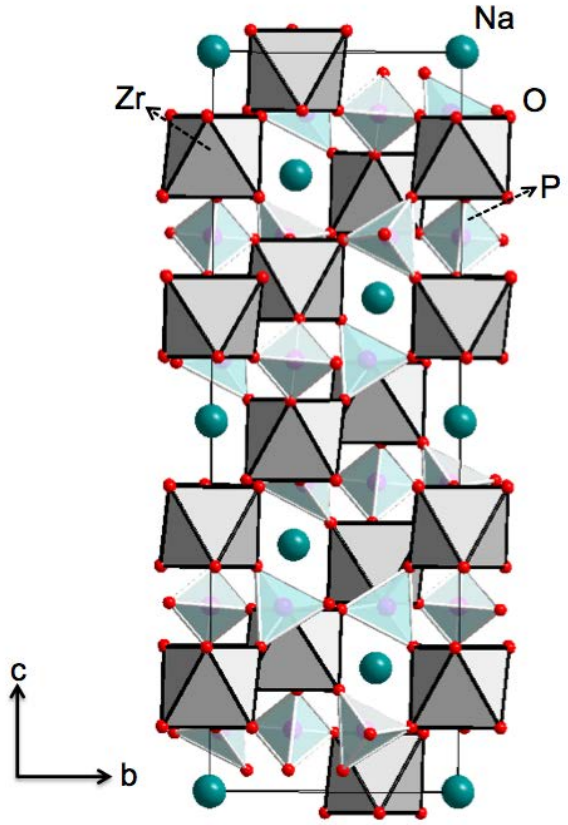

Figure 1.3. *Crystal structure of NASICON type solid electrolytes [13]*

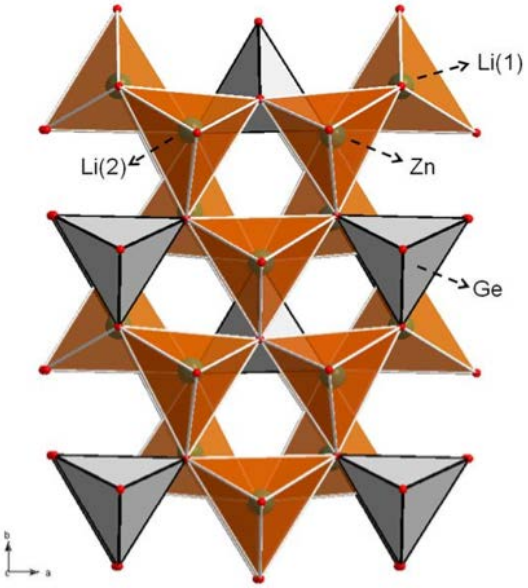

Figure 1.4. *Crystal structure of LISICON type solid electrolytes [13]*

The activation energy at low temperatures is quite high. Li atoms in garnet structure presents at tetrahedral (24d) and octahedral (48g) sites but only 80 % of 24d sites and 40 % of 48g sites are occupied with Lithium atoms. This phenomenon has strong impact on ionic mobility of Li^+ ions. Smallest atoms in Figure 1.5 show the possible locations and route of Li^+ ions in conduction mechanism. Li atoms in octahedral sites are mobile while atoms in tetrahedral sites act as cation traps [12].

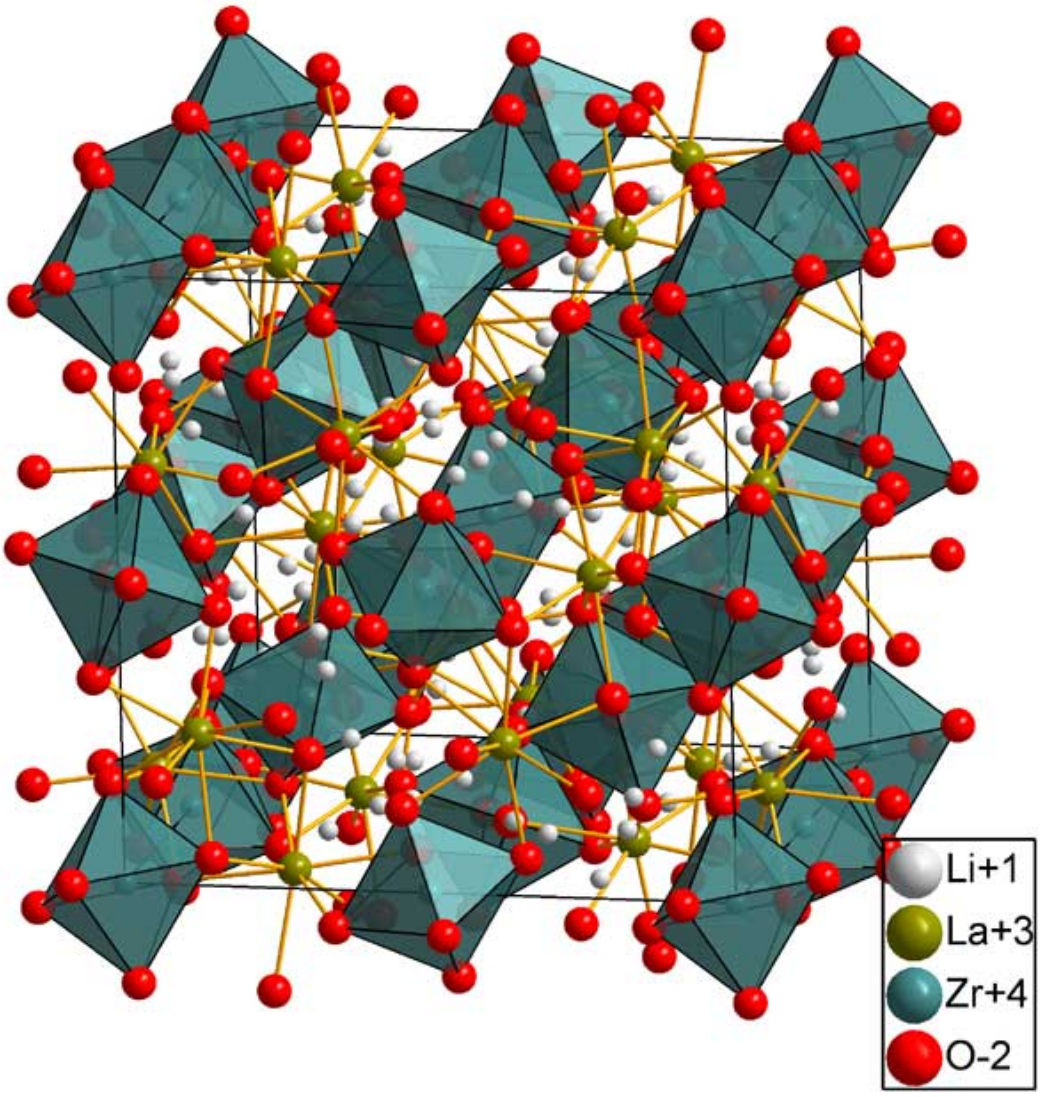

Figure 1.5. *Crystal structure of Garnet type solid electrolytes [13]*

1.2. All Solid-State Li-ion Battery Assembly

An all solid-state Li-ion battery consists of two electrodes (anode and cathode) with a solid electrolyte located between these two electrodes. Since solid electrolyte is not able to wet electrodes like liquid electrolytes, there are several challenges that scientist are trying to overcome. These are listed as follows [14]:

i. Volumetric changes and stress changes during charge-discharge process
ii. Ion and electron migration of electrode materials
iii. Ion migration of electrolytes
iv. Solid electrolyte/electrode interface structure

The first protoypes of all solid-state Li-ion batteries were launched as a thin-film microbatteries that has a very thin continuous solid electrolyte film on the surface of each electrode. The state-of-the-art of the all solid-state Li-ion batteries allows very limited current densities (C-rates) resulting with a very limited power density. Until now, many approaches were adapted in order to overcome this problem. These are based on reducing electrode-electrolyte interface resistance by activating the electrolyte surface by coating techniques such as sputtering [15] and PLD [16], conditioning surface by Li_2CO_3 coating [17], enhance wettability of electrolyte [18]. Such techniques are quite expensive and very complex assembly techniques. Researchers focused on to move one step further and are trying to find a way for bulk-type all solid-state Li-ion battery in the near future. Therefore, understanding the nature of solid electrolytes will give new insights in the field of solid-state battery assembly.

Garnet type solid electrolytes stand forward with their good crystallinity, high mechanical strength and highly dense microstructure. However, high-energy consumption during synthesis, impurity phase formation, and microstructure having coarse grains are the main drawbacks of garnet type electrolytes [19].

1.3. Motivation and Structure of the Dissertation

The dissertation focuses on to synthesize LLZO in an technologically feasible manner, elucidate LLZO sintering behavior as well as explaining the potential densification mechanism with the help of microstructural changes and Lithium detection in microscopically techniques. The dissertation contains seven chapters and a general conclusions chapter. Each chapter has its own logical flow. The dissertation

starts with a general introduction chapter which includes a general overview related to the Li-ion batteries and the state-of-the-art of the all solid-state Li-ion batteries.

Starting from Chapter 2, an optimization on synthesis parameters such as stabilizer content, calcination & sintering conditions and heating rate is discussed. Their performance is evaluated by DC polarization method.

In Chapter 3, thermodynamically ideal precursors were determined in terms of Gibbs Free Energy and Enthalpy changes of oxide formation reactions. Solvent stability of the precursor powders is also discussed. The ideal precursors are identified in terms of existing impurities and residual tetragonal LLZO phase. The performance of the as-synthesized pellets is discussed by both ionic conductivity changes and activation energy obtained by using Electrochemical Impedance Spectroscopy.

A densification model that represents the microstructural changes as a function of sintering temperature is presented in Chapter 4. The role of closed porosities and insufficiency of Archimedes density measurements are assessed within the chapter. Radial shrinkage is offered as a secondary tool for LLZO densification.

In Chapter 5, Lithium detection in electron microscopy techniques is discussed. Detecting capabilities of both Ga and Xe ion source FIB-SEM and their efficiency for detecting light materials such as Lithium are compared by using Monte Carlo Simulations. First Lithium elemental maps by using ToF-SIMS combined Xe-ion source FIB-SEM is presented within this chapter.

In Chapter 6, the surface impurities formed from air-aged LLZO samples is discussed with ToF-SIMS attached Ga ion source FIB-SEM. The anions and cations are determined from ToF-SIMS positive and negative spectra.

In Chapter 7, bottom-up approach of LLZO synthesis (Citrate-Nitrate Method) is used. The role of Zirconium precursors having a different dissociation behavior on cubic phase stabilization of LLZO is studied. The negative influence of nitrate ions on cubic phase stabilization is discussed within this chapter.

2. OPTIMIZING THE SYNTHESIS CONDITIONS OF SOLID-STATE REACTION SYNTHESIZED $Li_7La_3Zr_2O_{12}$

All Solid State Lithium Ion Batteries (ASS-LIB) have been attracting great attention due to their high temperature stability, energy density and safety. Cubic $Li_7La_3Zr_2O_{12}$ (LLZO) ceramic electrolyte is one of the most studied solid electrolyte because of its exceptionally high chemical stability against Li metal, air and moisture, thermal stability and very competitive ionic conductivity. In order to stabilize cubic LLZO, relatively high temperatures are required. On the other hand, it's possible to decrease sintering temperature and time with a stabilizer addition. In this chapter, the optimum synthesis parameters were determined in terms of Al content, cubic phase stabilization temperature and sintering time. The performance of the synthesized solid electrolytes was evaluated by assessing the microstructural changes and DC conductivity. After that, the optimum calcination conditions as well as heating rate was also determined by using thermal analysis methods.

2.1. Motivation

Petroleum based energy sources are expected to come to an end in the near future. For this reason, there is a growing interest on alternative technologies for energy sources and storage. Secondary Li-ion batteries are important types of energy storage systems that are considered to replace petroleum based energy sources. Achieving high power and energy densities would open new perspectives and find new application areas for Li-ion batteries from consumer electronics to even electrical vehicle (EV) applications. However, in terms of EV applications, safety is a crucial parameter preventing the widespread use.

Typical battery system contains anode, cathode and electrolyte. Electrolyte is the main substance concerning the safety of batteries. Organic liquid electrolytes that are widely used in commercial Li-ion secondary batteries are flammable, not stable at high voltages and they possess a possibility of short circuit [1, 20]. On the other hand, solid-state electrolytes show high electrochemical stability at high voltages and excellent temperature stability that makes them indispensible electrolyte candidates to enhance safety issues. Achieving comparable transport properties are the main challenges on solid electrolyte research [21, 22].

Nowadays, a garnet type solid electrolyte $Li_7La_3Zr_2O_{12}$ (LLZO) is one of the most studied electrolyte because of its exceptionally high stability against Li metal, air and moisture; thermal stability and competitive total conductivity (approx. 10^{-4} S/cm at 25 °C) in comparison to liquid electrolytes [23]. There are two polymorphs of LLZO reported so far [24, 25]. Tetragonal – the low-temperature stable form of LLZO – has approx. 10^{-6} S/cm Li^+ conductivity [24]. However, cubic – high-temperature stable form of LLZO – rises up to 5.11 x 10^{-4} S/cm. Cubic structure can be stabilized by either increasing synthesis temperature to where the cubic phase is stable or doping with stabilizers during synthesis. In the case of pure LLZO, cubic phase stabilization temperature was found to be around 1230 °C [25]. On the other hand, stabilizer addition would lower the stabilization temperature and result in increased ionic conductivity. W, Al, Ta, Ba, Te, Y and Nb were used to stabilize cubic form of LLZO. For example, 0.25 moles of Te addition reduced the stabilization temperature to 1100°C and increased the Li^+ conductivity to 1.03 x 10^{-3} S/cm [20]. Similarly, Al addition increased the Li^+ conductivity within the range of 10^{-4} S/cm. When Al introduced into the LLZO structure, it can substitute Li. The Kroger-Vink notation for Al-Li substitution is as follows:

$$2[Al_{Li}^{\bullet\bullet}] = [V_{Li}^{\prime}] \tag{2.1}$$

It's found that, below 0.204 moles of Al addition could not stabilize the cubic form since Li vacancy concentration is insufficient. If the Al addition is higher than 0.389 moles, it exceeds the maximum Al solubility in the cubic form and a secondary phase of $LaAlO_3$ can be formed [26].

Although, numerous studies were focused on the synthesis of LLZO in the literature, very few of them contain microstructural evaluation and use dry polishing with a maximum of 800 grit polishing papers [21, 27]. Therefore, the purpose of this chapter was to investigate the microstructural changes by adding 20, 25 and 30 mole % Al to LLZO which is produced via solid state reaction method. The effect of sintering conditions on the electronic conductivity was also a purpose of the current chapter.

2.2. Experimental

The effect of Al content, sintering temperature and sintering time on the cubic phase stabilization was investigated. Firstly, Li_2CO_3 (Merck) was dried at 200 °C, whereas La_2O_3 (Sigma-Aldrich) and ZrO_2 (Inframat) were dried at 900 °C before mixing to get rid of the hydroxides and humidity. Al_2O_3 (Ceralox) was used as Al source to stabilize the cubic phase. Stoichiometric amounts of powders were mixed in agate mortar grinder (Retsch RM200). 15 % of excess Li as Li_2CO_3 was added in order to compensate Li losses during the calcination. Powders were calcined at 900 and re-calcined at 980 °C for 12 hours in a muffle furnace (Nabertherm). Between each calcination step, powders were reground. After that, 2 g of calcined powders were isostatically pressed into pellet (16 mm diameter) at 290 MPa. Then, different amounts of Al containing pellets were sintered at 1100 °C and 1150 °C for 12 and 24h sintering time within a powder bed containing calcined powders. Alumina crucible was used for all heat treatments. 2°C/min heating rate was set in order to minimize unexpected Li losses during heat treatments.

In order to investigate the thermal behavior of starting powders, Netzsch STA 449 F3 Thermogravimetry/Differential Thermal Analysis (TG/DTA) analysis were conducted. Mixed precursor powders were put into alumina crucible and heated up to 1200 °C with a heating rate of 5 °C /min in air.

Microstructural changes have also been discussed in terms of polished microstructure and fracture surface images. After each experiment, pellets were ground using 2-propanol as coolant and their crystal structures were determined by using Rigaku MiniFlex 600 X-ray diffractometer (XRD) with a scan speed of 1°/min and step size of 0.02° by using Cu K_α. For the scanning electron microscopy (SEM) investigations, the pellets were first ground up to 2000 grit SiC papers. Secondly, as prepared pellets were polished using appropriate polishing media (AKASEL – DiaDoublo Water Free 0.25 Micron Diamond Suspension) before microstructural analysis. Then, microstructural and elemental analyses of each pellet were carried by SEM (Zeiss SUPRA 50VP) attached with an energy dispersive spectrometer (EDS-Oxford INCA). Due to the surface ion-exchange when LLZO is contacting with water [5], water usage was avoided in any treatment of the pellets.

Potentiostatic polarization method was used to determine electrical conductivity of the pellets. The effect of sintering time on the electronic conductivity of stabilised

cubic phase were focused on the 30 mole % Al containing LLZO samples sintered at 12 and 24 h. As a control experiment, 36 h-sintered pellet was also conducted in order to see the electrical conductivity changes as a function of microstructure. All measurements were carried out by using Galvanostat/Potentiostat system (Gamry Reference 600) with a minimum current resolution of 20 aA. Pellets were cut into the dimensions of 5mm length x 5mm width. Both surfaces were coated with Silver paste to provide a contact between Ni electrodes and the pellets. 10 Volts were applied and kept for a sufficient time (10000 seconds) to stabilize current values.

2.3. Results & Discussion

2.3.1. Thermal behavior of precursor powders

Before calcination, thermal behavior of mixture of starting precursors was investigated by TG (Figure 2.1).

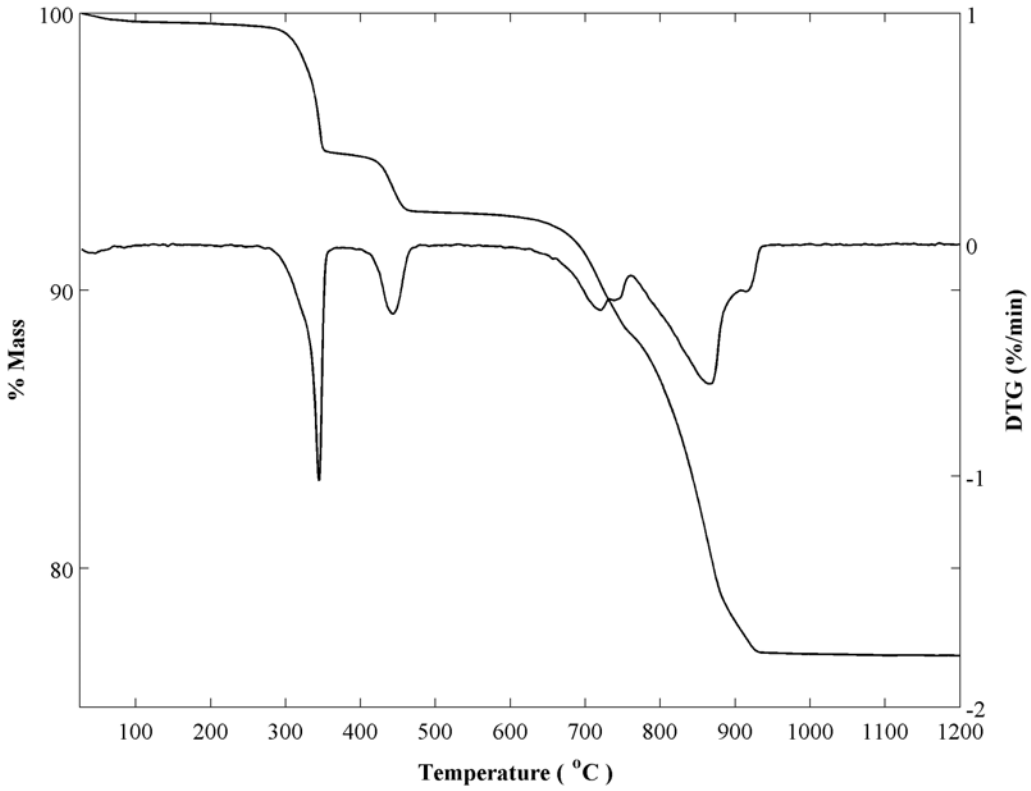

Figure 2.1. *TG and DTG curves of mixed precursor powders*

When temperature increased to 250 °C, a minute amount of weight loss was observed which corresponds to physical water loss. Then, there were 2-step weight loss in the temperature range of 300 °C to 500 °C and the DTG curve showed two fairly sharp peaks. These peaks correspond to hygroscopic water loss from La_2O_3 powder in the mixture. La_2O_3 powder converts into $La(OH)_3$ in the presence of air or water. Two peaks corresponding to weight losses in the range of 300 °C to 500 °C were caused by the following reactions respectively [28].

$$La(OH)_{3(s)} \rightarrow LaOOH_{(s)} + H_2O_{(g)} \quad (2.2)$$

$$LaOOH_{(s)} \rightarrow La_2O_{3(s)} + H_2O_{(g)} \quad (2.3)$$

The sharp peak at around 720 °C is due to the melting of Li_2CO_3 in the mixture [29]. The weight losses which corresponds to gaseous CO_2 losses from thermal decomposition of Li_2CO_3, starts at the same time of melting and continues gradually until 920 °C. The reaction of thermal decomposition is as follows:

$$Li_2CO_{3(l)} \rightarrow Li_2O_{(s)} + CO_{2(g)} \quad (2.4)$$

In the temperature range of 920 °C – 1200 °C, there was a very small weight loss which belongs to Li losses at high temperatures.

2.3.2. Determination of existing phases after calcination

Figure 2.2 shows the XRD patterns of the pellets which was sintered at both 1150 °C and 1230 °C for 12 h without Al addition.

Figure 2.2 showed that for pellets sintered at 1150 °C, tetragonal LLZO (PDF Card No: 01-078-6708), Li_2ZrO_3 (PDF Card No: 01-070-8744), Pyrochlore $La_2Zr_2O_7$ (PDF Card No: 01-071-2363) phases were present. However, if the temperature was increased to 1230 °C which is the temperature of cubic stabilization reported elsewhere [25], the structure turns mostly out to the cubic LLZO (PDF Card No: 00-063-0174) with a minute amount of $La_2Zr_2O_7$. Note that, there are three discrete peaks between 2θ=50 to 55° in cubic structure whereas six peaks are visible in tetragonal structure, because of the crystallographic symmetry differences between cubic and tetragonal. Figure 2.3 presents the XRD patterns of 20, 25 and 30 mole % Al containing LLZO pellets sintered at 1100 and 1150 °C for 12 and 24 hours.

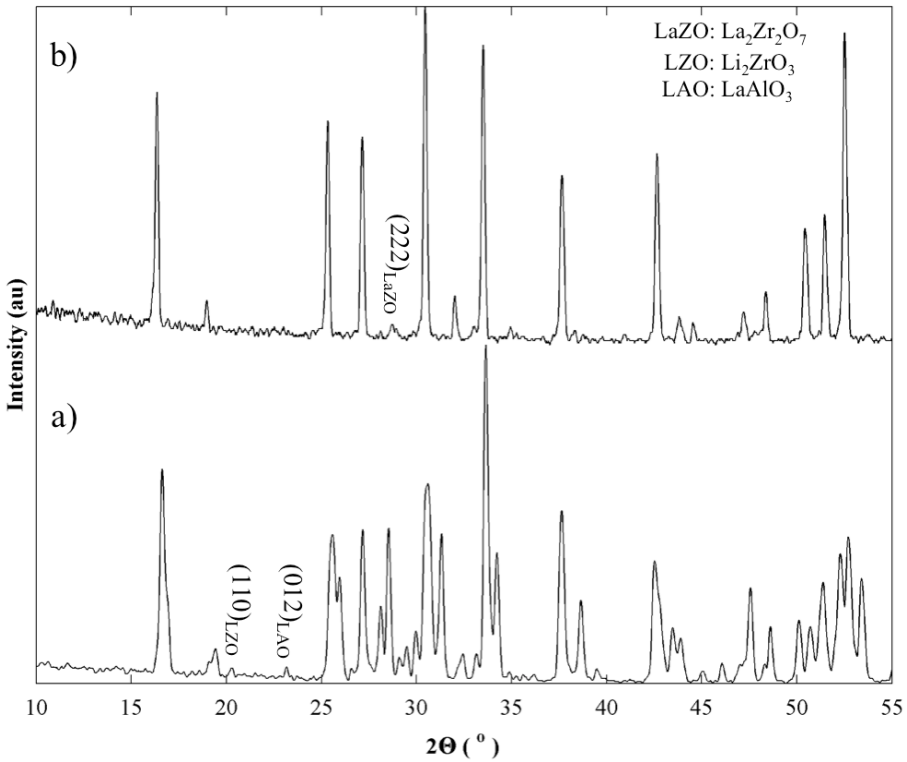

Figure 2.2. *XRD patterns of the pellets sintered at 1150 (a) and 1230 °C (b) for 12 h without Al addition*

Small peak shifts in Figure 2.3 is due to the experimental conditions. XRD results of 20 mole % Al containing LLZO pellets showed that samples sintered at 1100 °C for 12 and 24 hours have 3 discrete peaks between 2θ=50 to 55° with a significant background. It's believed that contribution of tetragonal LLZO peak doublets' causes the background and a mixture of tetragonal and cubic LLZO peaks were seen together. However, if the sintering temperature was increased to 1150 °C, all of the peaks can be indexed as cubic LLZO phase and the background between 2θ=50-55° was also reduced.

XRD patterns of 25 mole % Al containing LLZO pellets are shown in Figure 2.3 (e) - (h). In comparison to 20 mole % Al containing LLZO pellets, Figure 2.3 (e) and (f) showed a minute amount of $LaAlO_3$ at the similar sintering temperature and time. At lower sintering temperatures of even 1100 °C, cubic LLZO phase can be stabilized. On the other hand, if Al content is increased to 30 mole %, unreacted products disappear as shown in Figure 2.3 (i) - (l). The remaining peaks are indexed as cubic LLZO.

To summarize the findings given above, minimum of 1230 °C sintering temperature is needed if Al was not added.

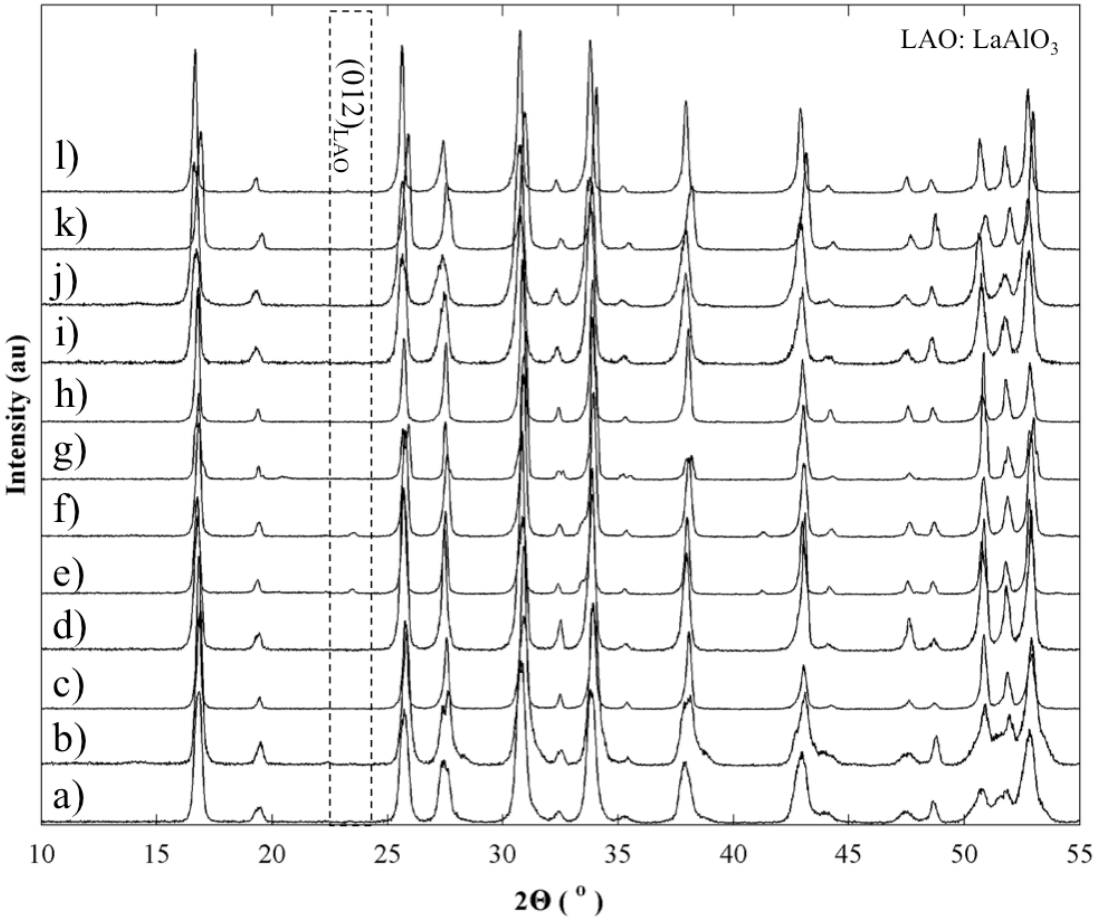

Figure 2.3. *XRD patterns of 20 mole % Al containing LLZO pellets sintered at 1100 °C for 12 h (a), 24 h (b) and 1150 °C for 12 h (c), 24 h (d); 25 mole % Al containing LLZO pellets sintered at 1100 °C for 12 h (e), 24 h (f) and 1150°C for 12 h (g), 24 h (h); 30 mole % Al containing LLZO pellets sintered at 1100 °C for 12 h (i), 24 h (j) and 1150 °C for 12 h (k) and 24 h (l)*

However, Al addition up to 30 mole % could lower the stabilization temperature to 1100 °C., sintering conditions of 1100 °C – 12 h is not enough to fully stabilize cubic phase for all different Al contents. In contrast, if sintering time was increased to 24 h; 20 and 25 mole % Al containing LLZO can be stabilized with the presence of small amount of tetragonal phase. Additionally, for 1150 °C sintering temperature, cubic LLZO phase was stabilized for all different sintering times.

2.3.3. Microstructural evaluation

Microstructures of polished samples were investigated for 12 h and 24 h sintering times at different temperatures by using backscattered electron (BSE) imaging technique in SEM (Figure 2.4).

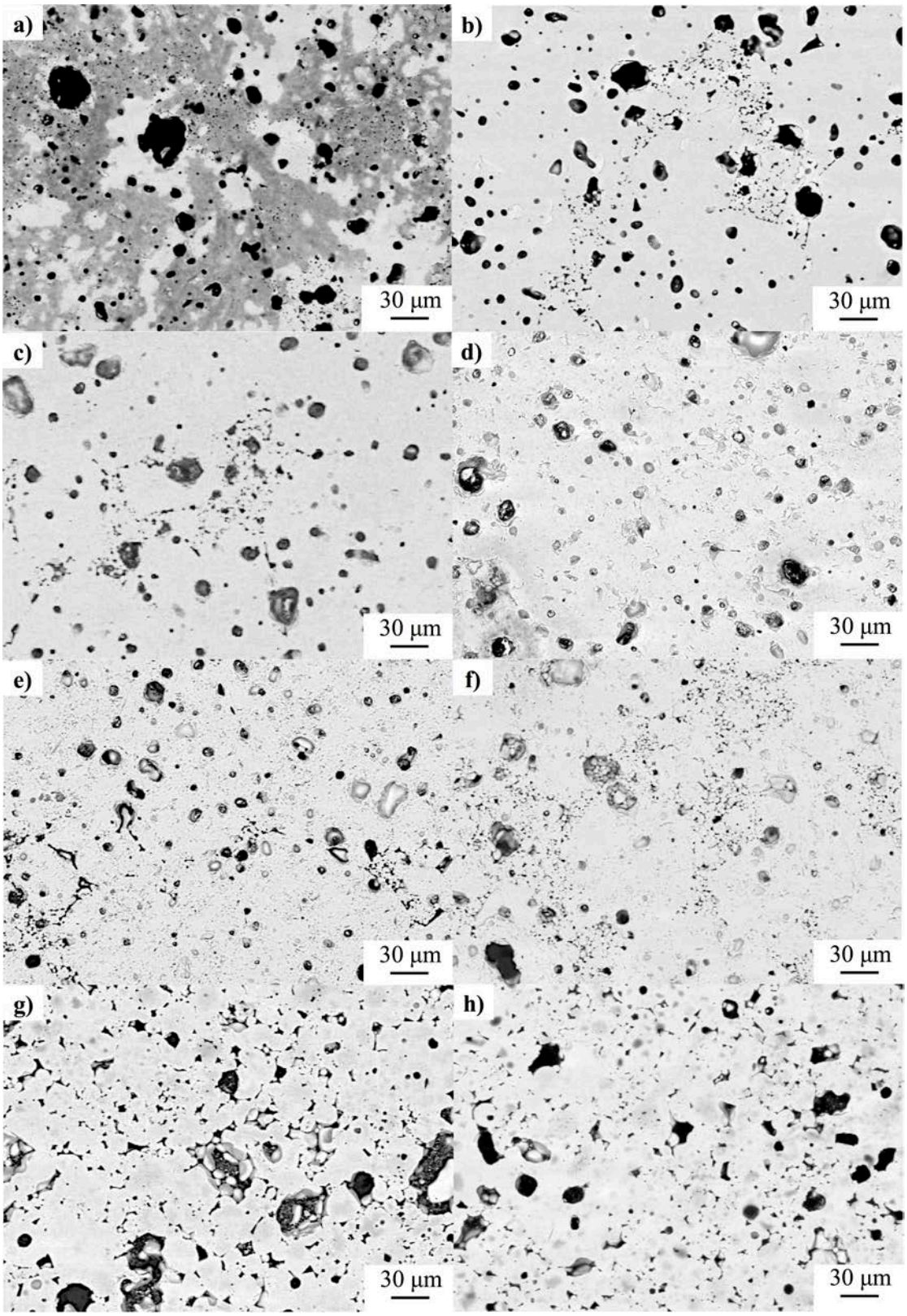

Figure 2.4. *BSE images obtained from 20 mole % Al containing LLZO pellets sintered at 1100 °C for 12 h (a), 24 h (b) and 1150 °C for 12 h (c), 24 h (d); 25 mole % Al containing LLZO pellets sintered at 1100 °C for 12 h (e), 24 h (f) and 1150 °C for 12 h (g), 24 h (h); 30 mole % Al containing LLZO pellets sintered at 1100 °C for 12 h (i), 24 h (j) and 1150°C for 12 h (k) and 24 h (l)*

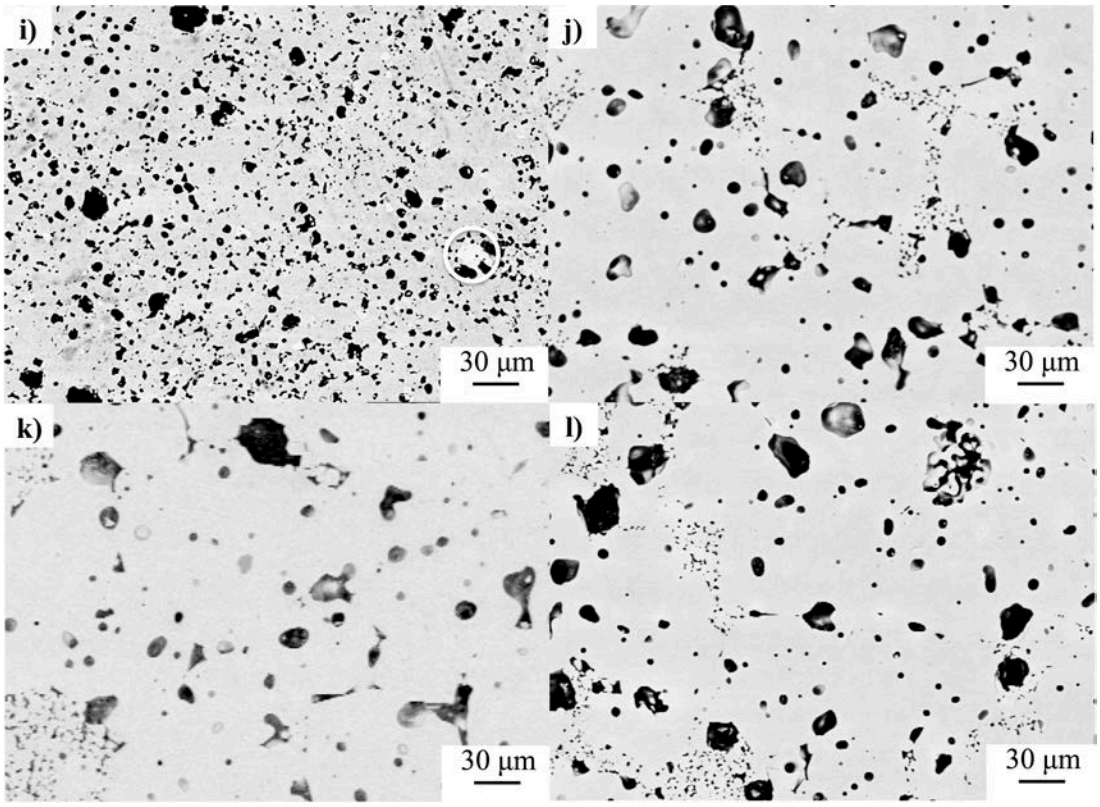

Figure 2.4. (continued) *BSE images obtained from 20 mole % Al containing LLZO pellets sintered at 1100 °C for 12 h (a), 24 h (b) and 1150 °C for 12 h (c), 24 h (d); 25 mole % Al containing LLZO pellets sintered at 1100 °C for 12 h (e), 24 h (f) and 1150 °C for 12 h (g), 24 h (h); 30 mole % Al containing LLZO pellets sintered at 1100°C for 12 h (i), 24 h (j) and 1150 °C for 12 h (k) and 24 h (l)*

Figure 2.4 showed that, as-sintered pellets have fairly porous microstructure. In Figure 2.4 (a), dark grey and light grey areas are observed with highly porous microstructure. There are two types of pores: (*i*) pores formed because of evaporation of gaseous substances and (*ii*) pores formed due to the incomplete sintering at grain junctions.

Pores formed because of evaporation of gaseous species such as gaseous residuals or Li losses at high temperature treatment are mostly spherically shaped and seen within the grains (1st type). In contrast 2nd type of pores were formed due to the incomplete sintering at the grain junctions. They are shapeless intergranular voids.

The main driving force for eliminating 2nd type of pores is diffusion. When the sintering time increases to 24 h, pores start to become rare and segregate in the grain junctions forming the 2nd type of pores as shown in Figure 2.4 (b). This phenomena was not only observed by increasing sintering time, but also by increasing sintering temperature to 1150 °C. For the samples sintered at 1150 °C for 12 h, less but still

existing 2nd type of pores are seem to segregate at the grain junctions (Figure 2.4 (c)). However, when the sintering time was increased to 24 h at 1150 °C, 2nd type of pores were not observed in the microstructure (Figure 2.4 (d)). But, 1st type of pores were still present in the microstructure with a fully stabilized cubic LLZO structure.

25 mole % Al containing LLZO microstructures are shown in Figure 2.4 (e) – (h). Compared to Figure 2.4 (a), there is no phase contrast at 1100 °C sintering temperature for 12 h sintering time. However, highly porous microstructure with both 1st and 2nd type pores were observed. Less amount of 2nd type of pores were also clearly seen at 1100 °C sintering temperature for 24 h sintering time (Figure 2.4 (f)). On the other hand, at 1150 °C sintering temperature, all the pores were almost disappeared even for 12 h sintering time (Figure 2.4 (g)). The microstructure in Figure 2.4 (h) is the same with the microstructure in Figure 2.4 (g). However, grains were larger.

Figure 2.4 (i) – (l) shows 30 mole % Al containing LLZO microstructures. When the sintering time doubled, 2nd type of pores were dramatically decreased, whereas 1st type of pores decreased less. However, when the sintering temperature were increased to 1150 °C, important amount of 1st type of pores were also disappeared. On the other hand, 2nd type of pores were decreased less and distributed non-homogeneously because of grain growth and densification during sintering. Grain size was increased.

EDS point analysis was conducted in order to compare the stoichiometry of different grains in the microstructure and given in the Table 2.1. In Figure 2.4 (i), some of white regions connected to the porosities were seen. One of them marked with a circle in Figure 2.4 (i) and its elemental analysis was also presented in Table 2.1.

Table 2.1. *SEM-EDS point analysis from the polished surfaces*

Sintering Temperature (°C)	Sintering Time (h)	Mole % ratio Al/La/Zr	Notes
1100	12	0.24/3.04/2.02	
1100	12	1.19/1.00/0.00	Area in circle
1100	24	0.24/2.94/2.11	
1150	12	0.26/2.99/2.05	
1150	24	0.26/3.03/2.18	

From the Table 2.1, it can be deduced that apart from the circled area, all of the measurements were very near to stoichiometric Al:La:Zr ratio for the LLZO phase. But, bright region in circle did not contain Zr, which is probably $LaAlO_3$ compound. It's believed that $LaAlO_3$ is not common since it is not detected by using XRD assuming

that it is not in amorphous structure. The phase diagram is calculated from FactSage 7.0 (data not given) and it was found that at these sintering temperatures, $LaAlO_3$ is in a liquid form and during sintering it can easily fill the porosities.

In Figure 2.5, elemental mapping from the 30 mole % Al containing sample sintered at 1100 °C for 24 h was given.

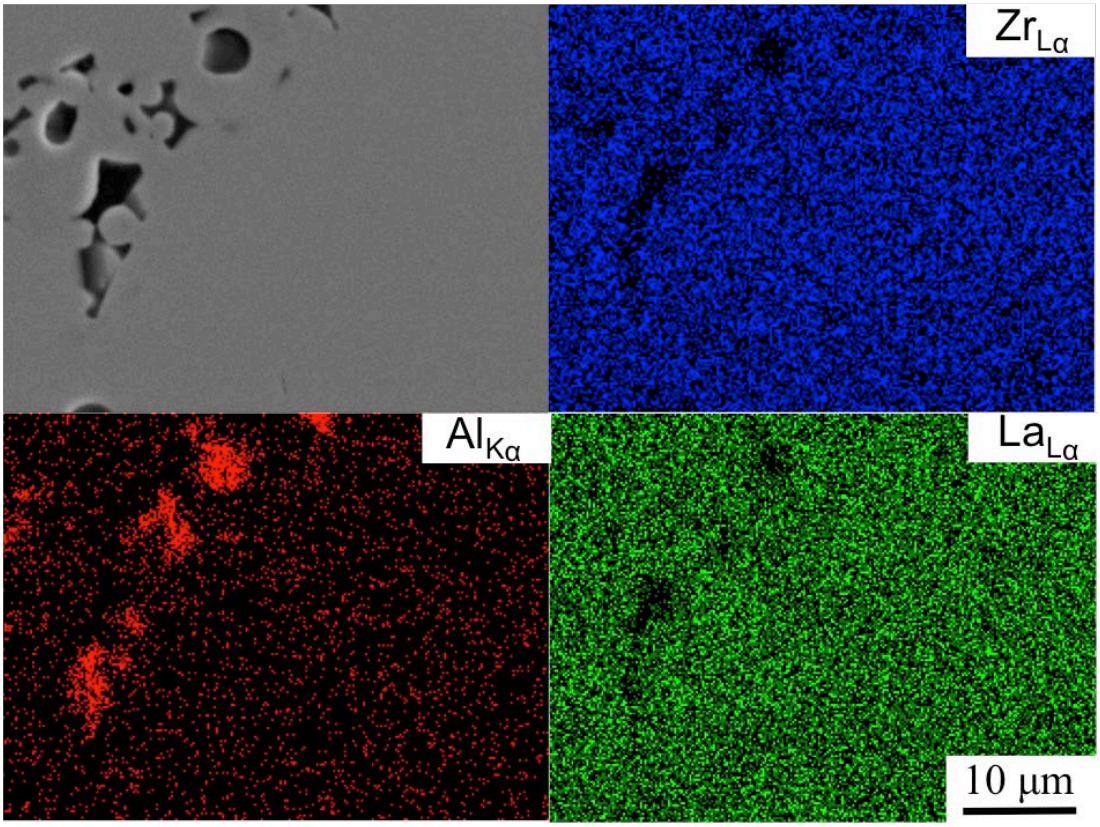

Figure 2.5. *BSE-SEM image and SEM-EDS mapping of pellet sintered at 1100 °C for 24 h*

La, Al and Zr are homogeneously distributed for entire pellet whereas Al map showed highly concentrated Al deposits within the black regions in the BSE image. There might be two possible reasons about Al segregation phenomena. Firstly, liquid Al-bearing substances can exist in the porosities at sintering temperatures and after cooling it may remain at the porosities. Secondly, Li can be replaced by Al as it was explained in somewhere else [26]. At high temperatures, Li losses result in Li vacancies, which is likely to be filled by Al atoms. As Li is lost from the porosities, Al will fill the Li vacancies creating Al-rich regions in the microstructure.

In order to investigate the cause of contrast observed in the Figure 2.4 (a), EDS point analysis were taken from the regions numbered as 1 and 2 in Figure 2.6.

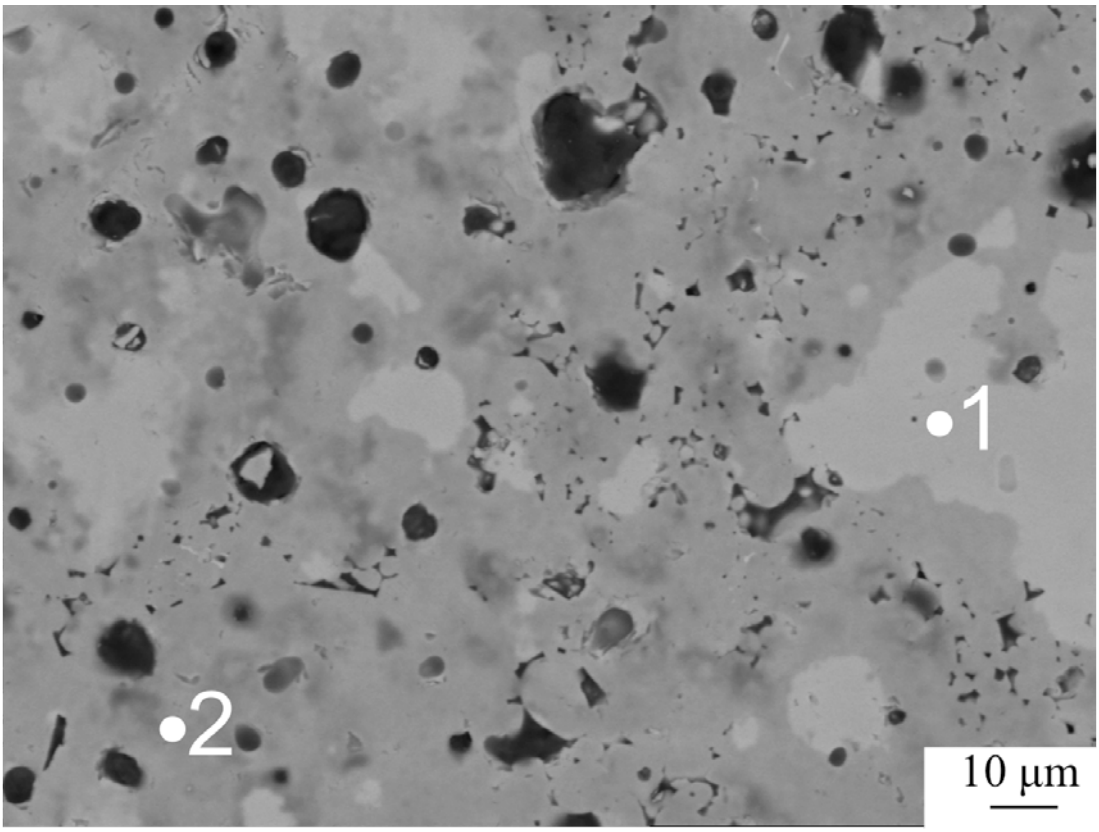

Figure 2.6. *EDS point analysis taken from two different regions having a different contrast*

Results showed that brighter regions denoted as Point 1 has 1.0/21.4/14.6 (Al/La/Zr) ratio whereas dark regions denoted as Point 2 has 0.0/21.7/15.2 (Al/La/Zr). Due to the atomic weight differences between Al and Li, average atomic weight is much higher at the bright regions. Thus, Al containing regions appear bright in comparison to Li containing areas. In the light of Al-Li substitution phenomena explained above, Li deficit region contains Al.

Fracture surface images of 20 to 30 mole % Al containing LLZO pellets are shown in Figure 2.7.

Similar to polished samples, from the fractured surfaces, it can be seen that these material also contain both 1st and 2nd type of pores. Some of the pores within the grains are interconnected. The particle size of the grains ranges from 20 – 50 μm for all the samples.

Similar to polished samples, from the fractured surfaces, it can be seen that these material also contain both 1st and 2nd type of pores. Some of the pores within the grains are interconnected. The particle size of the grains ranges from 20 – 50 μm for all the samples.

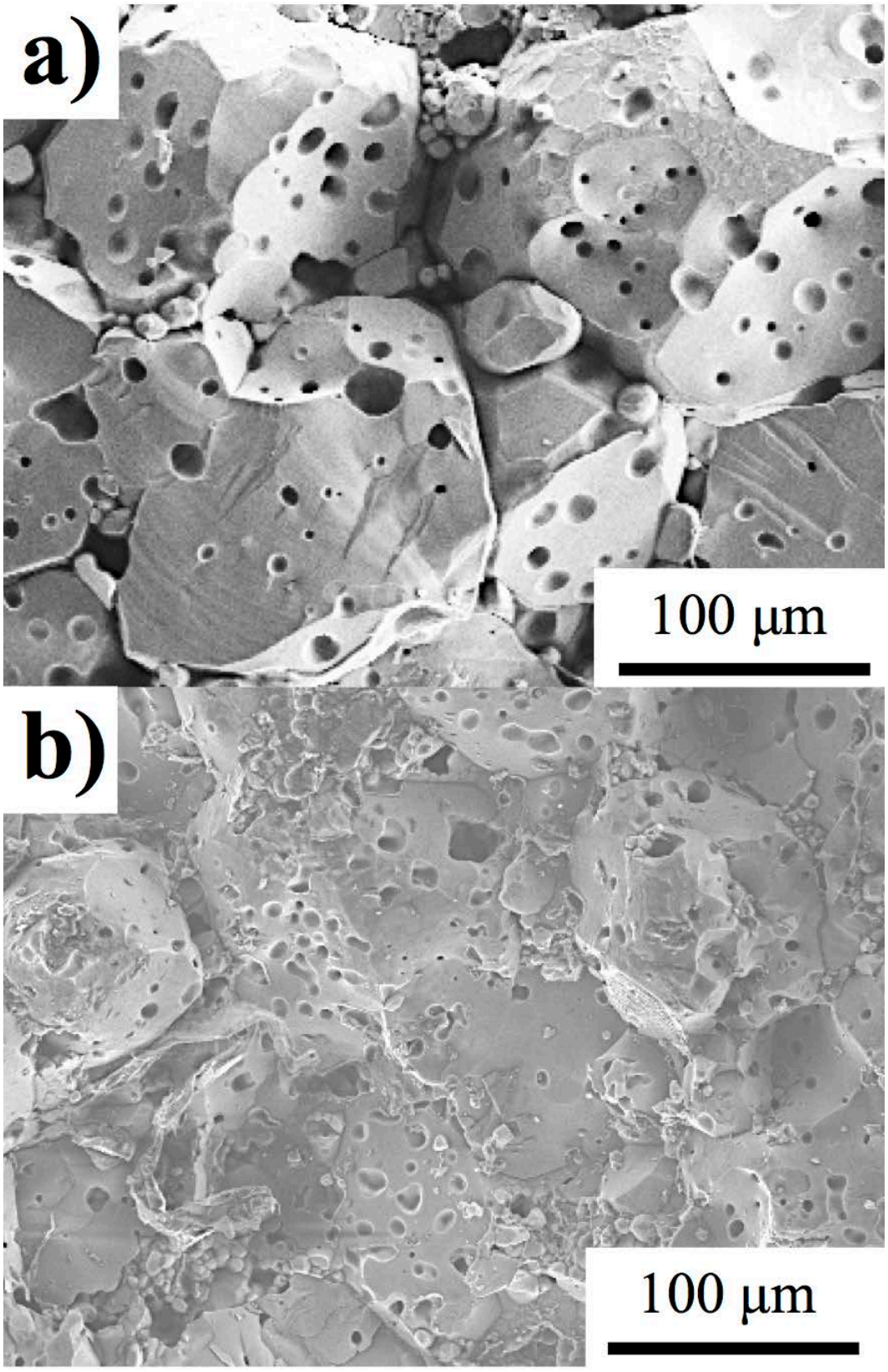

Figure 2.7. *Secondary electron images obtained from the fractured surfaces of the pellets containing: a) 20 mole %, b) 25 mole % and c) 30 mole % Al sintered at 1100 °C for 12 h*

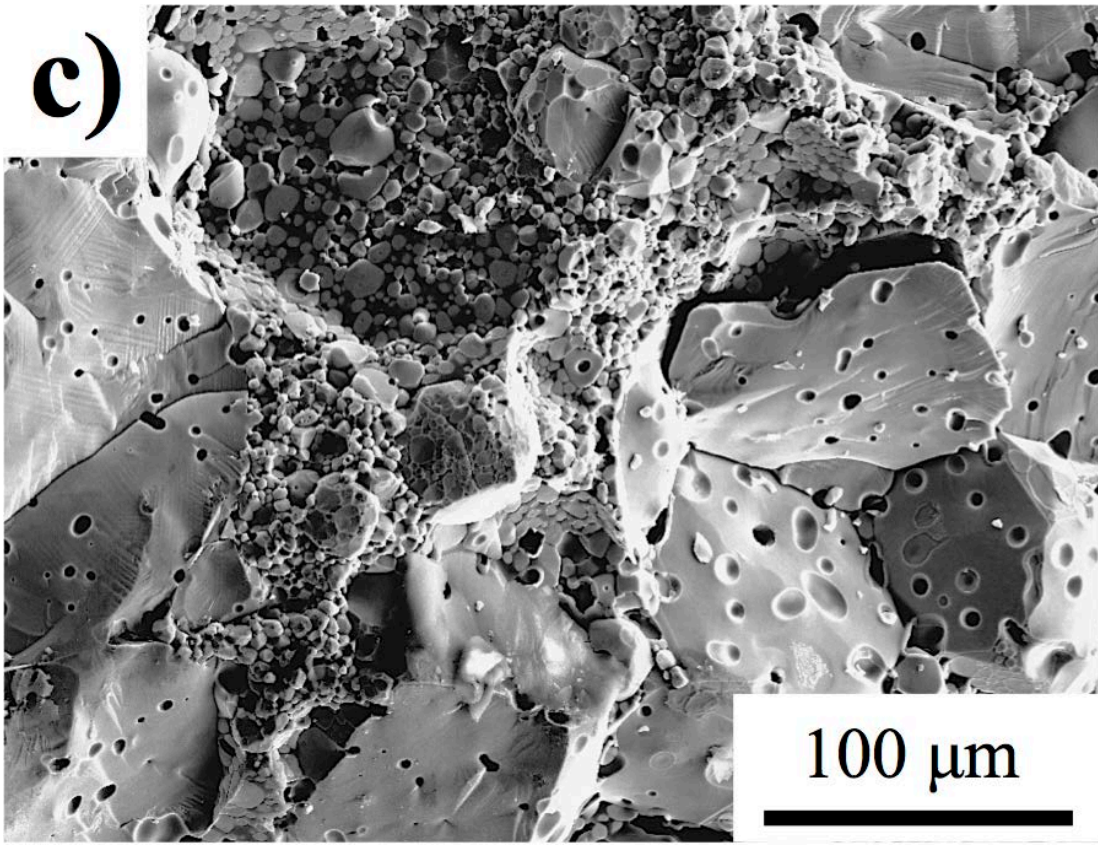

Figure 2.7. (continued) *Secondary electron images obtained from the fractured surfaces of the pellets containing: a) 20 mole %, b) 25 mole % and c) 30 mole % Al sintered at 1100 °C for 12 h*

2.3.4. The effect of sintering time on the electrical conductivity of 30 mole % Al containing LLZO

Electrolytes should have the lowest electronic conductivity to prevent self-discharge of batteries. Low electronic conductivity also enhances shelf life. Electronic conductivity is also an important factor to determine ionic transport number which determines whether electrolyte is ionic or mixed conductor. Ionic transport number can be defined by the ratio of total ionic conductivity, which is not part of this chapter, and sum of electrical and ionic conductivities. If electronic conductivity is low, ionic transport number will approach to 1.0 and the electrolyte behaves like ionic conductor. However, if electronic conductivity is high, ionic transport number will diverge from 1.0 and the electrolyte tends to be mixed conductor. For the purpose of determining the DC conductivity, 30 mole % Al containing LLZO sintered at 1150 °C for 12, 24 and 36 hours and the fractured surface SEM images were presented in Figure 2.8.

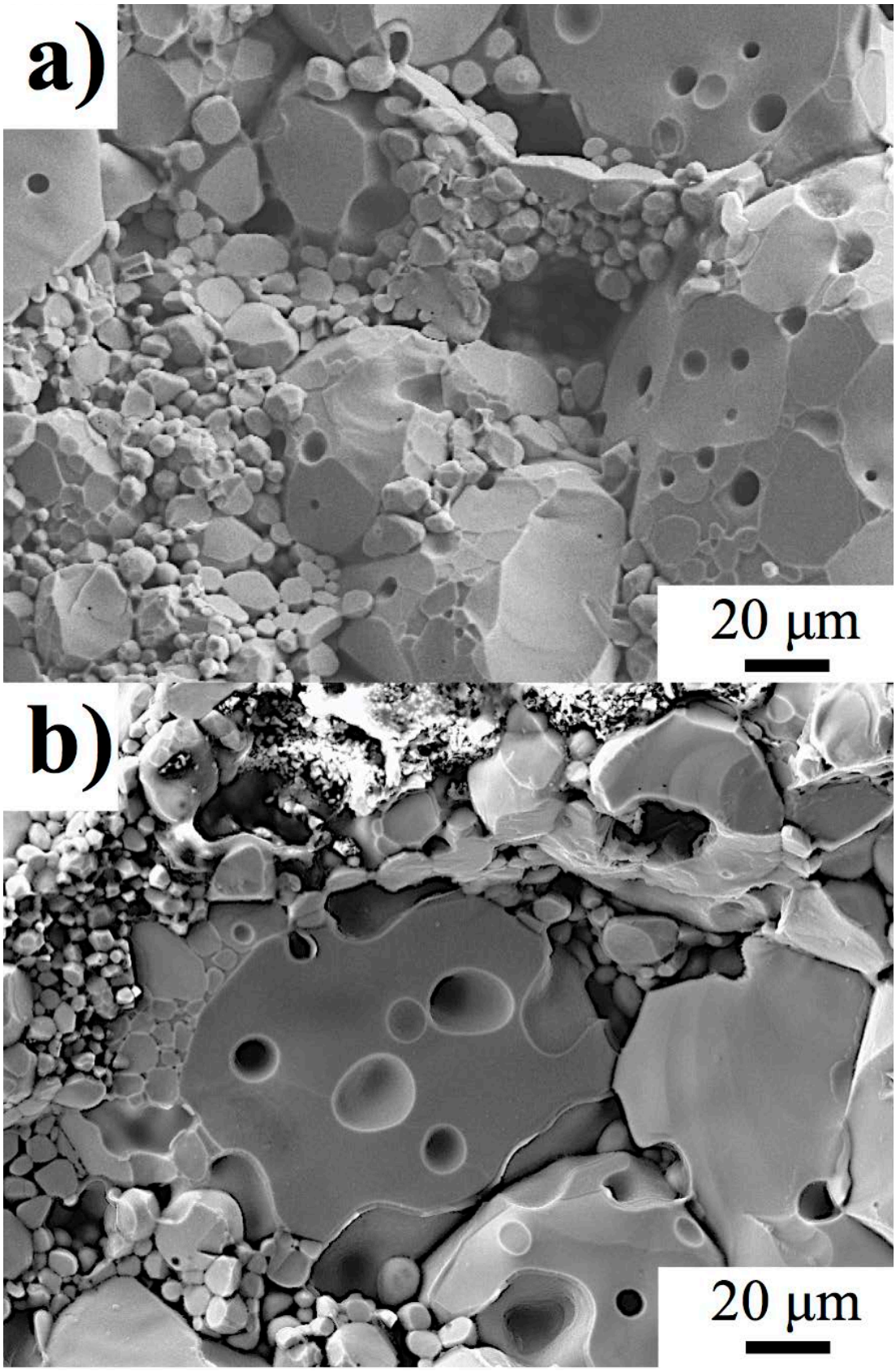

Figure 2.8. *Secondary electron images obtained from the fractured surfaces of the pellets of 30 mole % Al containing LLZO sintered at 1150 °C for: a) 12 h b) 24 h and c) 36 h*

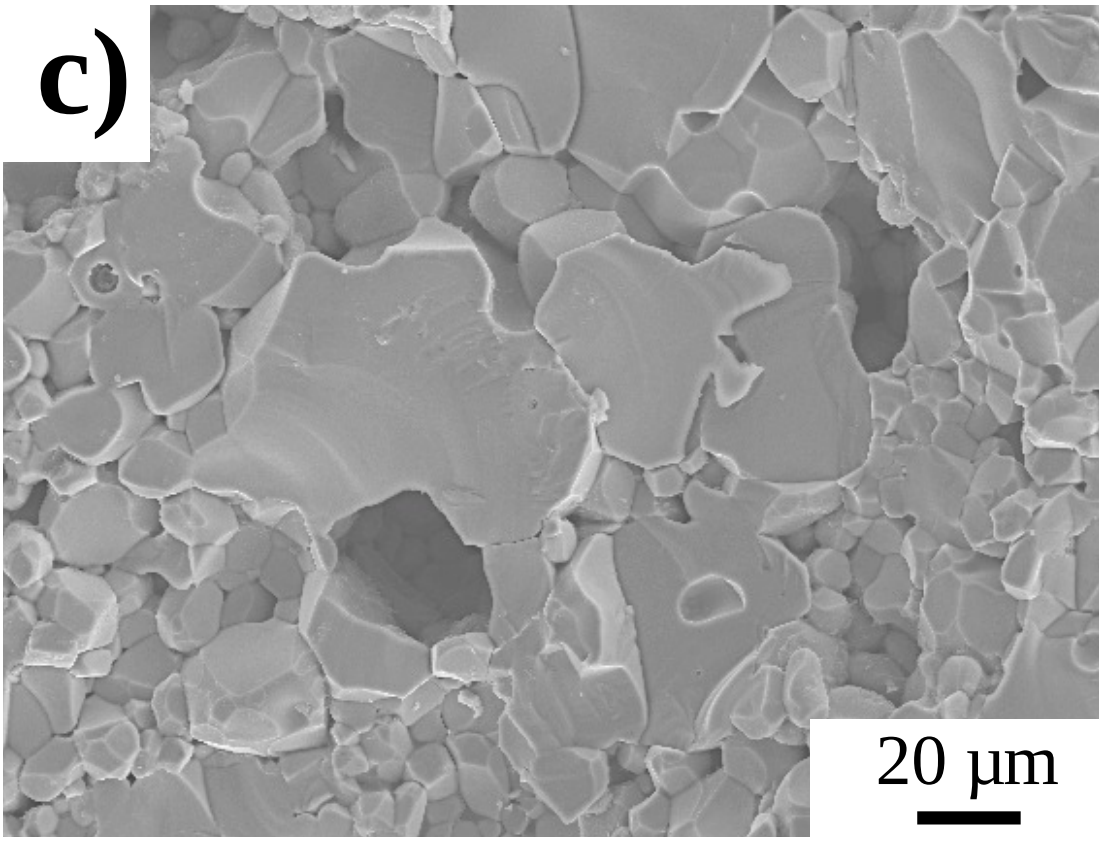

Figure 2.8. (continued) *Secondary electron images obtained from the fractured surfaces of the pellets of 30 mole % Al containing LLZO sintered at 1150 °C for: a) 12 h b) 24 h and c) 36 h*

Big grains (primary grains) are highly porous and surrounded by small grains (secondary grains) deposited at grain boundaries in Figure 2.8 (a). However, when the sintering time was increased up to 24 h, as shown in Figure 2.8 (b). Pores within the grains were reduced. There are also small grains deposited at the grain boundaries detectable (Figure 2.8 (b)). However, when the sintering time was increased to 36 h, nearly fully dense primary (Figure 2.8 (c)) There was no distinction between primary and secondary grains. Both intergranular and transgranular fracture can be seen in Figure 2.7 and Figure 2.8.

In the light of findings so far, cubic stabilization steps in terms of the microstructural changes can occur by (*i*) melting of aluminate compounds, (*ii*) filling the pores by liquid compounds, (*iii*) formation of Al rich regions around pores that makes the contrast difference, (*iv*) Al diffusion through the entire pellet and (*v*) grain growth and densification.

The most dense and pure pellets are obtained from 30 mole % Al containing pellets sintered at 1150 °C. Therefore, electronic conductivities of only 30 mole % Al containing LLZO sintered at 1150 °C were measured (Table 2.2).

Table 2.2. *DC conductivities of 30 mole % Al containing LLZO pellets sintered at 1150 °C for 12, 24 and 36 hours*

Sintering Temperature (°C)	Sintering Time (h)	Crystal Structure	DC Conductivity (S/cm)
1150	12	Cubic	3.77×10^{-8}
1150	24	Cubic	6.67×10^{-9}
1150	36	Cubic	6.95×10^{-9}

As it can be seen from the Table 2.2, when the sintering time is increased from 12 h to 24 h, the electronic conductivity was decreased dramatically. The pellet sintered for 12 h shows more mixed conductor behavior than the pellet sintered for 24 h. However, there is no significant change between 24 h and 36 h sintering time.

To sum up the findings above, the cubic phase stabilization of 20 to 30 mole % Al containing LLZO sintered at 1100 and 1150 °C for 12 h to 36 h were investigated. XRD results showed that all samples contained large amount of cubic LLZO phase under all synthesis conditions. On the other hand, fully stabilized cubic LLZO material was obtained at 1150 °C for 24 h sintering time. BSE images supported by elemental analysis from polished surface clarify that, little amount of other phases such as $LaAlO_3$ compounds, below the detection limit of XRD may be present in the samples. Al containing phases were observed within porosities in the sample sintered at 1100 °C for 24 h by using elemental maps of the polished surfaces. 1^{st} type of pores that are identified at grains due to the presence of gaseous residuals. When sintering time was increased, the porosities tend to be decreased. According to the fracture surface images, density of the pellets is not affected dramatically by increasing Al content. Out of 30 mole % Al containing samples, the lowest electronic conductivity was obtained from LLZO sintered at 1150 °C for 24 h and selected as the best solid electrolyte in this chapter in terms of its self discharge and ionic conduction behavior.

On the other hand, the synthesis conditions have some of disadvantages in a technological manner. Some of the disadvantages are as follows:

- A slow heating-cooling rate (2°C/min) was used.

- 2 individual calcination steps were required.
- A minimum of 24 hours sintering time is needed.

For the purpose of reducing calcination steps, thermal analysis of powders after each calcination step was firstly conducted. TG/DTG curves after each calcination were depicted in Figure 2.9.

The main weight loss in both Figure 2.9 (a) and (b) was observed until 100 °C and can be attributed to the evaporation of humidity. It can be understood from the Figure 2.9 that approximately same amount of weight losses (5-6 %) was seen. The main reason for slight differences are due to air and water absorption in open-air conditions. The peaks and corresponding weight losses related on $La(OH)_3$ and Li_2CO_3 decompositions were identical. Thus, an additional calcination step is useless since the weight loss after calcinations is not significantly reduced meaning that decompositions were almost completed.

2.3.5. The effect of heating rate on solid-state synthesis of $Li_7La_3Zr_2O_{12}$

Because of the highly volatile nature of Lithium, synthesis of Lithium containing materials should be carefully handled. In order to carefully control the Lithium losses, heating rate should be taken into account. However, there are lots of heating rate used during synthesis of LLZO. Besides, the effect of heating rate is still yet to be explained. Table 2.3 showed the examples of different heating rates used in LLZO synthesis.

Table 2.3. *Heating rates of solid-state reaction synthesized LLZO*

Research Group	***Heating Rate (°C/min)***	***Reference***
Murugan et. al.	1	[25]
Kotobuki et. al.	1	[30]
Sakamoto et. al.	1.67	[31]
Bai et. al.	2-5	[32]
Cao et. al.	2 & 3	[33]
Rao et. al.	2.15	[34]
Yang et. al.	3	[35]
Rettenwander et. al.	5	[36]
Li et. al.	5	[37]
Ren et. al.	10	[29]
Larraz et. al.	10	[38]

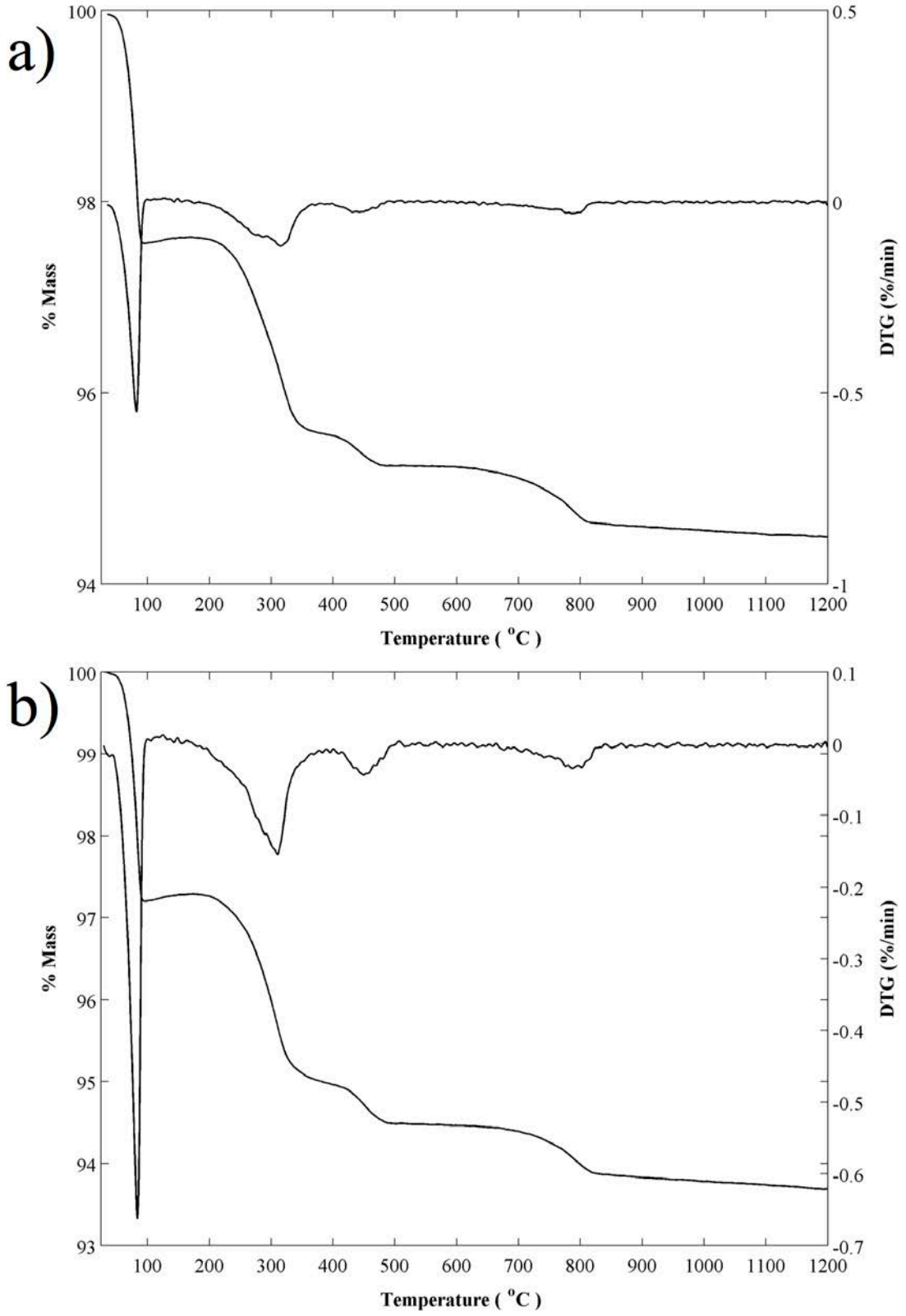

Figure 2.9. *TG/DTG curves of powders after calcination at (a) 900 °C (b) 980 °C (b)*

As it can be seen from the Table 2.3 that very wide range of heating rate was used for the LLZO synthesis until now. However, there's a lack of the study which investigates the effect of heating rate in a technological manner.

The thermal behavior of the precursors powders at 5 and 10 °C/min heating rates was evaluated and the TG curves comparing the different heating rates were presented in Figure 2.10.

The corresponding weight losses in Figure 2.10 were discussed in detail in Section 2.3.1. However, a special attention should be paid on the remaining mass percentage at different heating rates. Until 300 °C, the weight loss was higher at 10 °C/min heating rate. The reason of this behavior was attributed to hygroscopic behavior of the precursors. During slow heating at a rate of 5 °C/min, a minute amount of the released humidity could be recaptured by the both Li_2CO_3 and La_2O_3 powders. No weight loss change could be observed related to the residual $La(OH)_3$ and Li_2CO_3 thermal decomposition. At a heating rate of 10 °C/min, reactions were completed and no weight loss were obtained after 1000 °C.

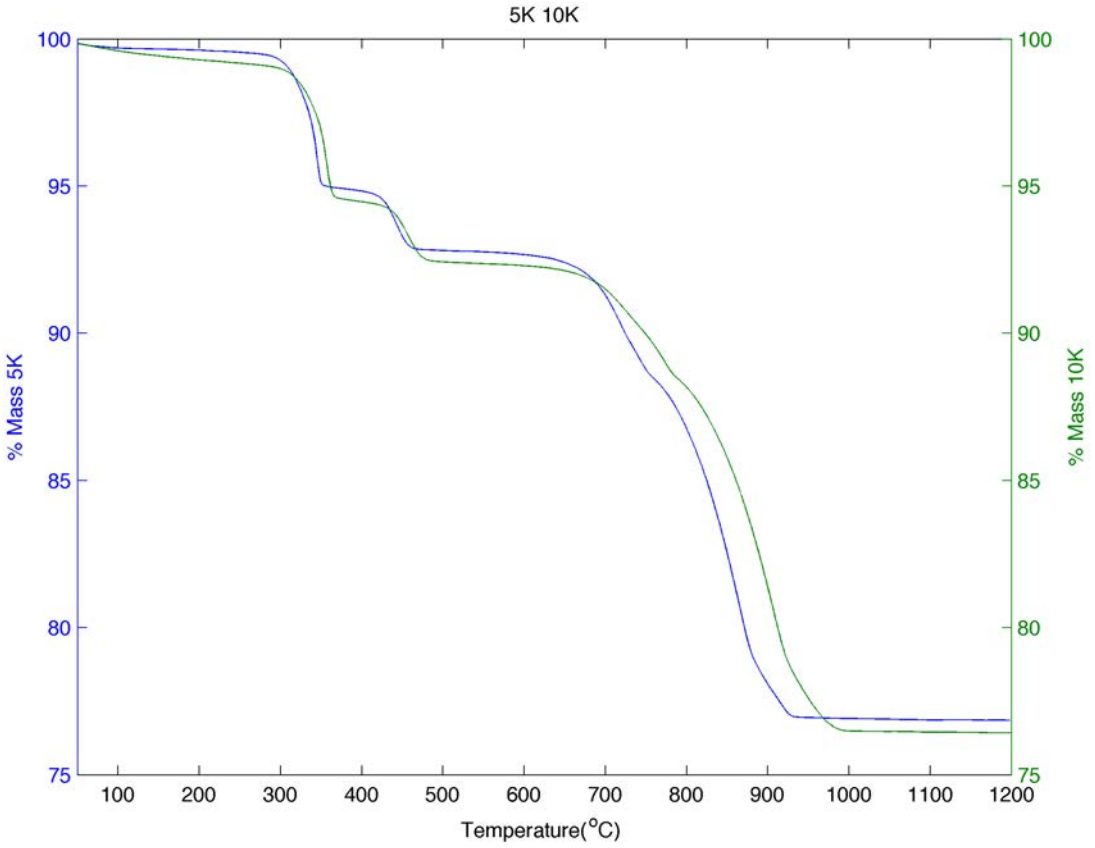

Figure 2.10. *TG curve of precursor powders at 5 and 10 °C/min heating rates*

The details of the synthesis method was explained in Section 2.2. Unlike Section 2.2, the single-step calcination were used and the calcination temperature were set at 1000 °C with a heating rate of 10 °C/min according to the findings in Figure 2.9 and Figure 2.10.

Figure 2.11 showed the XRD patterns of LLZO powders calcined at 1000 °C for 6 hours with 2, 5 and 10 °C/min.

There are two important points that must be mentioned during discussion of the findings in Figure 2.11. First of all, when the heating rate was selected as 2 and 5 °C/min, there were remnants of cubic LLZO phase within the structure. But tetragonal LLZO phase was found as dominant phase when 10 °C/min heating rate was used. Total heat treatment times calculated were approx. 22.3, 12.5 and 9.3 hours for 2, 5 and 10 °C/min heating rates, respectively.

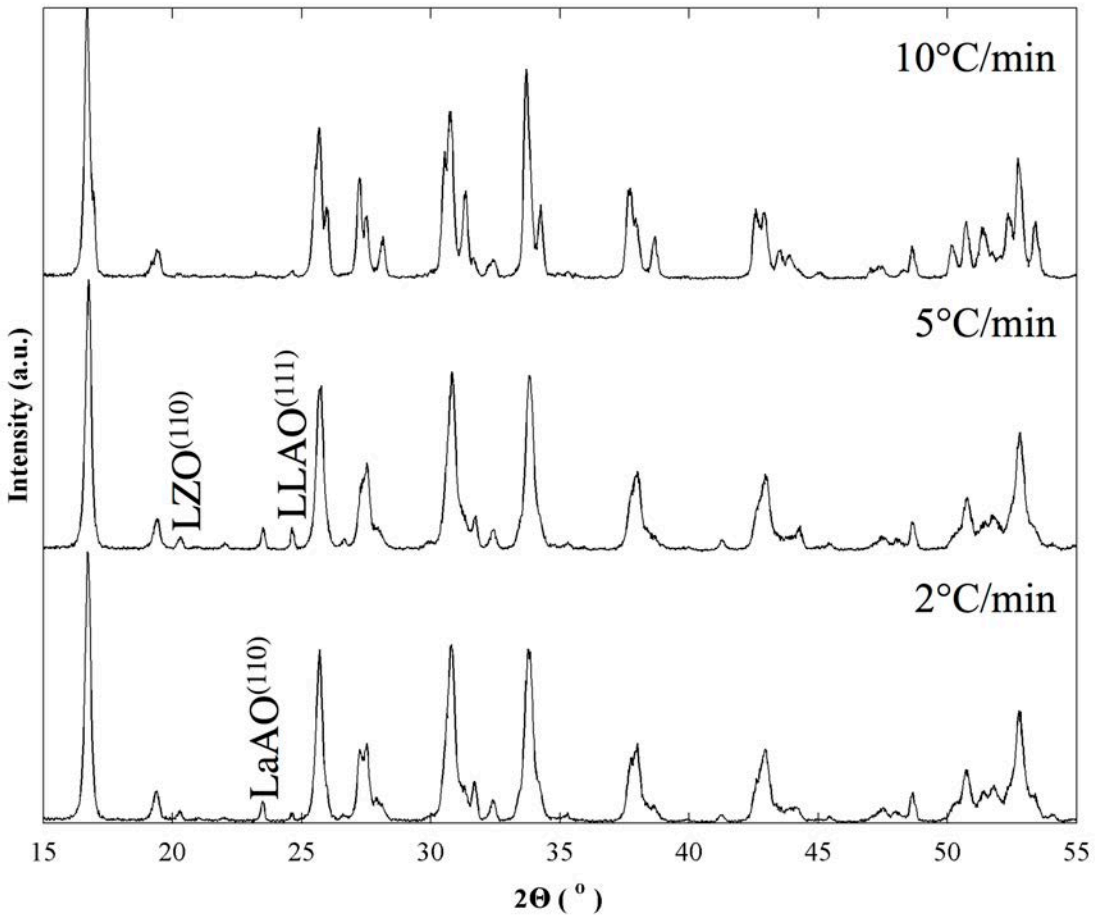

Figure 2.11. *XRD patterns of LLZO powders after calcination at 1000 °C for 6 hours with 2, 5 and 10 °C/min*

Since tetragonal to cubic phase transformation was a time requiring reconstructive phase transition, a longer heat treatment time resulted with a more presence of cubic LLZO phase.

In the impurity phase perspective, Li_2ZrO_3, $LaAlO_3$ and $La_2Li_{0.5}Al_{0.5}O_4$ were detected as the main impurity phases. The highest amount of impurity phases were observed in 5 °C/min. The amount of Li_2ZrO_3 was increased when the heating rate was increased from 2 °C/min to 5 °C/min. On the other hand, it was reduced dramatically when the heating rate was set to 10 °C/min. Besides, very small increase was observed for $LaAlO_3$ when the heating rate was increased to 5 °C/min. But, it was reduced dramatically when the heating rate was set to 10 °C/min. $La_2Li_{0.5}Al_{0.5}O_4$ which was a triple phase solution of $La_2O_3.Li_2O.Al_2O_3$, was dramatically increased when the heating rate was increased to 5 °C/min and decreased at the heating rate of 10 °C/min.

The reason of such a behavior is believed as the presence of molten lithium compounds. The thermal characteristic of the Li_2CO_3 is a well-known behavior. It was firstly melted and the thermal decomposition into Li_2O was taken place from its liquid phase. At lower heating rates of 2 and 5 °C/min where Li_2CO_3 melts, it causes segregation resulted with Li_2ZrO_3 and as a consequence $LaAlO_3$. Since the total heat treatment time of 5 °C/min is nearly half of the 2°C/min, the diffusion is insufficient to form a LLZO resulting with an increase on Li_2ZrO_3 and $LaAlO_3$. When the heating rate was increased to the 10 °C/min, the segregation because of the Li_2CO_3 melting was strongly prohibited. Decomposition was taken place from its solid state. Such an enhanced homogenization, the obtained crystal structure was nearly purely LLZO.

To conclude the findings above, presence of impurity and cubic phase stabilization is two rivalry phenomena which act at the same time. To obtain a cubic LLZO phase, the total heat treatment time should be increased since the cubic phase transformation's reconstructive nature. On the other hand, in order to minimize the amount of impurity phases, the total heat treatment time should be lowered as low as possible. Since additional step is required for the cubic phase transformation, the purity of the obtained powders were more important and higher purity, but pure tetragonal, 10 °C/min heating rate was favored and selected for the further experiments.

3. A THERMODYNAMIC POINT OF VIEW FOR SELECTING PRECURSORS FOR SOLID STATE $Li_7La_3Zr_2O_{12}$ SYNTHESIS

For the solid-state reaction synthesis of Al containing $Li_7La_3Zr_2O_{12}$, various precursors have been used. Since there is a lack of general agreement for choosing precursors, a quantitative approach to build a consensus is required. In this chapter, a thermodynamic point of view for selecting the precursors in the field of $Li_7La_3Zr_2O_{12}$ synthesis was covered according to the Gibbs Energy and Enthalpy change of precursors' decomposition reactions. Within the scope of the chapter, $Al(OH)_3$, was discussed for the first time as an Al source in the field of solid-state LLZO synthesis.

3.1. Motivation

Solid electrolytes for all solid-state lithium batteries show unique advantages over organic based liquid electrolytes such as excellent battery lifetime, electrochemical and thermal stability and enhanced safety [39-41]. Thus, they gained a lot of interest especially for the safety-concerning applications such as electrical vehicles (EVs).

Nowadays, garnet-type solid electrolytes became popular because of their outstanding ionic conductivities among other types of solid electrolytes. Cubic $Li_7La_3Zr_2O_{12}$ (LLZO) phase, as one of the garnet-type solid electrolyte, was successfully used in the lab-scale all solid-state lithium batteries [42].

There are lots of studies on the LLZO synthesis via solid-state reaction method. In these studies, various types of powders were used (Table 3.1).

Table 3.1. *A brief overview of Li, La, Zr and Al sources used in the synthesis of LLZO through solid-state reaction related methods*

Research Group	Li Source	La Source	Zr Source	Al Source	Calcination Conditions	Sintering Conditions	Ref
Murugan et. al.	LiOH	La_2O_3	ZrO_2	-	900 & 1100°C – 12h	1200°C - 16h (C, NI)	[43]
Ahn et. al.	LiOH	La_2O_3	ZrO_2	-	900°C – 12h	1220°C – 18h (T, C)	[44]
Awaka et. al.	Li_2CO_3	La_2O_3	ZrO_2	-	900°C – 12h	980°C – 5h (T, n.d.)	[24]
Chen et. al.	Li_2CO_3	La_2O_3	ZrO_2	Al_2O_3	n.d.	n.d.	[45]
Dermenci et. al.	Li_2CO_3	La_2O_3	ZrO_2	Al_2O_3	900°C & 980°C – 12h (T)	1150°C – 24h (C, NI)	[46]
Chen et. al.	Li_2CO_3	$La(OH)_3$	ZrO_2	Al_2O_3	900°C & 950°C – 10h (n.d.)	1200°C – 24h (C, I)	[47]
Düvel et. al.	Li_2O	La_2O_3	ZrO_2	Al_2O_3	600°C – 6h (I)	1227°C – 15h (C, I)	[48]
Hitz et. al.	$LiNO_3$	La_2O_3	ZrO_2	-	700°C – 12h (T, I)	1100°C – 12h (T, I)	[49]

n.d.= No data, T=Tetragonal, C= Cubic, I=Impurity phases present, NI=No impurity phases present

According to Table 3.1, there is a consensus on ZrO_2 as a Zr source and Al_2O_3 as an Al source but other metal sources vary and result in different synthesis conditions. The common Li sources are LiOH and Li_2CO_3; La sources are La_2O_3 and $La(OH)_3$.

In the light of all these findings, each precursor has unique thermodynamical nature and considering this, there is a lack of theoretical background on selecting different precursors for the synthesis of LLZO powder.

This chapter aims to discuss the selection of Li, La and Al precursors for the solid state LLZO synthesis with the help of Gibbs Free Energy and Enthalpy calculations. Cubic phase stabilization, microstructural changes and electrochemical performance at various sintering temperatures between 1000 and 1200°C by using favored precursors was also reported.

3.2. Experimental

All thermodynamic data were calculated between 0°C to 1000°C (maximum calcination temperature was selected such that all decomposition reactions were expected to be completed at that temperature) with a step size of 100 °C by using a thermodynamic software (HSC-Chemistry Software (Outokumpu)) and presented on 1 mole Li_2O, La_2O_3 and Al_2O_3 formation basis under 1 atm air pressure. By using optimized data from HSC; LLZO was synthesized by solid-state reaction method. 30 mole % Al was added to stabilize cubic phase. In order to evaluate the performance, stoichiometric amounts of thermodynamically favored powders along with ZrO_2, were mixed in agate mortar grinder (Retsch RM200) for 1 hour. The excess Li to compensate Li losses during calcination and sintering was selected as 15 mole %. Powders were calcined at 1000°C which was established to be the highest calcination temperature to prevent excessive Li losses for 6 hours and then, sintered at 1000, 1100 and 1200°C which was lower than the minimum temperature required for cubic phase stabilization without Al stabilizer addition for 12 hours within its powder bed. After calcination, powders were ground again for 1 hour and 1.5 g of calcined powders were isostatically pressed to obtained pellets (15 mm diameter) at 240 MPa for 45 minutes. 10 °C/min heating rate was set for calcination and sintering studies.

Crystal structures of pellets were determined by using X-ray diffractometer (XRD - Rigaku MiniFlex 600) between 2θ=15° - 55° with a scan speed of 1 °/min and step size of 0.02° by using Cu K_α X-ray source.

Unpolarized micro-Raman spectra were collected by using Witec Alpha300R with 532 nm laser with 1200 gr/mm grating and 50X magnification.

For microstructural evaluation, scanning electron microscope (SEM-Zeiss SUPRA 50VP) attached with an energy dispersive spectrometer EDS (Oxford INCA) was used on the fractured surface of each pellet. Pellets were sputtered with Au-Pd for 15 seconds prior to SEM investigations.

Bulk conductivities were measured with an AC Impedance Method with 30 mV Perturbation Amplitude between 1 kHz to 1 MHz Frequency range by using Galvanostat/Potentiostat system (Gamry Reference 600). Pellets were firstly polished down to 1200 grit abrasive SiC papers. Then, Au-Pd as Li-ion blocking electrode was sputtered on both sides of pellets for 90 seconds. The average of at least 3 measurements was taken for measuring the thickness and the diameter. Selected pellets were heated up to 114 °C in a tubular furnace designated for that purpose and activation energy (E_a) was calculated using the equation:

$$\sigma T = \sigma_0 \times e^{\frac{-E_a}{k_B T}} \tag{3.1}$$

where σ, k and T showed conductivity, Boltzmann constant and temperature, respectively.

3.3. Results & Discussion

3.3.1. Thermodynamic Calculations

Table 3.2 showed the calculated Gibbs Free Energy and Enthalpy changes of LiOH, Li_2CO_3, $LiNO_3$, $La(OH)_3$ and $Al(OH)_3$ as a function of temperature for their oxide formation reactions given below:

$$2LiOH_{(s)} \rightarrow Li_2O_{(s)} + H_2O_{(g)} \tag{3.2}$$

$$Li_2CO_{3(s)} \rightarrow Li_2O_{(s)} + CO_{2(g)} \tag{3.3}$$

$$LiNO_{3(s)} \rightarrow Li_2O_{(s)} + 2NO_{2(g)} + \frac{1}{2}O_{2(g)} \tag{3.4}$$

$$2La(OH)_{3(s)} \rightarrow La_2O_{3(s)} + 3H_2O_{(g)} \tag{3.5}$$

$$2Al(OH)_{3(s)} \rightarrow Al_2O_{3(s)} + 3H_2O_{(g)} \tag{3.6}$$

According to the Table 3.2, the change in Gibbs Free Energy at 1000 °C calcination temperature for the thermal decompositions of LiOH, Li_2CO_3 and $LiNO_3$ were all positive and extra energy must be supplied to the system in order to form Li_2O.

Table 3.2. *Gibbs Free Energy and Enthalpy change calculations for oxide formation reactions of LiOH, Li_2CO_3, $LiNO_3$, $La(OH)_3$ and $Al(OH)_3$*

Temperature	*Gibbs Free Energy Change (kJ/mole)*					*Enthalpy Change (kJ/mole)*				
(°C)	*LiOH*	*Li_2CO_3*	*$LiNO_3$*	*$La(OH)_3$*	*$Al(OH)_3$*	*LiOH*	*Li_2CO_3*	*$LiNO_3$*	*$La(OH)_3$*	*$Al(OH)_3$*
0	96.8	180.6	323.3	178.1	21.3	135.5	224.8	436.8	303.8	151.2
100	82.8	164.5	282.3	132.5	-26.1	134.4	224.3	433.2	300.7	149.8
200	69.2	148.6	242.4	88.0	-73.0	132.5	223.5	428.5	295.5	146.0
300	56.1	133.0	208.2	44.8	-118.8	130.0	221.6	369.5	288.4	139.5
400	43.5	117.8	181.0	3.1	-163.1	127.1	217.8	358.1	279.2	129.8
500	32.8	103.4	155.5	-37.2	-205.7	81.5	213.5	347.5	268.2	116.5
600	26.8	89.3	131.2	-75.9	-246.4	76.1	210.5	337.7	255.2	99.7
700	21.4	75.6	108.1	-113.0	-284.9	71.2	206.3	328.6	240.3	79.2
800	16.5	66.0	85.9	-148.5	-321.2	66.9	157.3	320.2	223.5	55.2
900	12	57.7	64.4	-182.3	-355.0	63.2	153.8	312.5	204.8	27.6
1000	7.8	49.6	43.5	-214.5	-386.3	60.2	150.9	305.4	184.2	-3.7

In contrast, energy was generated in the system during thermal decompositions of $La(OH)_3$ and $Al(OH)_3$ since the change on Gibbs Free Energy at 1000 °C calcination temperature were negative.

Since much less energy (7.8 kJ/mole) required, LiOH was the favored Lithium precursor compared to Li_2CO_3 and $LiNO_3$. $La(OH)_3$ and $Al(OH)_3$ were other preferred precursors with their endergonic nature of thermal decomposition reactions.

At 1000 °C calcination temperature, Enthalpy changes pointed out that the thermal decompositions of LiOH, Li_2CO_3, $LiNO_3$ and $La(OH)_3$ were all endothermic and additional heat was needed for decomposition reactions given in Equations between (3.2) and (3.6). Among Lithium sources, LiOH is the most favorable due to its lowest enthalpy change. Moreover, with its -3.7 kJ/mole Enthalpy change, thermal decomposition of $Al(OH)_3$ was exothermic and release extra heat to the system. La_2O_3 should also be preferred rather than $La(OH)_3$ because of the $La(OH)_3$'s endothermic nature at the calcination temperature of 1000 °C.

An attention should be paid to $Al(OH)_3$. In a thermodynamic point of view, $Al(OH)_3$ was one step ahead compared to the common Aluminum source, Al_2O_3, with its exergonic and exothermic behavior at 1000 °C calcination temperature.

To sum up the theoretical findings, LiOH, $La(OH)_3$ and $Al(OH)_3$ were thermodynamically favored precursors in terms of Gibbs Free Energy change of their

oxide formation reactions. On the other hand, LiOH, La_2O_3 and $Al(OH)_3$ were determined as the most favored precursors according to Enthalpy change calculations.

Before solid-state LLZO synthesis, precursor powders were generally dried prior to use [24, 38, 43, 44, 46, 50]. In this manner, it's also important to enlighten the hygroscopic behavior of the thermodynamically preferred precursor powders. Room temperature Gibbs Free Energy change of hydration reactions given below could enable us to discuss the hygroscopic behavior of La_2O_3 and Al_2O_3:

$$La_2O_{3(s)} + 3H_2O_{(g)} \rightarrow 2La(OH)_{3(s)} \qquad \Delta G_{25}= \text{-166.6 kJ /mole} \qquad (3.7)$$

$$Al_2O_{3(s)} + 3H_2O_{(g)} \rightarrow 2Al(OH)_{3(s)} \qquad \Delta G_{25}= \text{-21.3 kJ /mole} \qquad (3.8)$$

As stated in Equation (3.7) and (3.8), both La_2O_3 and Al_2O_3 were eager to absorb water with their -166.6 and -21.3 kJ/mole Gibbs Free Energy change at 25 °C, respectively. In other words, $La(OH)_3$ and $Al(OH)_3$ stood forward with their excellent room temperature stability in the presence of humidity. It's worth to note that LiOH was excluded from the calculations since it was the hydrated form of Li_2O.

3.3.2. Characterization of $Li_7La_3Zr_2O_{12}$ by using thermodynamically favored precursors

Two batches were prepared by using appropriate amounts of LiOH, $La(OH)_3$, ZrO_2 and $Al(OH)_3$ (batch denoted as ΔG-mix) and LiOH, La_2O_3, ZrO_2 and $Al(OH)_3$ (batch denoted as ΔH-mix). From now on, the notation "ΔG-mix" will be used to identify the mixtures prepared by the favored precursors according to Gibbs Free Energy change and "ΔH-mix" will be used to identify the mixtures prepared by the favored precursors according to Enthalpy change. Thermal behavior of ΔG-mix and ΔH-mix were assessed by the TGA/DTA plots given in Figure 3.1.

There were stepwise weight losses for both batches until 1000 °C. The endothermic peak and weight loss located below 100 °C was the evaporation of physically bonded water. Another group of endothermic peaks at 323 and 428 °C were very strong in ΔH-mix.

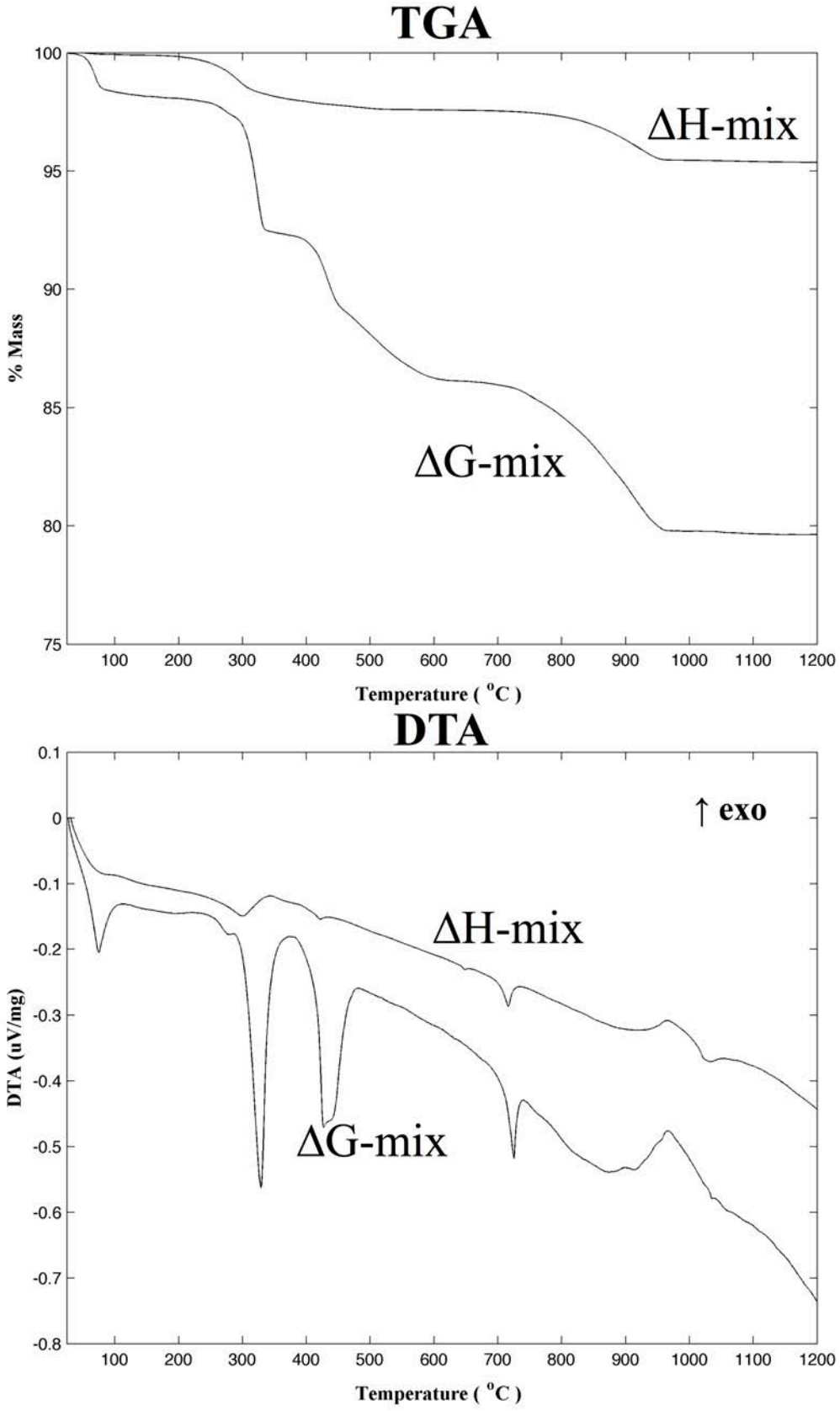

Figure 3.1. *TG/DTA plots of powder mixtures prepared based on Gibbs Free Energy and Enthalpy change calculations*

Weight losses were attributed to the two-step decomposition of $La(OH)_3$ into La_2O_3 [46]. The sharp endothermic peak at 725 °C and subsequent weight losses were the melting and thermal decomposition of Li_2CO_3 impurity which was inevitably present with LiOH precursor, respectively. It should also be emphasized that there was a minute amount of $La(OH)_3$ decomposition peaks in ΔH-mix even if La_2O_3 was the Lanthanum precursor. Either H_2O absorption on La_2O_3 during heat treatment or instability of La_2O_3 during mixing in 2-propanol media were believed as the main reasons of $La(OH)_3$ existence.

For solid-state reaction synthesis of LLZO, the precursor powders were generally mixed in 2-propanol in order to obtain homogeneous mixture. Thus, the effect of the mixing media was determined by mixing ΔH-mix precursors with (denoted as Wet-mix) and without (denoted as Dry-mix) 2-propanol addition. Their XRD patterns were shown in Figure 3.2.

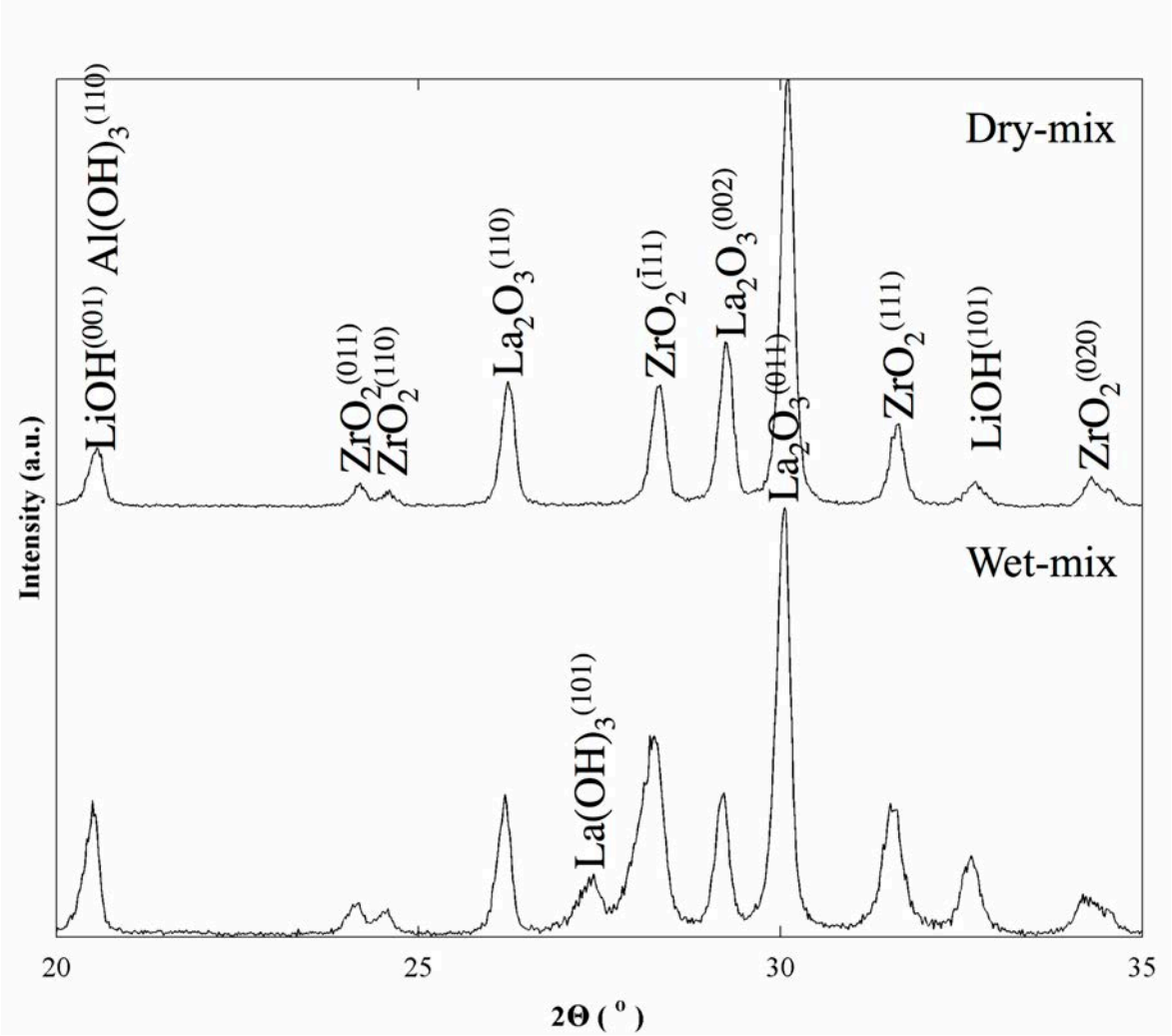

Figure 3.2. XRD *patterns of wet and dry mixed precursors for solid-state LLZO synthesis*

Peaks in dry mixed precursors were indexed as LiOH (PDF No: 01-076-0911), La_2O_3 (PDF No: 01-071-5408), ZrO_2 (PDF No: 01-074-1200) and $Al(OH)_3$ (PDF No: 00-033-0018). However, additional $La(OH)_3$ peak (PDF No: 00-006-0585) was formed during mixing in 2-propanol media. The reason may be attributed either to the water content of 2-propanol or unwanted reaction of the hydroxyl group in 2-propanol with La_2O_3. Other precursors were seemed to be stable in 2-propanol media. One can conclude from the findings that wet mixing with 2-propanol should be avoided when La_2O_3 was used and dry mixing could be a better option.

In order to determine the role of thermodynamically favored precursor powders on performance, ΔG-mix and ΔH-mix powders were initially dry-mixed, calcined at 1000°C for 6 hours, sintered at specified temperatures between 1000°C – 1200°C for 12 hours. Their XRD patterns were given in Figure 3.3.

In both mixtures, patterns after calcination were identical pointing out the tetragonal LLZO phase (PDF Card No: 01-080-6141). However, XRD patterns after sintering at 1000, 1100 and 1200 °C were indexed as cubic LLZO phase (PDF Card No: 01-078-6708).

A particular emphasis should be made for the pellets sintered at 1000 and 1100°C in both ΔG-mix and ΔH-mix. The background formed between $2\theta = 50° – 55°$ was believed to be due to the presence of both cubic and tetragonal phases having a small particle size at the same time. However, after sintering at 1200°C, the background corresponding to tetragonal phase diminished implying that no residual tetragonal LLZO phase left. Moreover, the gradually increasing peak intensity at $2\theta = 34.5°$ was obvious. Such an increase in peak intensity was the clue of the peak overlapping with Li_2O (PDF Card No: 01-076-9237).

Unpolarized micro-Raman spectrum in Figure 3.4 also confirmed the presence of tetragonal LLZO phase for the pellets sintered from ΔG-mix at 1000 and 1100°C and Li exclusion mechanism.

The acquired spectrum was in accordance with LLZO spectrum reported elsewhere [38]. The bands between 100 and 150 cm^{-1} were the vibrations of La cations where the wide band at about 640 cm^{-1} was due to Zr-O bond stretching. It has been recently reported that the Raman shift at 157 cm^{-1} was the characteristic peak of the tetragonal LLZO phase and the shift at 289 cm^{-1} was continually decreased and disappeared when cubic LLZO phase was stabilized [51, 52].

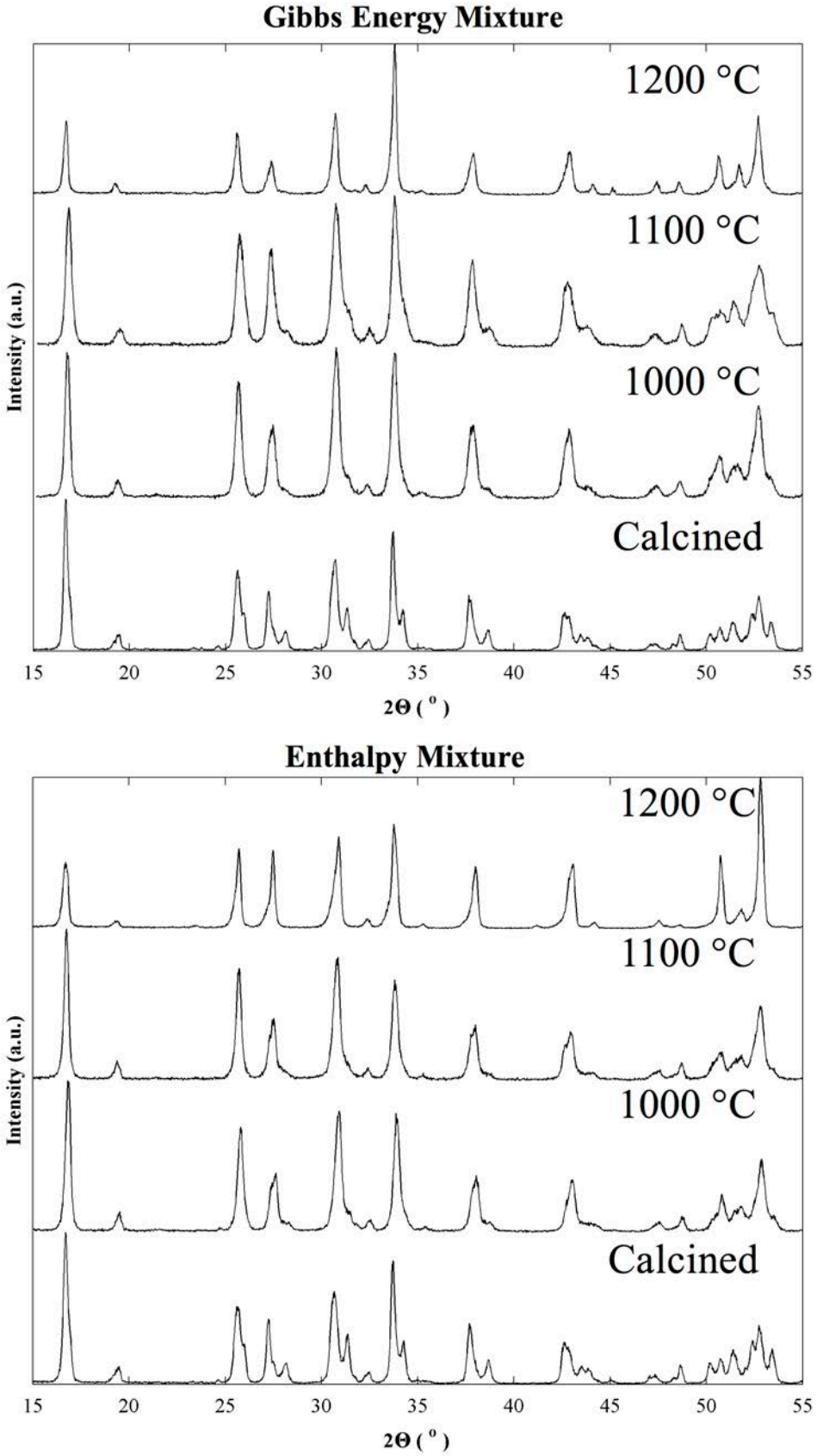

Figure 3.3. *XRD patterns of powders after calcination and pellets sintered at 1000°C, 1100°C and 1200°C*

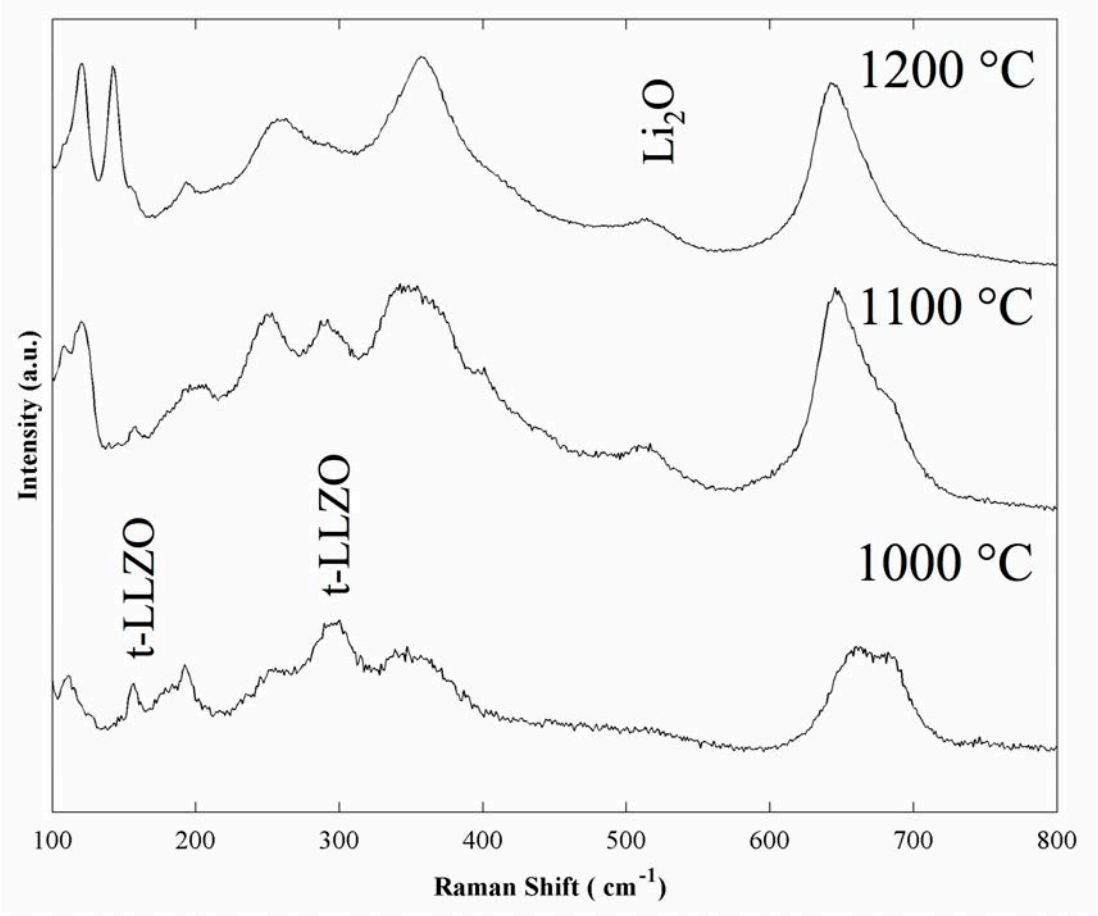

Figure 3.4. *Unpolarized micro-Raman spectrum of LLZO sintered at 1000 °C to 1200 °C for 12 hours*

The band at around 520 cm^{-1} was T_{2g} mode of Li_2O and appeared first in the sample sintered at 1100°C [53].

The presence of Li_2O in Figure 3.3 and Figure 3.4 was believed to be due to the well-documented Li exclusion phenomenon during Al incorporation in cubic LLZO structure based on the reaction given below [54]:

$$Li_{Li}^{x} + \frac{1}{2}Al_2O_3 \rightarrow Al_{Li}^{\cdot\cdot} + 2V_{Li}^{\prime} + \frac{3}{2}Li_2O \tag{3.9}$$

Considering the discussions in our previous paper, cubic LLZO structure could host more Al within the structure in comparison to tetragonal structure [46]. Accordingly, Li_2O could be formed when cubic LLZO phase appeared as a consequence of the Li exclusion phenomenon.

It’s worth to say that unpolarized micro-Raman results were strongly consistent with the XRD results showing the presence of Li_2O phase, tetragonal and cubic LLZO phase existence at specified sintering temperatures.

Secondary electron SEM images from fractured surfaces (Figure 3.5) also showed the microstructural changes for different sintering temperatures as well as different mixtures.

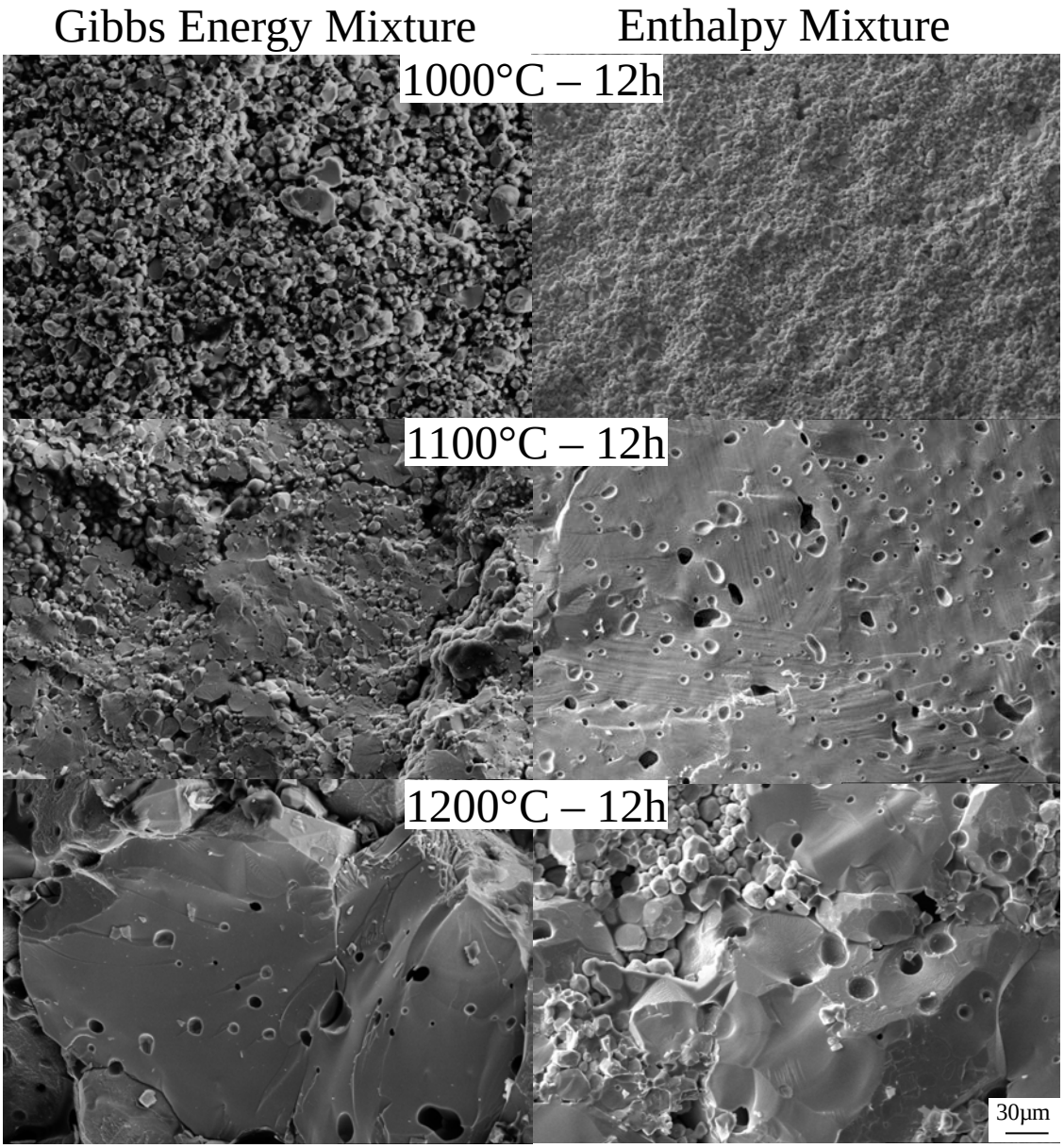

Figure 3.5. *Secondary electron images taken from the fractured surface of the samples sintered from Gibbs Free Energy and Enthalpy change mixture at 1000 °C (a), 1100 °C (b) and 1200 °C (c) for 12 hours*

It can be referred from the fractured surface images that after sintering at 1000 °C, almost homogeneously distributed and interconnected pores were present with a lack of densification in both mixtures. The initial stage of sintering could be observed. However, grains were smaller and interconnected pores were hardly seen in ΔH-mix as compared to ΔG-mix.

In the 1100 °C – 12 hours sintering conditions, grains were dramatically getting bigger revealing that grain growth was the dominant phenomenon. Porosities within grains were first observed. Although ΔG-mix has some small grains in the triple junctions of large grains, such small grains were uncommon in ΔH-mix.

In the fractured surface images associated with 1200 °C – 12 hours sintering conditions, an excessive grain growth forming hundreds of micrometer-sized grains could be observed. The size of porosities within grains was also increased. Apart from ΔG-mix, relatively small grains were formed at the triple junctions of the grains in ΔH-mix. Both intergranular and transgranular fracture were observed for all sintering conditions.

Electrochemical Impedance Spectroscopy (EIS) measurements were applied for the purpose of conductivity discussions on cubic stabilized LLZO samples from ΔG-mix and ΔH-mix. In Figure 3.6, the Nyquist plot and the equivalent circuit (inlet) of the samples sintered at 1200 °C for 12 hours were demonstrated for each mixture.

In a typical Nyquist plot of solid ion conductors, there were consecutive two semicircles at the high-frequency region that was ascribed as ionic and grain boundary resistance and also linear-like tails at low-frequency region because of the Li-ion blocking electrodes. In contrast, the behavior at the high-frequency region for ΔG-mix and ΔH-mix in Figure 3.6 was not the same. There was only one semicircle became apparent in ΔH-mix which corresponds to ionic resistance coming together a negligible amount of grain boundary resistance. Meanwhile, a flat curve as a consequence of nearly equal ionic and grain boundary resistance contribution was observed in the ΔG-mix. Considering the fractured surface images and Nyquist plot, it could be concluded that grain boundary resistance was decreased in ΔH-mix thanks to the increased number of grain boundaries. Grain boundaries were highly concentrated defect regions, which greatly enhance ionic conductivity. In this regard, the large number of grain boundaries will reduce grain boundary resistance.

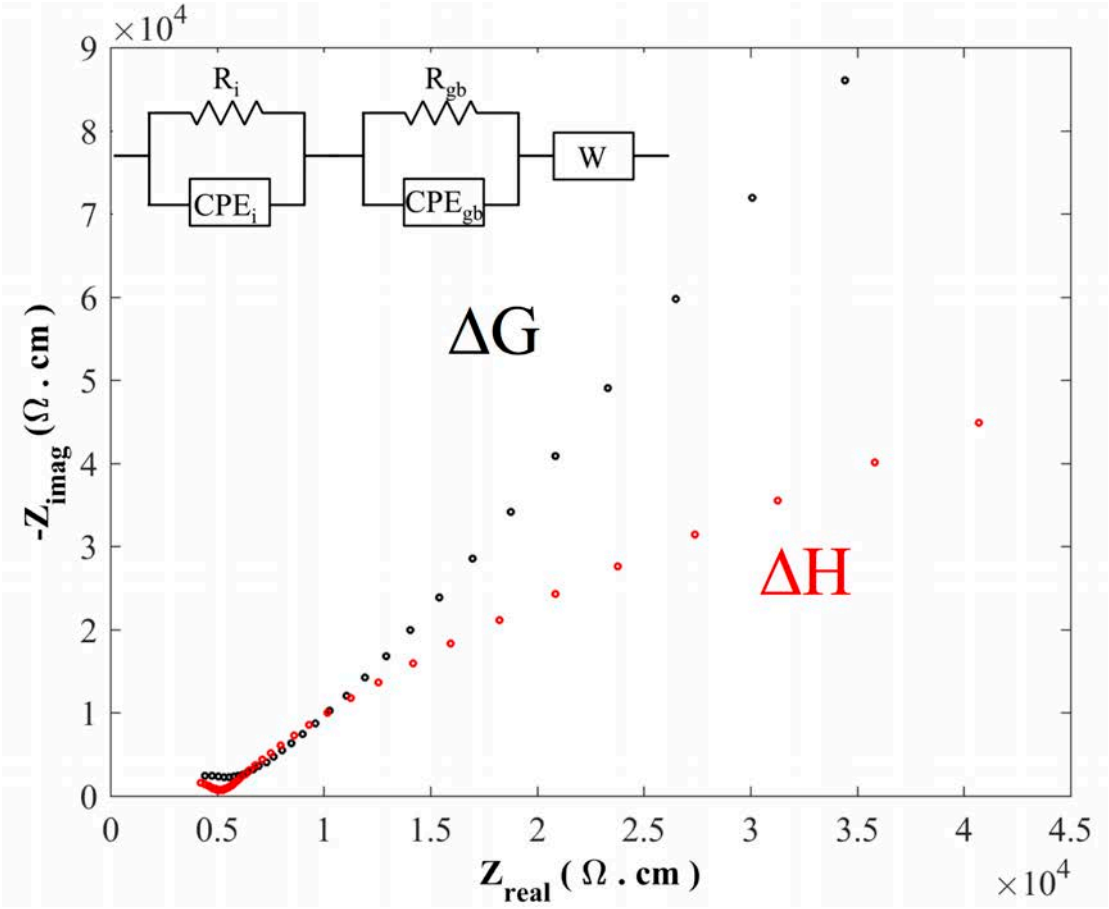

Figure 3.6. *Nyquist Plots of LLZO samples sintered at 1200 °C for 12 hours*

The fitted bulk conductivities measured from the Nyquist plots in Figure 3.6 was calculated as 1.37 x 10^{-4} S/cm for ΔG-mix and 2.11 x 10^{-4} S/cm for ΔH-mix that was one of the highest among other studies [24, 43-45, 47-49, 55]. In the light of the findings in Figure 3.5 and Figure 3.6, the probable explanation on the conductivity changes was the grain coarsening if hydroxides were used.

Table 3.3 summarized the bulk conductivities of each pellet sintered at temperatures between 1000 and 1200 °C.

Table 3.3. *Bulk conductivities of pellets sintered with Gibbs Free Energy mixture (σ_{dG}) and Enthalpy mixture (σ_{dH}) between 1000 and 1200 °C*

Sintering Conditions	*σ_{dG} (mS/cm)*	*σ_{dH} (mS/cm)*
1000°C - 12h	0.002	0.003
1100°C - 12h	0.019	0.072
1200°C - 12h	0.137	0.211

The dramatic drop in bulk conductivity for the samples sintered at 1000 and 1100 °C compared to 1200 °C was due to the presence of tetragonal LLZO. Moreover, the bulk conductivity of ΔH-mix was always higher than ΔG-mix.

Within the scope of the chapter, $Al(OH)_3$ has been discussed. However, it's worth to compare the performance of widely-used Al_2O_3 and $Al(OH)_3$. Concerning the effect of Aluminum source on ionic conductivity, a control experiment which contains Al_2O_3 as Aluminum constituent was conducted by adapting the conditions obtained at the highest conductivity (ΔH-mix; sintered at 1200 °C – 12 hours sintering conditions) and its bulk conductivity was calculated as 2.80×10^{-4} S/cm which was higher than those obtained by using $Al(OH)_3$. The similar increment on ionic conductivity was observed while changing Lanthanum source from $La(OH)_3$ to La_2O_3 in Figure 3.6.

Activation energy can give an idea about the ease of Li-ion hopping between two different sites within the lattice and can be calculated by measuring the slope of the Arrhenius type relation between temperature and conductivity. The lower activation energy means the easier Li-ion transport within the lattice. Since it's a well-known fact that tetragonal LLZO has relatively low ionic conductivity compared to the cubic LLZO phase and not considered as an option in the field of solid electrolyte, the activation energy calculations were conducted for the samples sintered at 1200 °C for 12 hours which was shown to be in a cubic phase (Figure 3.3 and Figure 3.4). Arrhenius type plot for ΔG-mix and ΔH-mix was shown in Figure 3.7.

From the slope of the fitted data in Figure 3.7, the activation energies for the samples sintered by using both ΔG-mix and ΔH-mix were calculated as 0.47 and 0.23 eV, respectively pointing out much easier Li-ion transport by using ΔH-mix. As compared to literature values, ΔH-mix could also be classified as one of the lowest reported values with its 0.23 eV activation energy [24, 45, 48, 49, 56].

An important technologic outcome of the present chapter is the reduced processing time. Cubic LLZO phase is obtained at 1200°C sintering for 12 hours after 1000°C calcination for 6 hours which is one of the shortest total processing time.

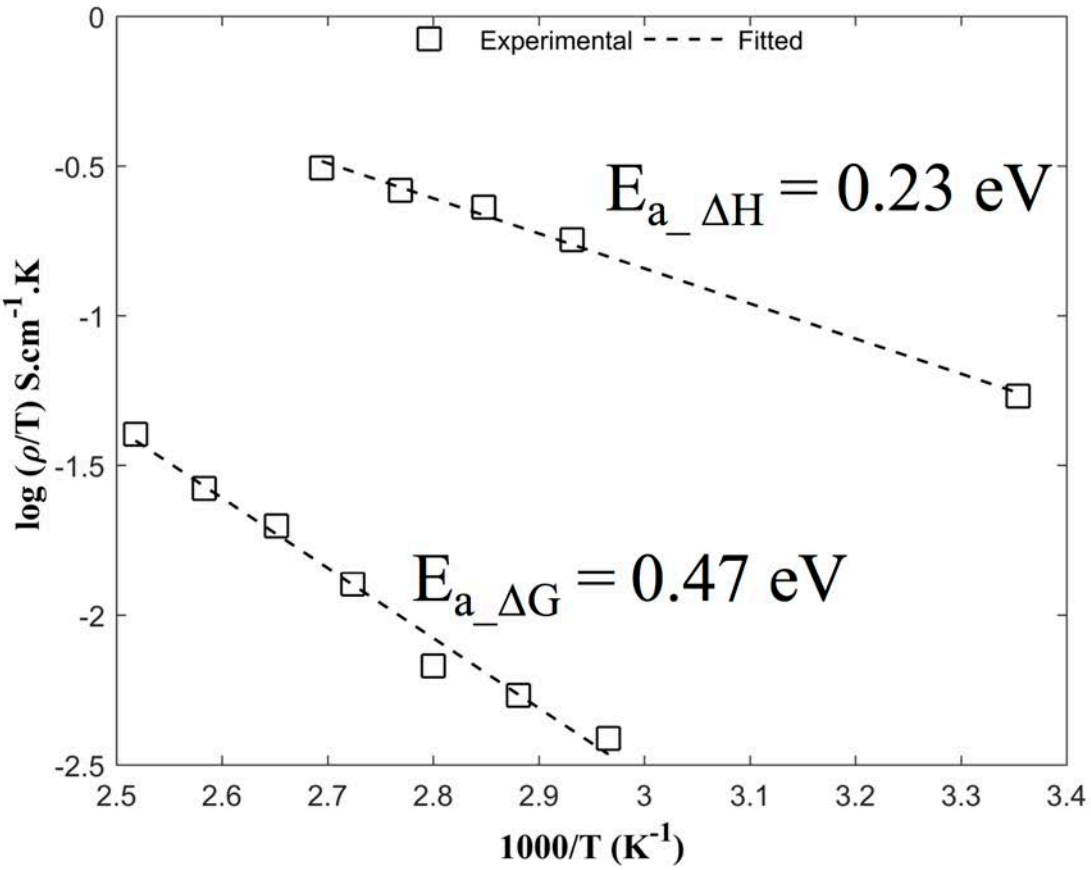

Figure 3.7. *Arrhenius plot of LLZO sintered at 1200 °C for 12 hours*

3.4. Conclusion

Thermodynamic calculations have been conducted in order to determine the ideal precursors for Al stabilized LLZO synthesis. According to the calculations, La_2O_3 and $La(OH)_3$ is the preferred precursors in terms of Gibbs Free Energy and Enthalpy change, respectively. LiOH and $Al(OH)_3$ are commonly favored for both calculations.

$La(OH)_3$ and $Al(OH)_3$ show good hygroscopic behavior when compared to their oxides. However, using hydroxides result in excessive grain growth and causing a lower bulk conductivity.

Higher bulk conductivity (2.11 x 10^{-4} S/cm) and activation energy (0.23 eV) was obtained from ΔH-mix with a negligible amount of grain boundary resistance. However, in the case of ΔG-mix, the bulk conductivity is only around 1.37 x 10^{-4} S/cm and 0.47 eV activation energy because of the significant grain boundary resistance contribution.

4. A NOVEL DENSIFICATION MODEL FOR $Li_7La_3Zr_2O_{12}$

Microstructures of inorganic solid ionic conductors should be as dense as possible since porosities have no contribution to the ionic conductivity. Besides, the number of grain boundaries should be the highest for improved Li^+ conduction. For densification assessments during sintering of $Li_7La_3Zr_2O_{12}$, one of the popular solid ion conductors in the field of all-solid-state Li-ion batteries, Archimedes density measurement technique has been widely used. However, Archimedes density is unable to take into account closed porosities that are very common in $Li_7La_3Zr_2O_{12}$ microstructures. In this chapter, a densification model for $Li_7La_3Zr_2O_{12}$ is introduced with the help of dilatometer, Archimedes density and radial shrinkage.

4.1. Motivation

Inorganic solid ion conductors are considered as one of the crucial member for safety concerns in Li-ion batteries. Among them, garnet type $Li_7La_3Zr_2O_{12}$ (LLZO) stands forward as an important solid ion conductor with their outstanding performance on safety, stability and ionic conductivity. However, there's still a gap to reach the commercially expected conductivity values [12]. Various approaches such as cation doping and battery designations were tried in order to fulfill the commercial requirements [57-59]. But, sintering and densification behavior of LLZO have not been studied much in detail.

The typical microstructure of LLZO contains a significant number of closed porosities [46]. Even though, Archimedes Method is the unique technique used for density evaluation in the field of LLZO synthesis, it's insufficient in the presence of closed porosities since they were unable to be wetted during immersion into the liquid [60]. The use of relative density for the purpose of indicating closed porosity changes is questionable for two main reasons that directly affects the theoretical density calculations: (1) Dopant incorporation within garnet LLZO structure and atomic replacements changes the theoretical density and calculations are an experimentally challenge; (2) The actual composition of Lithium in the garnet LLZO structure could vary due to high temperature Lithium losses and changes the theoretical density.

Thus, Archimedes density measurements itself would not be enough for the assessment of densification. In some cases, volumetric shrinkage, along with Archimedes density, was used as an option [61]. However, for volumetric shrinkage

measurements, volume calculations should be as precise as possible. On the other hand, in powder bed synthesis methods (a typical LLZO synthesis method), powders from powder bed can be chemically bonded to the pellet surface, therefore extensive polishing is required during sample preparation. Even after this, accuracy of polishing may affect the repeatability of the real volume calculations.

Radial shrinkage has not been used in the field of LLZO synthesis and believed that would increase the reliability in comparison to volumetric calculations. For better assessment of densification behavior of LLZO, a combination of both Archimedes (True) density and radial shrinkage measurements should be considered.

This work aims to reveal the role of radial shrinkage on LLZO densification. By combining Archimedes density, optical dilatometer measurements, radial shrinkage and fractured surface images, a densification model as a function of temperature was also introduced within the present study.

4.2. Experimental

To synthesize LLZO powders, stoichiometric amounts of LiOH (Alfa Aesar), La_2O_3 (Roth), ZrO_2 (Inframat) and $Al(OH)_3$ (Merck) powders were mixed in agate mortar grinder (Retsch RM200). 15 % of excess Li as LiOH was added to compensate Li losses. As-mixed powders were calcined at 1000°C, reground and isostatically pressed into 15 mm diameter pellet at 290 MPa. Then, pellets were sintered at 1000, 1100 and 1200°C. 10 °C/min heating rate was set for all heat treatments. For microstructural evaluation of fractured surfaces of each pellet, scanning electron microscope (SEM-Zeiss SUPRA 50VP) was used on. Shrinkage profile was acquired from optical dilatometer (Expert System Solutions, Misura HSM, Italy) until 1200°C under air atmosphere with a heating rate of 10 °C/min. Density measurements were determined by Archimedes method in 2-propanol media according to the equation given below:

$$\rho_A = \frac{m_{dry}}{m_{sat} - m_{im}} \times \rho_{propanol} \quad (4.1)$$

where m_{dry}, m_{sat} and m_{im} are dry, saturated and immersed weights, respectively. Pellets were immersed into boiled 2-propanol for 3 hours. Then, immersed weights were

gathered. After that pellets were thoroughly wiped with a laboratory wipes and saturated weight were measured. The density of 2-propanol used in the calculations was 0.786 g/cm^3.

Radial shrinkage (R.S.) is calculated by obeying the following equation:

$$RS\% = \frac{D_{b.s.} - D_{a.s.}}{D_{b.s.}} \times 100 \qquad (4.2)$$

where $D_{b.s.}$ and $D_{a.s.}$ refer to diameters before and after sintering, respectively. Three values were measured and their average was determined as $D_{a.s.}$. The measurement errors in radial shrinkage calculations were measured to be less than below 2 % for each sample.

4.3. Results & Discussion

Dilatometer measurement was conducted for determining the temperature where sintering starts in terms of shrinkage of $Li_7La_3Zr_2O_{12}$ as a function of temperature. The curve was presented in Figure 4.1.

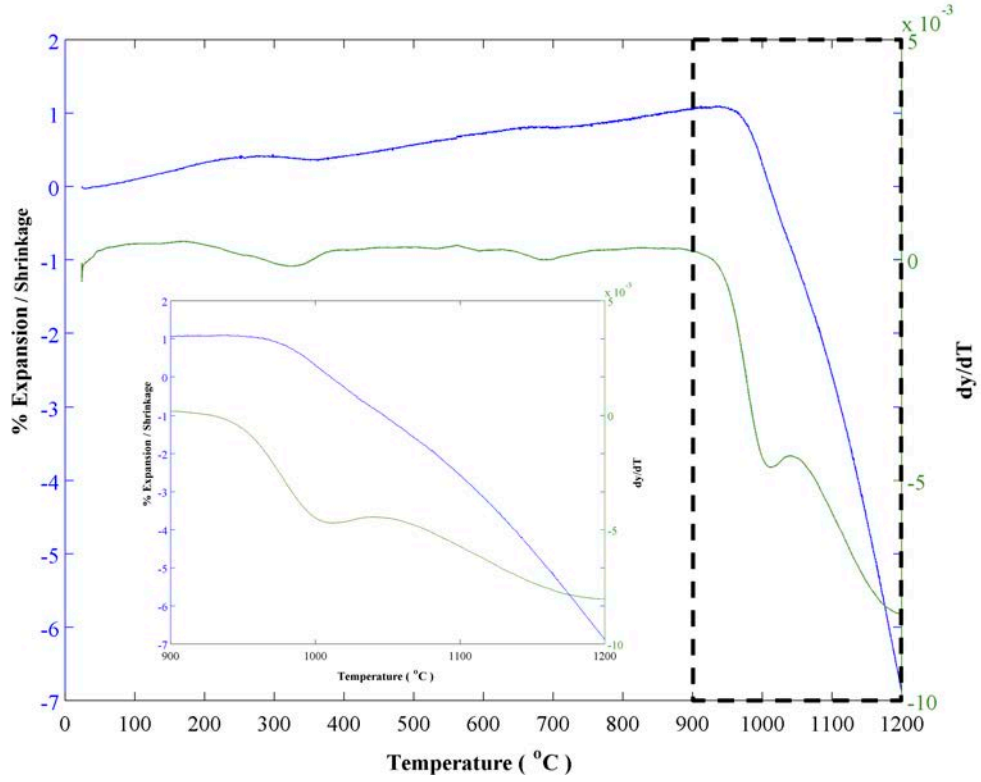

Figure 4.1. *Thermal expansion behavior of LLZO*

The dilatometer curve in Figure 4.1 showed a slight expansion until 980°C that could be attributed to H_2O and CO_2 capture and the thermal expansion of the pellet. After that, an excessive shrinkage was observed up to 1200°C resulting with 6.9 % total shrinkage. The zero shrinkage temperature for LLZO was found as 1000°C.

The dy/dT profile in Figure 4.1 showed changes on shrinkage rate. The slope of the dy/dT profile until 1020 °C was high. However, starting from 1050°C, the curve continued with a reduced slope. When the temperature was reached to 1200°C, nearly flat profile was obtained. It can be inferred from the optical dilatometer curve in Figure 4.1 that excessive densification starts with a high shrinkage rate. Later on, a second stage of sintering starts with a reduced shrinkage rate and at 1200°C, a new stage began with stable shrinkage rate.

In the light of the findings related to shrinkage rate, pellets were sintered at 1000, 1100 and 1200 °C that represented three different profile of shrinkage rate and their Archimedes density and radial shrinkage profiles were plotted as a function of sintering temperature in Figure 4.2.

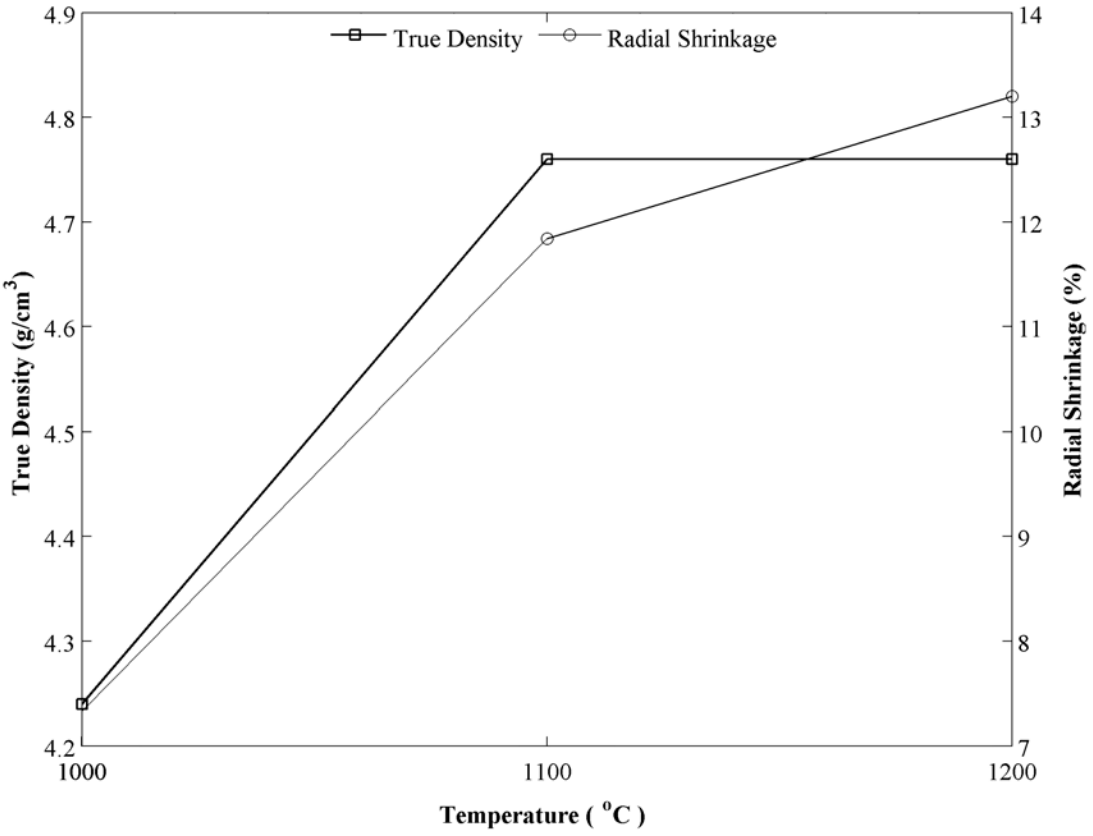

Figure 4.2. *Archimedes densities and radial shrinkage percentages of LLZO sintered at 1000, 1100 and 1200 °C*

In case of the increasing sintering temperature to 1100°C, Archimedes density was increased dramatically from 4.24 to 4.76 g/cm^3. Radial shrinkage was also raised from 7.3 % up to 11.8 %. At the point where Archimedes densities were compared between 1100°C and 1200°C sintering temperature, Archimedes density remained constant as 4.76 g/cm^3 whereas radial shrinkage kept increasing to 13.2 %. Similar to radial shrinkage, dilatometer results proclaimed approximately 4 % shrinkage between 1100 and 1200°C. Table 4.1 summarizes the measured Archimedes density values and radial shrinkages as a function of sintering temperature.

Table 4.1. *Measured Archimedes density and radial shrinkage values for all sintering conditions*

Sintering Conditions	Archimedes Density (g/cm^3)	Radial Shrinkage (%)
1000°C – 12 hours	4.24	7.3
1100°C – 12 hours	4.76	11.8
1200°C – 12 hours	4.76	13.2

The effect of sintering temperature on the grain morphology was also investigated with the help of fractured surface SEM investigations (Figure 4.3).

Sample sintered at 1000°C showed an initial stage of sintering with a lack of densification. When the sintering temperature was increased to 1100°C, sintering and grain growth was observed. The formation of closed porosities was seen along with some open porosities. For the sample sintered at 1200°C, grain boundaries became common because of the grain separation at the triple junctions of the grains. Closed pores within grains were getting bigger.

To sum up the findings so far, one can conclude that the similar behavior of both Archimedes density and radial shrinkage was expected if the number of open and interconnected porosities were decreased in the microstructure. However, it was unlikely that Archimedes Density stayed constant at the same time radial shrinkage showed a significant increment. This could happen only if closed porosities could be measured by Archimedes method. Considering all; a model for densification behavior associated with temperature dependence was built and depicted in Figure 4.4.

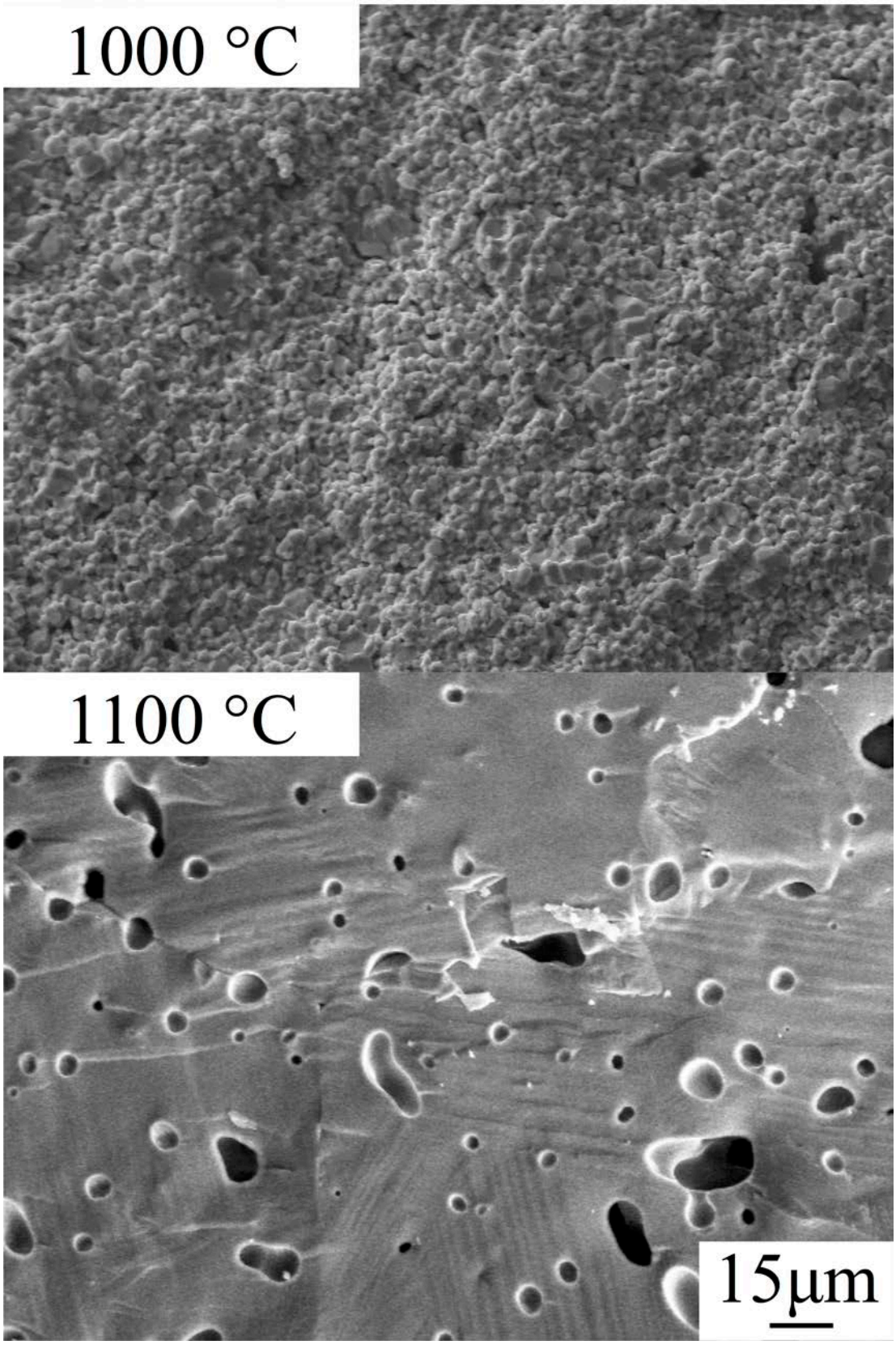

Figure 4.3. *Fractured surface SEM images of LLZO sintered at 1000, 1100 and 1200 °C*

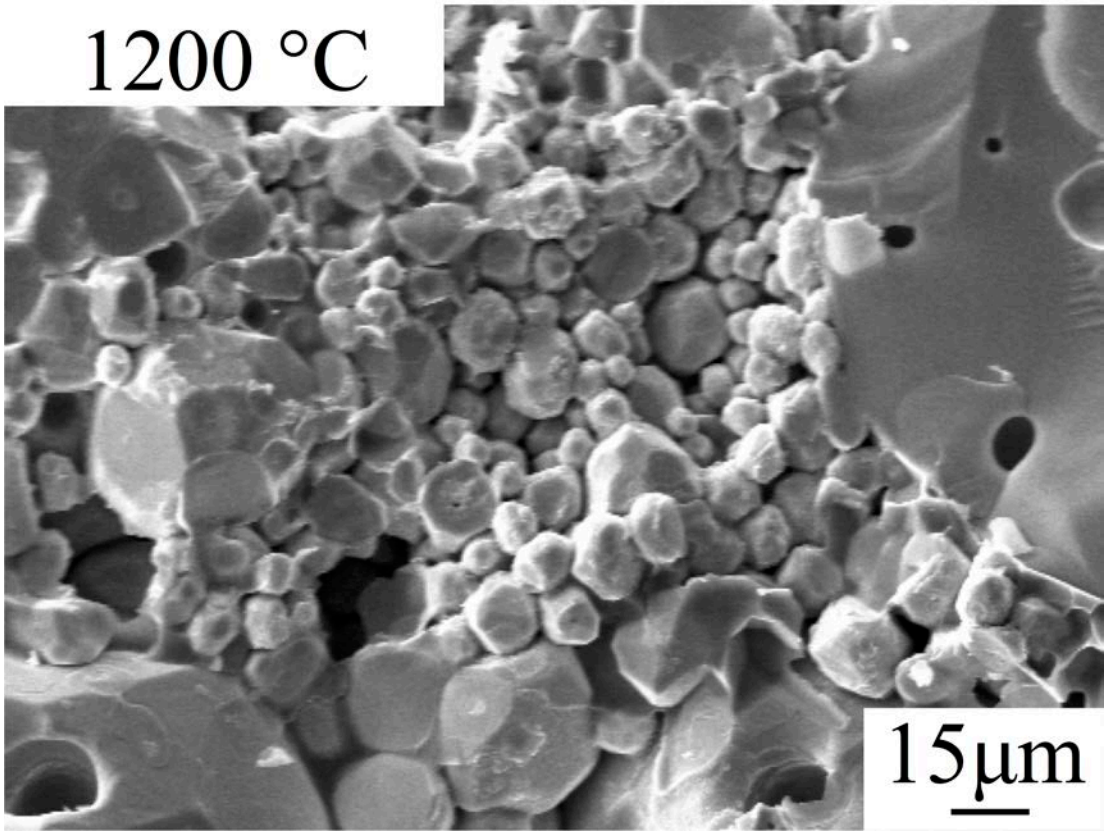

Figure 4.3. (continued) *Fractured surface SEM images of LLZO sintered at 1000, 1100 and 1200 °C*

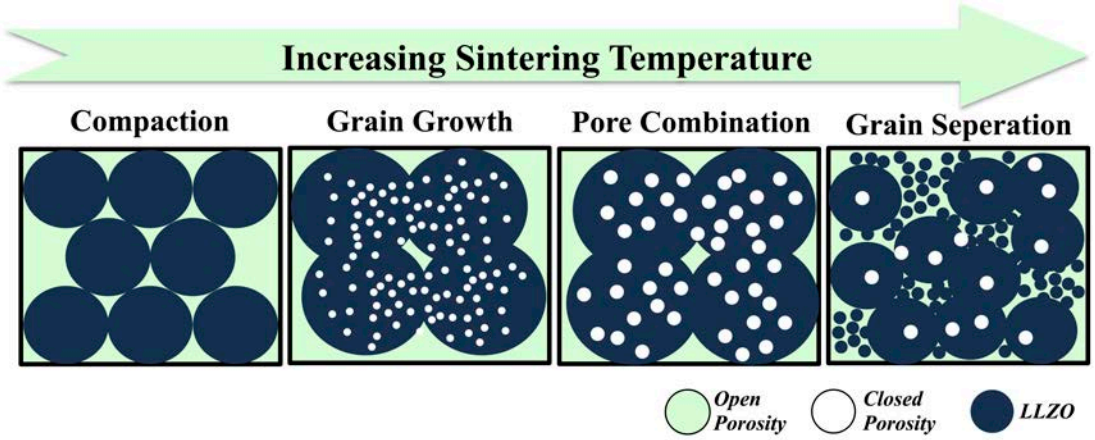

Figure 4.4. *LLZO densification model as a function of temperature*

It can be inferred from the Figure 4.4 that at first instant, densification occurred due to necking and massive grain growth. That causes an increase on all Archimedes density, radial shrinkage and a fast shrinkage on optical dilatometer curve. Increasing the sintering temperature to 1200°C, closed pores were firstly formed within grains,

then, the amount of closed pores per unit area were decreased but their size were increased which is a clue of linking multiple pores and pore coarsening. As a result of the pore linking, smaller sized secondary grains were separated from primary grains and located at the triple junctions of primary grains. Such kind of secondary grain formation is considered to have a positive effect on performance of the as-synthesized electrolytes because of the increment on total number of grain boundaries.

4.4. Conclusion

Radial shrinkage was adapted as an alternative method for accurate densification assessment of LLZO based solid electrolytes in this chapter with the help of optical dilatometer. According to the densification behavior with respect to sintering temperature, Archimedes density was increased with increasing sintering temperature at the initial stage of the sintering. Then, it remained constant at 4.76 g/cm^3 at the subsequent sintering stage. However, radial shrinkage showed a regular increase from 7.3 % to 13.2 % for all sintering stages. A plausible explanation for this phenomenon with the help of fractured surface images was attributed to the conversion of closed porosities into open porosities due to the grain separation caused by multiple pore linking. Grain separation of smaller sized grains (secondary grains) was specifically located at the triple junctions of bigger primary grains.

5. LI DETECTION BY USING MICROSCOPY TECHNIQUES

Li can find itself a wide range of applications especially in energy related areas since it's the lightest metal. However, Li detection by microscopy-based techniques is problematic because of the highly susceptible nature during electron beam irradiation. ToF-SIMS in a Gallium source FIB-SEM is a versatile technique to detect and map Li but the detection of light materials is problematic due to the large ion contaminated zone and low sputtering yield. By combining ToF-SIMS with a recently launched Xe ion source FIB-SEM, which has small ion contamination and high sputtering yield, can produce more realistic data at near surface and below the surface region especially for the detection of lightweight elements such as Li. In this chapter, Li detection and mapping capabilities of ToF-SIMS attached to the FIB-SEM with Ga and Xe ion sources were compared for Al incorporated $Li_7La_3Zr_2O_{12}$ solid electrolyte sample that contains Li-rich regions at triple junctions. Ga and Xe ion sources were compared with the solid-ion interactions based on Monte-Carlo simulations.

5.1. Motivation

Lithium (Li), with its 6.94 g/mole molecular weight, is the lightest metal recorded. Li also has the lowest density (0.53 g/cm^3) among known metals. Such properties make Li and Li bearing compounds as the best candidate for the applications where the weight is important. Alloying and/or making a composite of Li with Al, Mg and Zn metals improve mechanical properties such as interfacial strength and wear [62-64]. Lithium compounds can be used as a sintering additive for ceramic materials [65]. Glasses that contain Li compounds are suitable for wide range of applications for their optical properties [66]. Moreover, LiCl is used as a solid desiccant material for air conditioning since their high hygroscopic behavior [67]. On the other hand, the widest use of Li is for the battery technology used in the mobile equipment and devices such as mobile phones, laptops, electric cars and so on. Li-containing materials can be used either as an electrode (anode and cathode) or as an electrolyte in the battery technology [39, 68].

In order to further develop devices and understand what is happening to Li during the production and usage, it is important to develop and/or use microscopy based Li detecting and more importantly mapping techniques. For the detection of light elements, it is necessary to improve the spatial resolution to below 0.15 nm for lithium

and below 0.05 nm for hydrogen [69]. In this sense, the recent development of the spherical aberration corrector for transmission electron microscopes is a turning point, since the spatial resolution reaches 0.1 nm by the use of corrector. Findlay *et al.* reviewed the annular bright field (ABF) scanning transmission electron microscopy (STEM) image formation mechanism based on the S-state channeling model and the imaging condition to obtain lithium atomic columns in several Li-ion battery materials [70].

With transmission electron microscopy (TEM) based electron energy loss spectrometry (EELS) technique, Li can be detected [71]. On the other hand, diffraction-based TEM techniques like precession electron diffraction (PED), Li-containing compounds can also be identified and mapped [72, 73]. However, due to the high mobility of Li, TEM sample preparation for Li-containing samples need an extra care. In addition, these techniques do not provide large and/or 3D image areas to show the distribution of Li in the multi-grain regions.

Out of SEM-based techniques, wavelength dispersive spectroscopy (WDS) is not suitable whereas only recently very special energy dispersive spectroscopy (EDS) and soft X-ray emission spectroscopy (SXES) detectors are able to detect Li [74]. Electron back-scattered diffraction (EBSD) is capable of showing Li-containing phases [75]. However, there are some difficulties for example sample preparation is difficult for EBSD. Since SEM-based techniques obtain the signals from the rear surface of the sample, it is required not to loose Li from the surface layers to be examined by using EDS, SXES and EBSD. Diffraction techniques like EBSD and PED also require a confirmation based on chemical analysis. Therefore, Li detection and mapping by using microscopic techniques is still a very hot topic for many scientists.

Since the time of flight-secondary ion mass spectrometry (ToF-SIMS) technique counts ionized molecular fragments from the surface, it enables Li detection precisely [76]. Because of its outstanding Li detection capability, it attracts much interest in Li-ion battery researchers. There are recently published papers that show Li and Li-containing compounds in solid electrolyte interface (SEI) [77, 78], cathode surfaces [76, 79] and Li-air discharge products [80] after cycling. Another study showed chemical groups qualitatively by ToF-SIMS [81].

Combining focused ion beam-scanning electron microscopy (FIB-SEM) and ToF-SIMS could give more versatility on sample preparation of Li bearing battery

materials. A specific location of the sample is cut out by FIB process and following that the sample is transferred to the ToF-SIMS system [77, 82]. It enhances the accuracy of results whereas, 3D information and beyond the surface data is not successful with such setup in case of Li since light elements tend to sputter during electron beam irradiation. However, ToF-SIMS attached FIB-SEM setup will be a solution. In ToF-SIMS attached FIB-SEM, the sputtered atoms were collected simultaneously by TOF-SIMS detector during FIB excavation in SEM. As long as excavation takes place, data can be collected. 3D information under the surface is possible. Furthermore, at least two different types of ion sources can be used in FIB-SEM: (i) Gallium and (ii) Xenon. Considering the advantages of using recently developed Xe source in terms of low ion contamination, less damage to the surface and larger analyzed area, none of the above studies mentioned so far used ToF-SIMS analysis of Li compounds by using FIB with Xe ion source.

Therefore, the main aim of this chapter was to compare the detection and mapping capabilities of ToF-SIMS attached to two different FIB-SEM having two different ion source: more common source of Ga against recently developed and less common Xe source. To the best of our knowledge, there is no study found in the literature which focuses on detection and mapping of Li in ToF-SIMS attached Xe ion source FIB-SEM.

In this chapter, Al incorporated $Li_7La_3Zr_2O_{12}$ (LLZO), a solid electrolyte used for all-solid-state Li-ion batteries, that contains deliberately formed Al-rich regions was milled by both Ga and Xe ions by FIB combined with ToF-SIMS in order to compare obtained results from two different ion sources during FIB-SEM. Identifying Al-rich regions found at the triple junctions of Al stabilized LLZO is not well-documented yet and the previous studies reveal that Al could intensify at the triple junctions. Hence, there is no agreement among the scientists whether such regions contain Li or not [46, 83]. Thus, visualizing the Li existence and distribution of Al-rich regions is another outcome of the present chapter.

5.2. Experimental

LLZO was synthesized via solid-state reaction method explained in Section 2.2. In summary, Li_2CO_3, La_2O_3 (Sigma-Aldrich) and ZrO_2 (Inframat) were mixed. 30 mole % Al in the form of Al_2O_3 was used as a cubic stabilizing agent. Powders were calcined

at 900 and re-calcined at 980 °C for 12 hours in a furnace. After that, calcined powders were isostatically pressed into pellet and then sintered at 1100 °C for 24 h. The sintering conditions were selected deliberately not to have 100 % LLZO phase but to have different Li-containing phases such as tetragonal and cubic $Li_7La_3Zr_2O_{12}$, $La_2Zr_2O_7$ and $LiAlO_2$. XRD pattern confirmed this intention.

ToF-SIMS attached FIB-SEMs having two different ion sources like Ga (Tescan GAIA3) and Xe (Tescan XEIA 3) were used to map different elements in Li-containing LLZO solid electrolytes for battery applications. Accelerating voltages for both Ga and Xe ion sources were 30 keV. 1 nA ion beam current for Ga-FIB and 250 pA ion beam current for Xe-FIB combined analysis was used. Total analyzed area for all acquisitions was selected as $15 \times 15\ \mu m^2$.

Monte Carlo simulations were conducted by TRIM Software using both Ga and Xe ion source sputtered onto Lithium metal target. 30 keV ion energy was used for collision depth profiles. All data was gathered from 1000 sputtered Ga or Xe ion.

5.3. Results & Discussions

The XRD pattern of 30 mole % Al containing LLZO pellet sintered at 1100 °C for 24 hours was shown in Figure 5.1.

The pattern could be indexed as cubic LLZO (PDF Card No: 01-080-9103) and $LiAlO_2$ (PDF Card No:00-038-1464). However, there were a group of peak doublets and the small peak at $2\theta=53.5°$ in the detailed view of the dashed area was also indexed as (426) plane of tetragonal LLZO (PDF No: 01-080-6141). Taking into account the reference peak positions of tetragonal LLZO (shown in bold), it was believed that the background between $2\theta=50\text{-}54°$ in the detailed view of the dashed area in Figure 5.1 formed due to the tetragonal and cubic peak overlays.

The polished and fractured surface microstructure investigations of 30 mole % Al containing LLZO pellet sintered at 1100 °C for 24 hours were also carried out by using back-scattered electron imaging mode and their images were presented in Figure 5.2.

Homogeneously distributed and nearly spherical pores from a few microns to tens of microns ranging were observed from the polished surface image in the upper side of Figure 5.2. Such pores could either remain empty or be filled by another compound.

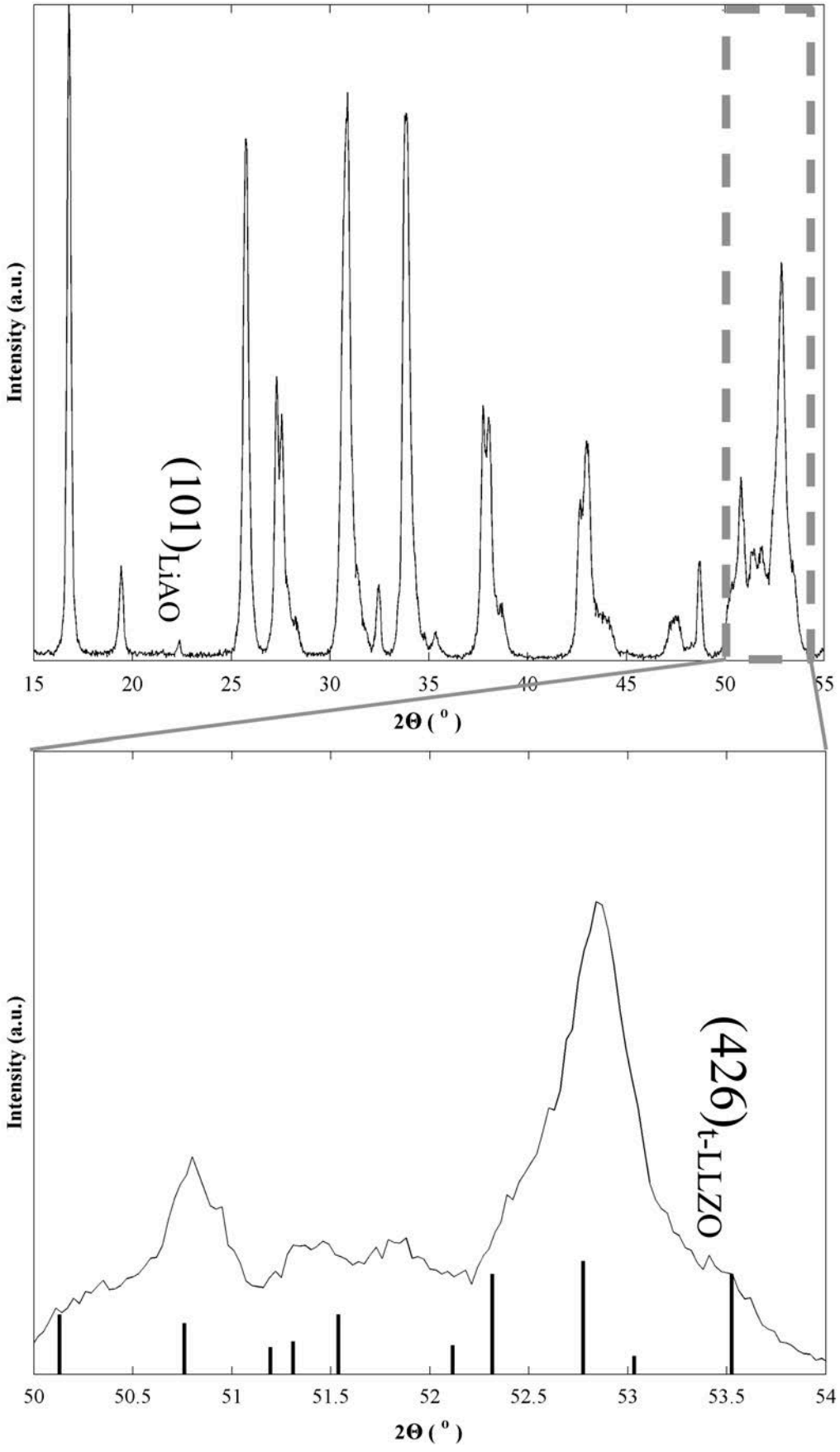

Figure 5.1. *XRD pattern of 30 mole % Al containing LLZO pellet sintered at 1100 °C for 24 hours*

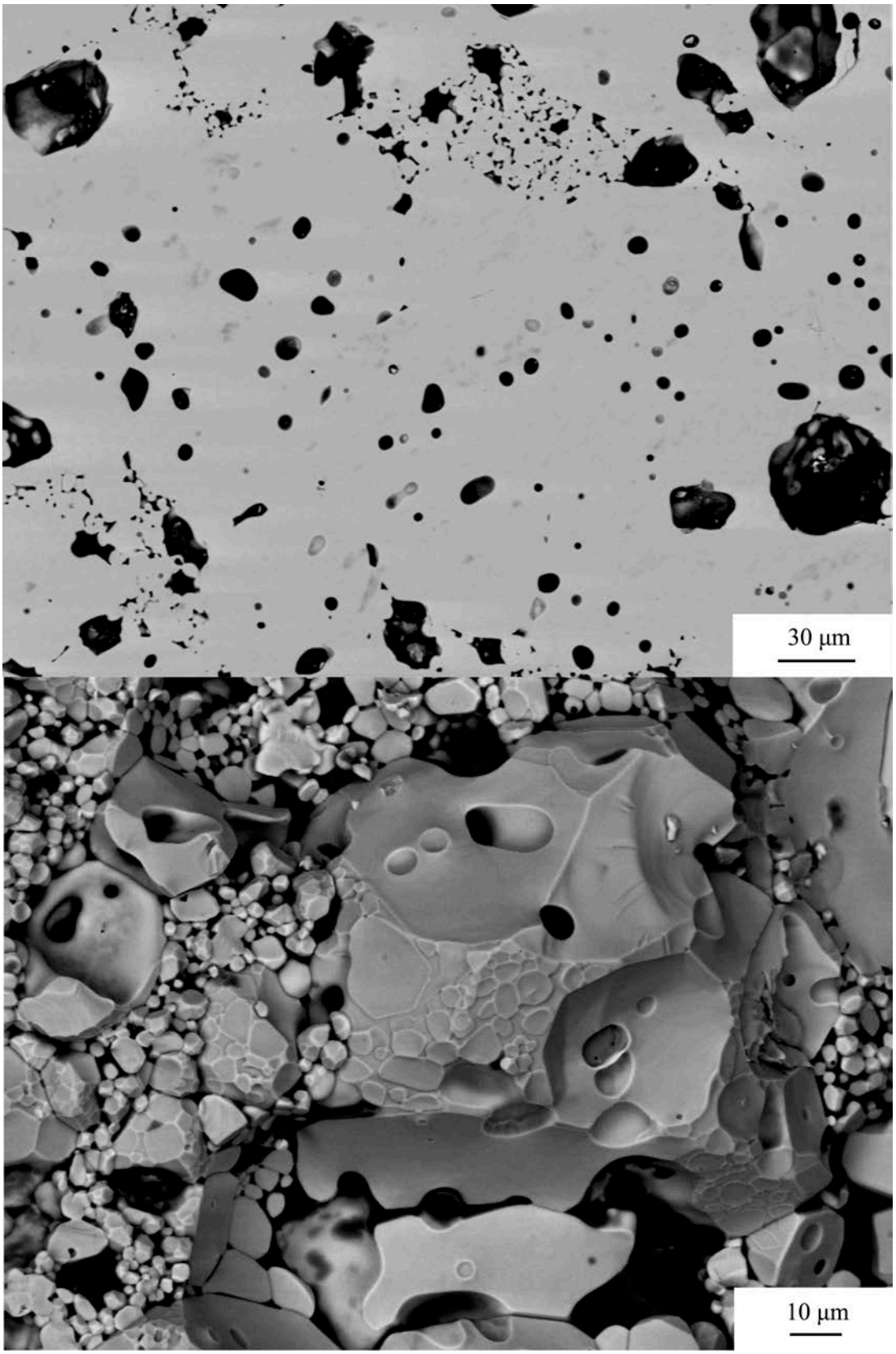

Figure 5.2. *The polished (upper side) and fractured surface (lower side) images of 30 mole % Al containing LLZO pellet sintered at 1100 °C for 24 hours*

The fractured surface image in the lower side of Figure 5.2 illustrated that grains having 30-40 μm diameter consisted of closed porosities. However, there were relatively small, a few micron sized grains, as well. They mainly located at the triple junctions of the bigger grains. Such microstructural formations were tend to increase the amount of porosities where impurity phases could be located at. It should be also mentioned that both transgranular and intergranular were took place.

Figure 5.3 comparatively showed the elemental maps of Li, Al, La and Zr after using both Ga and Xe ion source FIB removal along with back-scattered SEM images. When the SEM images are compared after FIB removal, it can be easily seen that Ga excavation is much smoother in comparison to Xe. According to back-scattered SEM images, microstructure consisted of LLZO grains (whitish contrast), inner-grain pores (blackish contrast) and a secondary phase (dark grey contrast) at the triple junctions of LLZO grains. Li and Al signals were collected from the identical regions forming the ToF-SIMS maps. Therefore, the impurity phase at the triple junction of LLZO grains could be attributed to $LiAlO_2$ detected in combination with XRD analysis. The atomic content of Li and Al in $LiAlO_2$ is equal in stoichiometry but the overall intensity of Al was comparably higher than Li in Ga excavated sample. This can be explained by the damage on Li during Ga ion beam irradiation. Li can travel in different directions in the pellet and form a Li-depleted region during Ga ion beam bombarding resulting in less intensity under more penetrating Ga ions. However, after less penetrating Xe ion source excavation, Li and Al intensity maps were almost similar stating the stoichiometric ratio of Li and Al in $LiAlO_2$. Li intensity in LLZO regions was relatively low due to the extensive Li detection from $LiAlO_2$ region. On the other hand, La and Zr elemental maps after both Ga and Xe ion source FIB removal showed that another intermediate phase $La_2Zr_2O_7$ was located on the outer part of LLZO grains around $LiAlO_2$.

Beam current is one of the parameters that effects strongly on the collected data and map quality. There were an inverse relationship between beam current and the resolution that was discussed before [84].

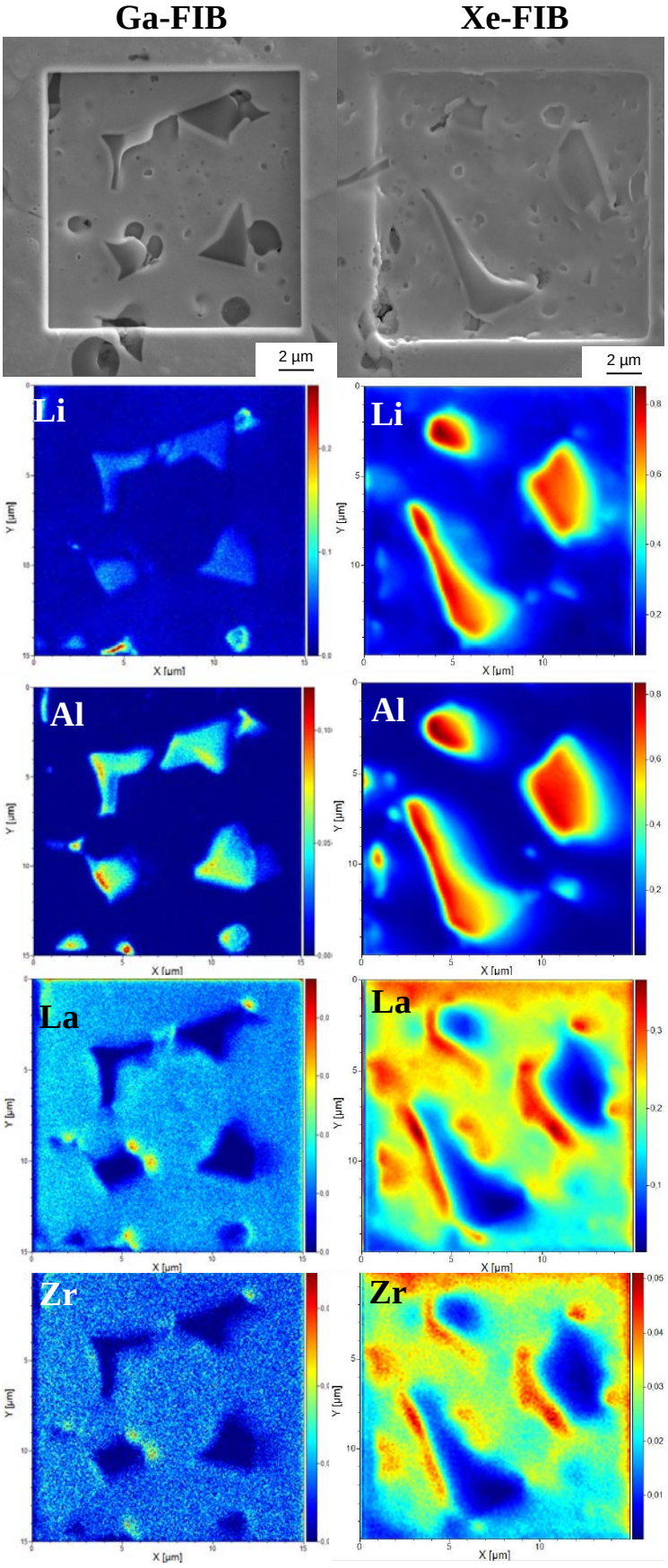

Figure 5.3. *Elemental intensity maps from ToF-SIMS acquisition with Ga and Xe ion sources*

The higher resolution can be obtained thanks to lower beam current. Thus, Li detection resolution was improved when Xe ion source was used since beam current used for building the elemental distribution maps in Figure 5.3 was 1 nA and 250 pA for Ga and Xe ion sources, respectively.

The ion-solid interactions also play an important role on the collected data and map quality presented in Figure 5.3. The Monte Carlo simulations of various ion sources on pure Si surface obtained from SRIM software revealed the increased ion range when ion mass was decreased. The sputtering yield and lateral straggling were also increased [84]. Ga^+ / Xe^+ - Li metal interactions were simulated by using TRIM and the projected range as a function of ion energy was plotted in Figure 5.4.

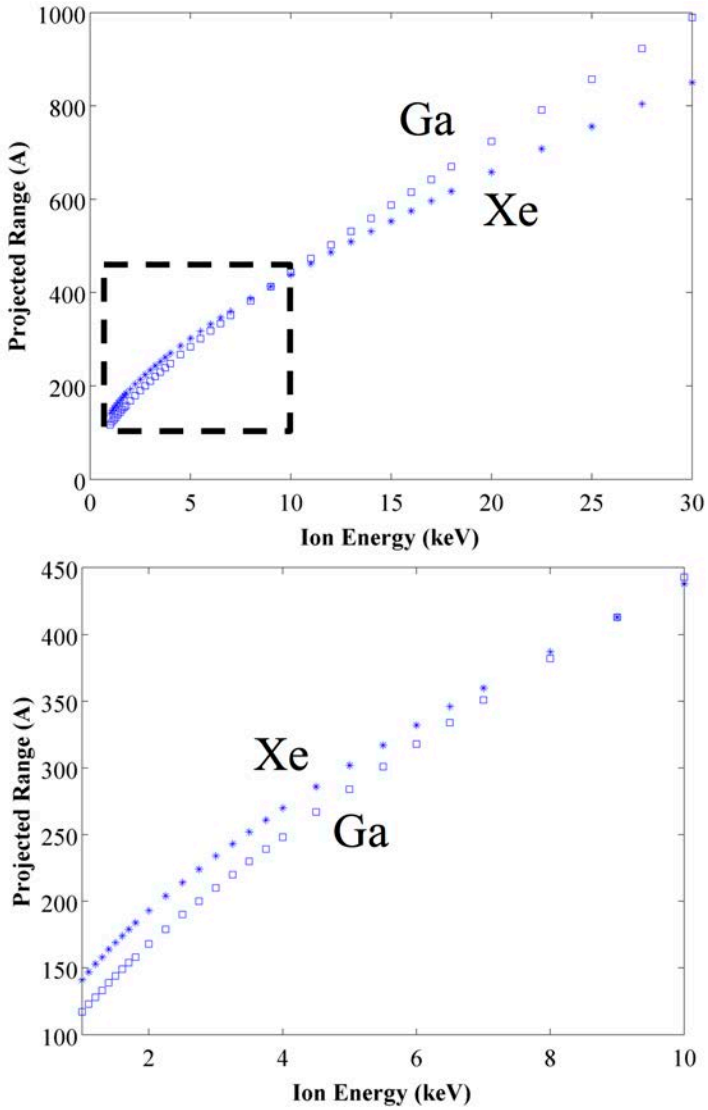

Figure 5.4. *Ga and Xe ion projection range into Lithium*

The projection range in Figure 5.4 could show two different regions. For the ion energies below 9 keV (magnified view from the dashed area), Ga has slightly lower projected range than Xe. However, the projected range of Xe is lower at ion energies higher than 9 keV. Collision depth profiles the vacancies produced with the help of ions from Ga and Xe ions calculated from the TRIM Software were presented in Figure 5.5.

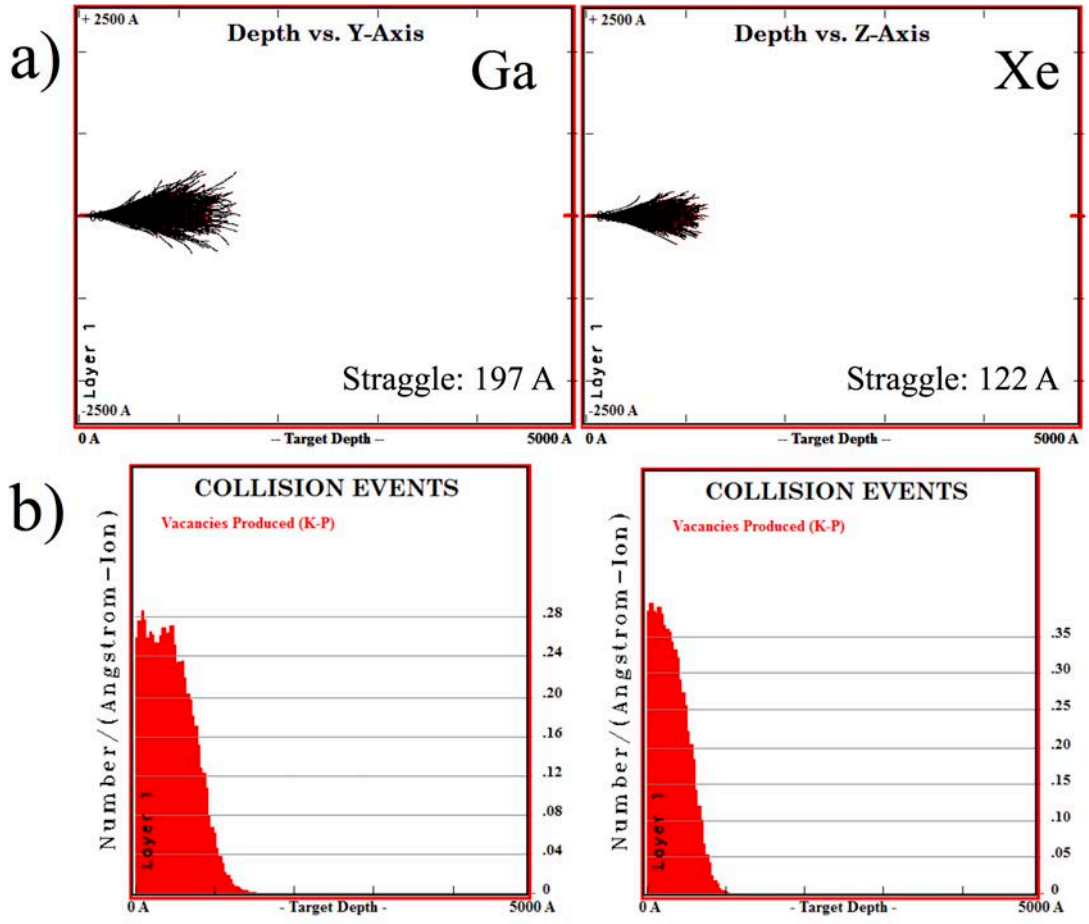

Figure 5.5. *(a) Collision depth profiles and (b) the number of vacancies produced from Ga and Xe ions in Lithium target*

Collision depth profiles obtained from TRIM in Figure 5.5 (a) demonstrated that Ga ions could penetrate up to approximately 1700 Å in depth with a longitudinal straggling of 197 Å. On the other hand, Xe ions could only penetrate into approximately 1100 Å in depth. Longitudinal straggling of Xe ions in Lithium was found as 122 Å. When ions interact with the target atoms, they either eject an atom apart from the target or relocate the atom at any suitable interstitial site through the target. In both two cases, there are vacancies, voids that resulted from ion-solid interactions, formed. In view to

this, the vacancies produced due to ion-solid interactions as a function of depth was calculated by using both Ga and Xe ions (Figure 5.5 (b)). It's worth to state that, Xe ions created vacancies with higher vacancy density (above 0.35 Å-ion) than Ga ions (approx. 0.28 Å-ion). Since the profile which belongs to vacancies created by Ga ion in Figure 5.5 (b) was wider than those created by Xe ion; more vacancies were observed in deeper through target material. According to the Monte Carlo calculations, the number of vacancies produced per each incident ion is found as 394.2 for Ga and 307.6 for Xe. Apparently; more precise surface information can be gathered by using Xe ion source since its lower penetration depth and longitudinal straggling.

To conclude all the findings above, FIB combined ToF-SIMS measurements using Xe ion source are more precise than Ga ion source showing a limited projection range, shallow surface ion contamination and highly efficient vacancy production for detecting and mapping Li, one of the lightweight elements and give more realistic results with high precision and improved resolution.

5.4. Conclusion

Li detection and mapping to show the distribution of Li are very important for the application areas such as Li-ion batteries and other areas that Li is used. ToF-SIMS technique attached to FIB-SEM especially Xe ion source is one of the techniques that is becoming more important in comparison to other Li detecting techniques. With this technique, it is also possible to reconstruct 3D maps and from these maps, it is also possible to quantitatively calculate the volume percent of Li-containing phases. $Li_7La_3Zr_2O_{12}$ was used to evaluate the effect of two different ion sources. To conclude the findings in this chapter;

- Very weak and homogeneous intensities of Li, as a light element, and Al were obtained from triple junctions of grains by using Ga ion source FIB-SEM combined with ToF-SIMS acquisition.
- On the other hand, by using Xe ion source during FIB-SEM with combined ToF-SIMS acquisition, the intensities of Li and Al are dramatically increased. Li and Al were intensified at triple junctions revealing that map constructed by using Xe ion source is better than map obtained from Ga ion source.

- Another outcome of the current study showed that $La_2Zr_2O_7$ was located at the outer side of LLZO grains near the $LiAlO_2$ phase.

In spite of this chapter was focused on $Li_7La_3Zr_2O_{12}$ solid electrolytes as a Li-containing material, the results are valid for all kinds of Li-containing materials.

6. AIR STABILITY ASSESSMENTS OF $Li_7La_3Zr_2O_{12}$ BY FIB-SEM COMBINED TOF-SIMS

$Li_7La_3Zr_2O_{12}$ (LLZO) is newly proposed fast Li ion conducting electrolyte, which is considered to replace organic electrolytes by most researchers. However, there is a lack of prolonged air stability behavior. Li containing surface phases of air exposed LLZO were investigated by ToF-SIMS attached to FIB-SEM. SEM images showed that after air exposure, LLZO surface was covered by surface phases. These phases are identified as mostly Li bearing oxide, hydroxide, carbonate and fluorides according to positive and negative ion mass spectra. A hygroscopic La was not found in these surface phases.

6.1. Motivation

Conventional Li-ion batteries that contain liquid electrolytes address the issue of toxicity and safety since liquid electrolytes are highly toxic and flammable. Nowadays, oxide type ceramic electrolytes are newly emerging candidate for replacing liquid electrolytes. However, their main drawbacks are relatively low ionic conductivity and poor contact properties [20, 25, 85]

Among them, cubic $Li_7La_3Zr_2O_{12}$ (LLZO) is recently studied oxide based solid electrolyte that shows very close ionic conductivity values with liquid electrolytes. Reported studies of LLZO are quite new and available since 2007 [25]. Hence, understanding the nature of LLZO is not well-documented. Vast majority of the studies related to LLZO focuses on the synthesis optimization [45, 86, 87] and enhancing electrochemical performance [27, 88, 89], but their interfacial properties, prolonged usage potential is rarely studied.

According to our knowledge, a study focused on stability of LLZO in different aqueous solutions uses impedance spectroscopy techniques to discuss the effect of water [89]. Another study based on water and air stability of LLZO discussed the pH changes when LLZO immersed in water and the samples were imaged by using Scanning Electron Microscopy techniques for air stability evaluation. They conclude with Li and La leave the pellet to form hydroxide phases in grain boundaries thus, increases pH [88].

As it was mentioned in Section 5.2, Time of Flight - Secondary Ion Mass Spectroscopy (ToF-SIMS) technique counts elements that leave from the surface

enabling Li detection precisely. Because of this, recently published papers related to Li and Li containing compounds only focused on Solid Electrolyte Interface (SEI) [77, 78], cathode surfaces [76, 79] and Li-air discharge products after cycling [80] and depth profile of chemical groups in LLZO qualitatively by ToF-SIMS [81]. However, there is no direct study reporting the elemental compositions of particles formed after air exposure. In the present study, FIB-SEM combined ToF-SIMS method was used to identify the phases formed at the surface after air exposure.

6.2. Experimental

LLZO was synthesized via solid-state reaction method. Firstly, Li_2CO_3 (Merck) was dried at 200 °C, whereas La_2O_3 (Sigma-Aldrich) and ZrO_2 (Inframat) were dried at 900 °C before mixing to get rid of the hydroxides and humidity. 20 mole % Al in the form of Al_2O_3 (Ceralox) was used as cubic stabilizing agent and improve sinterability as documented most of studies [44-46, 54, 90]. Stoichiometric amounts of powders were mixed in agate mortar grinder (Retsch RM200). 15 % of excess Li as Li_2CO_3 was added in order to compensate Li losses during heat treatments. Powders were calcined at 900 and re-calcined at 980 °C for 12 hours in a muffle furnace (Nabertherm). Between each calcination step, powders were reground. After that, 2 g of calcined powders were isostatically pressed into pellet (16 mm diameter) at 290 MPa. Then, as-prepared pellet were sintered at 1100 °C for 24 h within a powder bed containing calcined powders. Alumina crucible was used for all heat treatments. 2 °C/min heating rate was set in order to minimize unexpected Li losses during heat treatments.

For SEM investigations, the pellet was firstly ground using 2-propanol as coolant and polished by using mechanical polisher (Buehler, Minimet 1000). During mechanical polishing, water-free solutions (AKASEL – DiaDoublo Water Free Diamond Suspensions) were used to avoid contacting of water to the LLZO.

In order to determine the air stability of the as-synthesized LLZO samples, pellets were exposed to air for a week and the morphological discussions were carried out by FIB-SEM (Tescan Xeia) combined ToF-SIMS technique by using Ga ion source. ToF-SIMS and FIB-SEM parameters were the same as it was explained in Section 5.2.

6.3. Results & Discussion

The SE image of freshly polished surface was given in Figure 6.1.

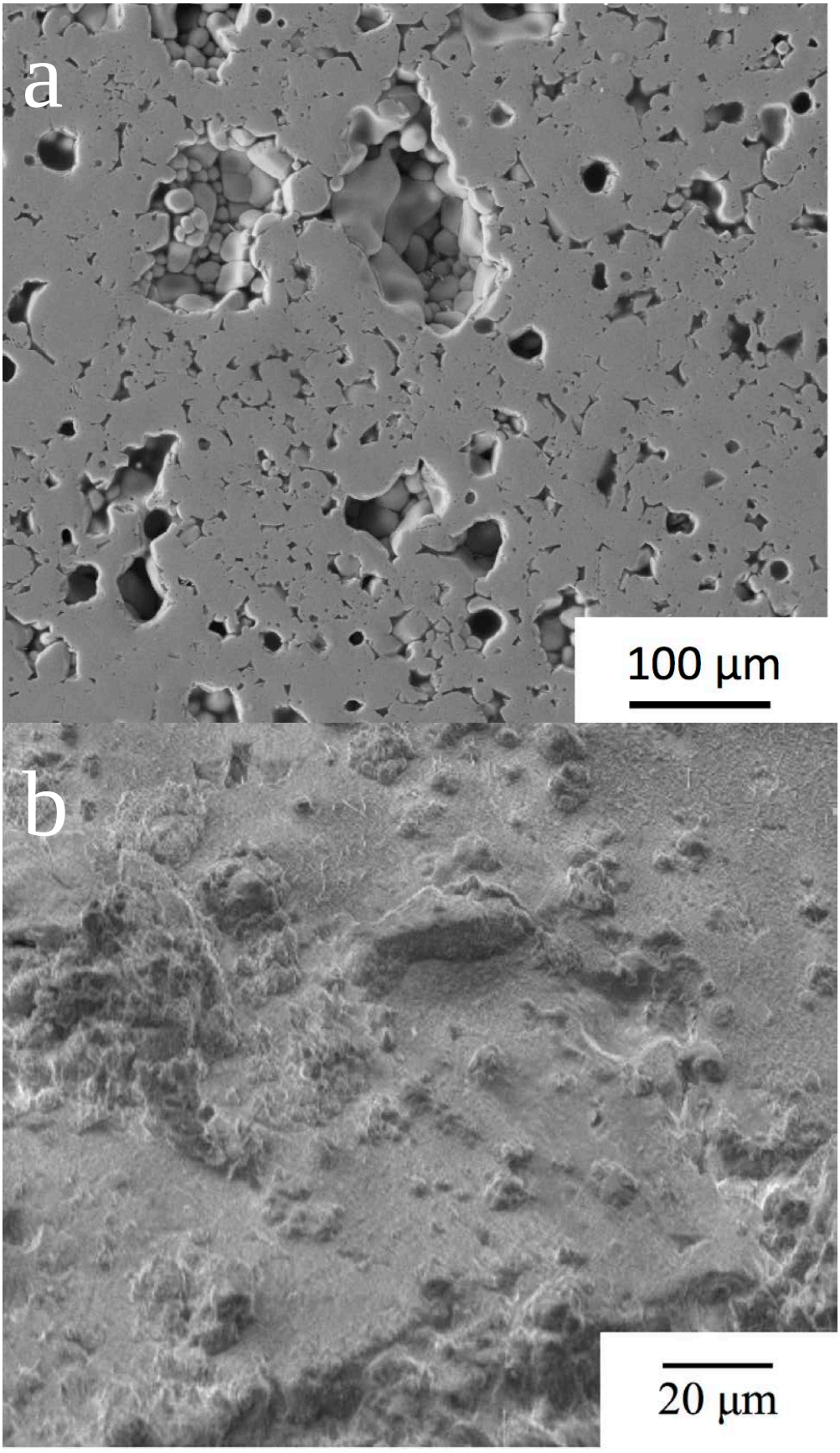

Figure 6.1. *SE images of (a) freshly polished (b) 1-week air exposed LLZO pellet*

Wide range of various sized porosities was seen in Figure 6.1 (a). There were two types of porosities in the microstructure. First type was outer-grain porosities that were located at triple junctions of grains. Other type of them was inner-grain porosity. All types of porosities and their formation mechanism was explained in detail in Section 4. After that, the pellet was left in open-air atmosphere for a week and secondary electron SEM images of LLZO surface without any additional sample preparation were presented in Figure 6.1 (b) After 1-week air exposure, the surface morphology was dramatically changed. There was a continuous wavy film that was a result of the LLZO covered with dirt and unwanted reaction deposits.

From the image presented in Figure 6.1 (b), the thickness and the homogeneity of the surface film cannot be identified. Therefore, cross-sectioned surface was prepared by using FIB-SEM and the back-scattered cross section image was given in Figure 6.2.

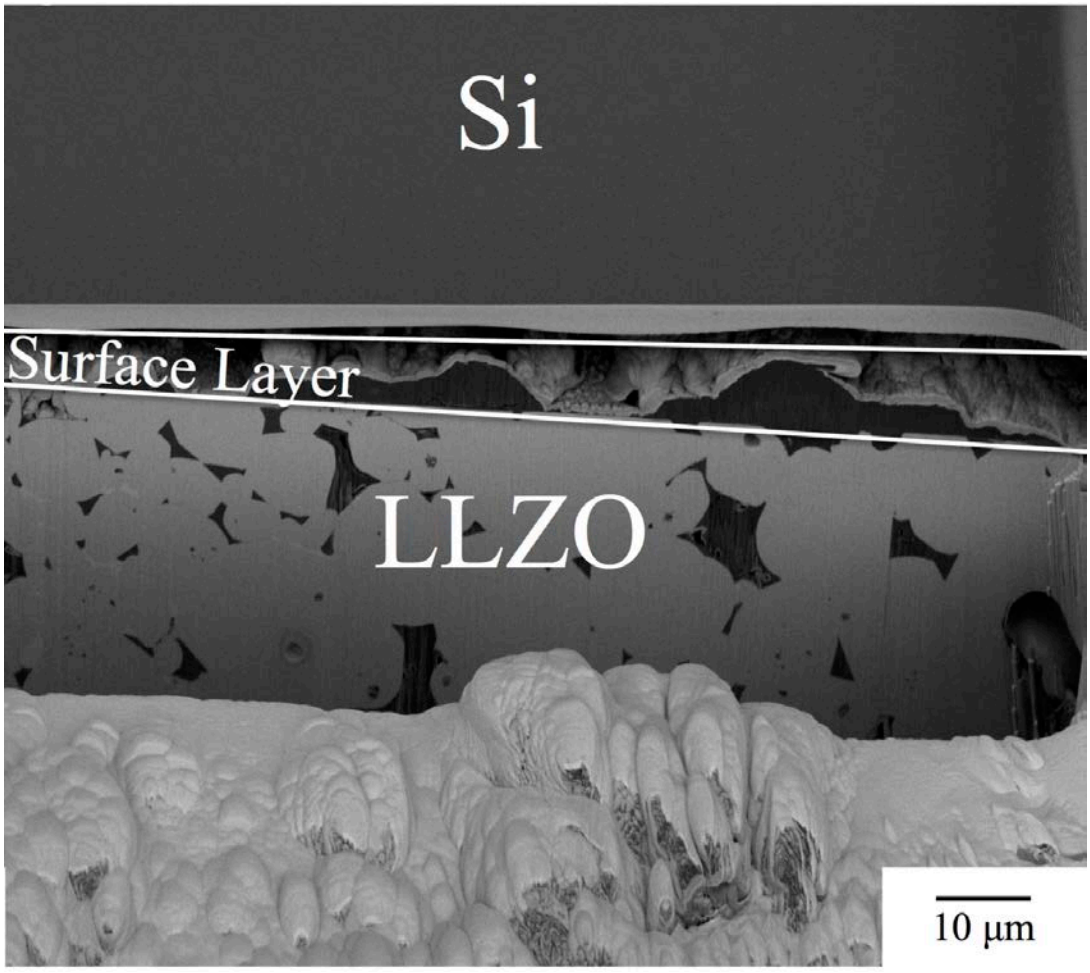

Figure 6.2. *BSE image of air exposed LLZO sample cross section view*

According to the BSE images in Figure 6.2, one could conclude that the thickness of the layer is a few micrometers and almost homogeneously distributed all over the surface. Besides, there were some bubbling formations beneath the surface layer. Figure 6.3 showed the microstructure of 1-week air exposed LLZO sample before and after FIB excavation in order to identify their chemical composition.

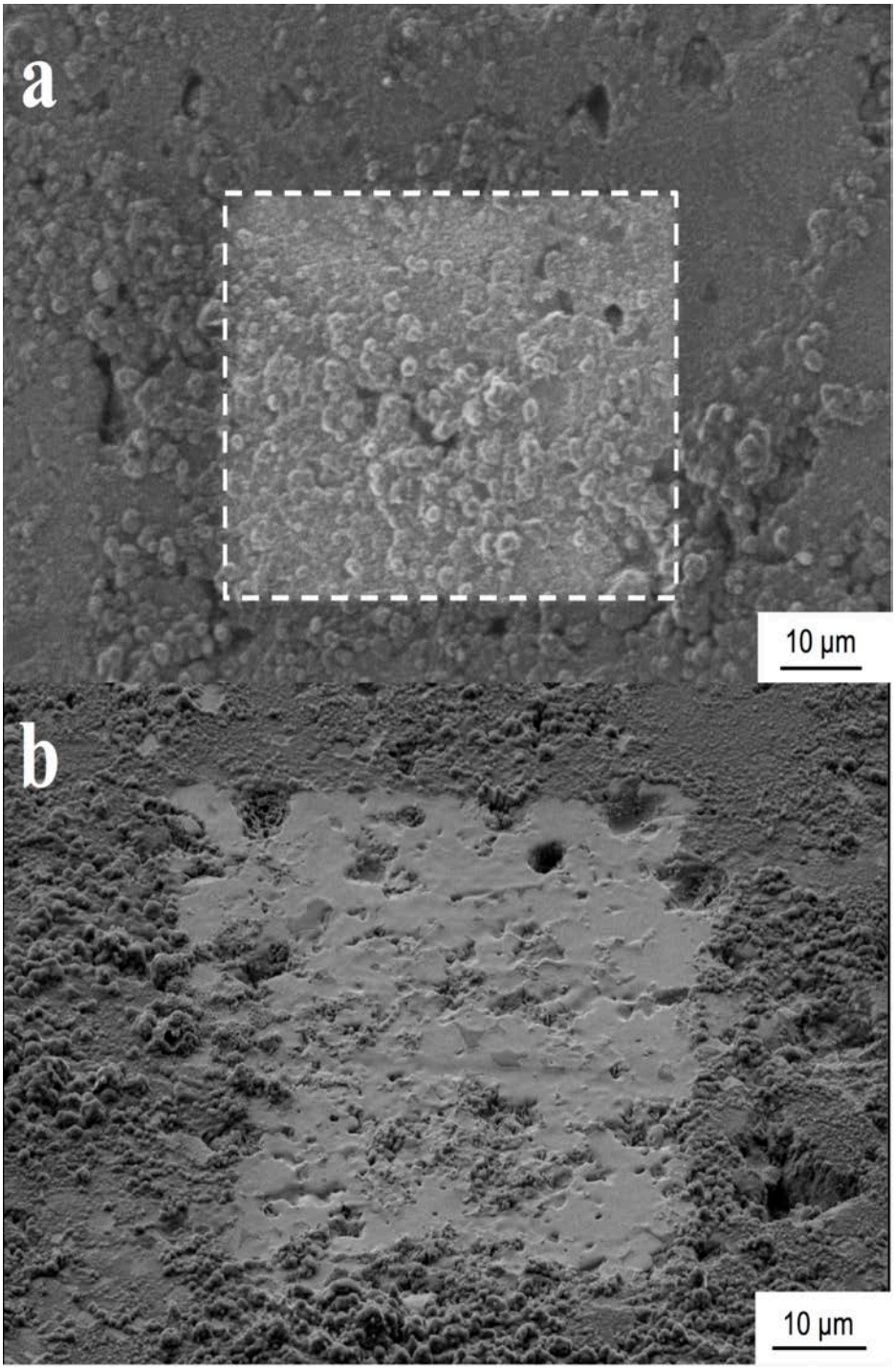

Figure 6.3. *SE images of 1-week air exposed LLZO samples before (a) and after (b) FIB excavation*

The dashed area in Figure 6.3 (a) was bombarded with Ga ions and scattered ions from the sample surface were collected by ToF-SIMS attachment. After bombardment, the secondary electron image of LLZO sample was presented in Figure 6.3 (b). Positive and negative mass spectra acquired from ToF-SIMS were depicted in Figure 6.4.

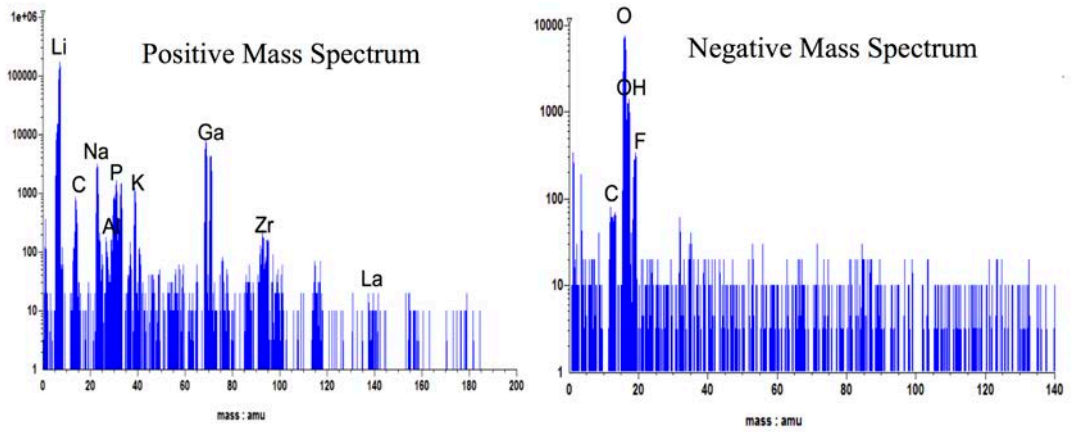

Figure 6.4. *Positive and negative mass spectra aquired from ToF-SIMS*

As it can be seen from the Figure 6.4 that, detected cations were Li^{+}, Na^{+}, P^{5+}, K^{+}, Al^{3+}, Zr^{4+} and Ga^{+}. Furthermore, the anions collected by ToF-SIMS detector were O^{2-}, OH^{-}, F^{-}. Carbon was observed both in negative and positive mass spectra. Thus, it can be referred from the Figure 6.4 that oxide, hydroxide, fluoride and carbonate compounds of Li could be obtained from the surface. It's worth to note that the Ga peak is observed due to the back-scattered Ga ions that were used to excavate the sample surface. Na, P, K and F peaks were also observed due to the dust coming from the air conditions. The presence of the Zr peak having a weak intensity in positive mass spectrum was believed to be due to the minute amount of Li_2ZrO_3 phase on the surface. On the other hand, a specific attention should be paid for the La peak. A study discussing the water stability of LLZO claimed that a dramatic increase on the pH could be attributed to the formation of LiOH and $La(OH)_3$ when LLZO was immersed into the water [88]. However, since there was no La peak observed in positive mass spectrum in Figure 6.4, the findings mentioned above emphasized the strong stability of La in air.

6.4. Conclusion

The air stability of LLZO is assessed by using freshly polished and 1-week air exposed samples by using ToF-SIMS analysis. After air exposure for a week, a few micrometer-sized continuous wavy film, which is the reason of side reactions and dirt, with non-uniform thickness was observed. Bubbles were formed in specified regions of LLZO surface. After that, surface film is excavated by using Ga ions in FIB system and the sputtered ions were collected by ToF-SIMS attachment. Li^{+}, Na^{+}, P^{5+}, K^{+}, Al^{3+}, Zr^{4+} and Ga^{+} were found in the positive spectrum of the excavated area whereas the negative spectrum contains O^{2-}, OH^{-}, F^{-} ions along with C in both spectra. Air exposure results with Li_2ZrO_3 formation apart from the LLZO structure since there are Li and Zr peaks in positive spectrum. On the other hand, La peak is not observed pointing out the stable La compounds within LLZO structure.

7. SOLUTION BASED SYNTHESIS OF $Li_7La_3Zr_2O_{12}$

Stabilization of cubic $Li_7La_3Zr_2O_{12}$ phase, one of the most promising solid electrolytes for Li-ion batteries, has been extensively studied in terms of various stabilizer additions in solution-based systems. However, different dissociation behavior of precursors on the cubic LLZO phase stabilization has not been studied. In this chapter, an understanding for the stabilization of cubic $Li_7La_3Zr_2O_{12}$ phase by using $ZrOCl_2$ and $ZrO(NO_3)_2$, which are having different dissociation behavior, with 0-40 mole % Al addition was offered. The role of nitrate ions within solution was also assessed.

7.1. Motivation

High-energy density Li-ion batteries are indispensable member for long-range Electrical Vehicles (EVs) applications. Nowadays, highly flammable and explosive organic based liquid electrolytes prevent the widespread use of EV's in the worldwide market due to safety requirements.

Recently, to improve safety, a high effort for replacing the widely used liquid electrolytes has been put forward. Solid electrolytes show outstanding advantages over organic based liquid electrolytes such as excellent battery life-time, electrochemical and thermal stability and enhanced safety [39]. Among them, $Li_7La_3Zr_2O_{12}$ (LLZO) having a cubic garnet structure is highly resistant to hydration, stable in air and shows high ionic conductivity [38, 88].

Cubic phase stabilization is the main challenge for synthesizing LLZO since its room temperature stable structure is tetragonal [91]. Several studies revealed that Al can help stabilization of cubic phase at room temperature and also increases the ionic conductivity [46, 54, 92]. Along with stabilizer addition, bonding characteristics of each precursor play an important role in the performance of LLZO. However, very few studies are based on the systematic investigation of different sources. It's been reported that simply changing Li source from Li_2CO_3 to LiOH in solid-state reaction synthesis results in lower sintering temperature, higher relative density and increased ionic conductivity since the bond type and required energy to break them are different for Li_2CO_3 and LiOH. The study aimed to discuss the microstructural and electrochemical performance differences for both Li sources and cubic phase stabilization was not the scope of the chapter [29]. In a very recent work, we've compared the effect of Al source

on the electrochemical performance of cubic LLZO phase during solid state reaction synthesis. In contrast, there is no study found in the literature discussing the effect of different sources on the stabilization of cubic LLZO phase for solution-based synthesis methods.

In solution based synthesis of LLZO, water-soluble salts of Li, La and Al dissociates by providing a single valence Li^{+}, La^{3+} and Al^{3+} ions within solution [88, 93]. However, two of water-soluble Zr sources have different dissociation behavior. $ZrOCl_2$ produces Zr^{4+} ions whereas the dissociation of $ZrO(NO_3)_2$ provides ZrO^{2+} ions in the aqueous solutions [94-97].

In the light of the reasons given above, we investigate the effect of $ZrOCl_2$ and $ZrO(NO_3)_2$, as Zr sources having different dissociation behavior, on cubic phase stabilization of 0 – 40 mole % Al containing LLZO via solution-based techniques. To the best of our knowledge, the present study aims for the first time the cubic phase stabilization of LLZO based on the multivalent dissociation behavior of precursors in solution-based LLZO synthesis. We also introduce an understanding of the phase stabilization mechanism in combination with the crystal structure and bonding information of each atom in tetragonal and cubic LLZO phases and the role of anions within the solution.

7.2. Experimental

LLZO powders were synthesized via citrate-nitrate route. Stoichiometric amounts of high purity $LiNO_3$ (Fluka), $La(NO_3)_3.6H_2O$ (Alfa Aesar), $Al(NO_3)_3.9H_2O$ (Alfa Aesar), $ZrO(NO_3)_2.nH_2O$ (Alfa Aesar) or $ZrOCl_2.8H_2O$ (Merck) were first dissolved in deionized water (ρ=0.55 mS/cm) under moderate stirring condition for 12 hours. Then, citric acid (Anhydrous, Merck) and Ethylene Glycol (Anhydrous, Sigma-Aldrich) were added as organic complexing agent and chelating agent, respectively. The molar ratio of organic additives and metal ions were selected as 62:38 whereas molar ratio of Citric Acid and Ethylene Glycol were 60:40 as described somewhere else [92]. All chemicals were used as received without further treatment. 15 % mole of excess $LiNO_3$ as a Li source was added in order to compensate Li losses during calcination. The resulting solution was heated at 120°C under moderate stirring conditions. White precipitates were obtained after gelation and dried at 150 °C overnight. Brownish dried gel were calcined at 1000 °C, which is the highest calcination temperature possible to produce

without excessive Li losses, for 6 hours in a muffle furnace. An alumina crucible was used for all heat treatments. 2 °C/min heating rate was set in order to minimize unexpected Li losses during heat treatments.

After calcination, powders were roughly ground and existing phases were determined by using X-ray diffractometer (XRD – Bruker D8 Advance) between 15° - 55° with 2°/min scan speed and a step size of 0.02° by using Cu K_α radiation. Then, morphological and elemental analyses of each pellet were carried out by using scanning electron microscope (SEM-Zeiss SUPRA 50VP) attached with an energy dispersive spectrometer (EDS - Oxford INCA).

3D models of tetragonal and cubic LLZO were constructed with CrystalMaker 9.2.7 Software by using space groups of $I4_1/acd$ (COD ID: 1545086) and Ia-3d (COD ID: 7206766) respectively. Dilatometer measurement conditions were the same as the conditions explained in Section 4.2.

The calcined powders (1.5 g) were isostatically pressed into a pellet (15 mm diameter) with a pressure of 290 MPa and sintered within its powder bed at 1100 °C for 12 hours for the purpose of achieving a high relative density. Both sides of powder bed sintered pellets were ground with 2000 grit SiC abrasive papers and Au-Pd blocking electrodes were coated with the sputtering technique for 40 seconds. As-prepared pellets were placed into 2-electrode split test cell (EQ-STC, MTI) and ionic conductivity measurements were carried out by using AC Impedance method with a frequence range between 10 Hz – 1 MHz and 20 mV/rms perturbation voltage. Gamry Reference 600 potentiostat/galvanostat system and Gamry Framework software were used for measurements and fitting. A flowchart of synthesis and sintering procedure was summarized in Figure 7.1.

7.3. Results & Discussion

7.3.1. Citrate-Nitrate Approach

XRD patterns of the powders calcined at 1000 °C for 6 hours for 0-40 mole % Al with $ZrOCl_2$ as Zr source were given in Figure 7.2.

From XRD patterns, it's obvious that without Al addition, tetragonal LLZO was obtained along with some impurities such as Li_2ZrO_3 (PDF No: 01-070-8744), $La_2Zr_2O_7$ and Monoclinic-ZrO_2 (PDF No: 00-037-1484). When Al added, Li_2ZrO_3 content was increased whereas $La_2Zr_2O_7$ content was decreased.

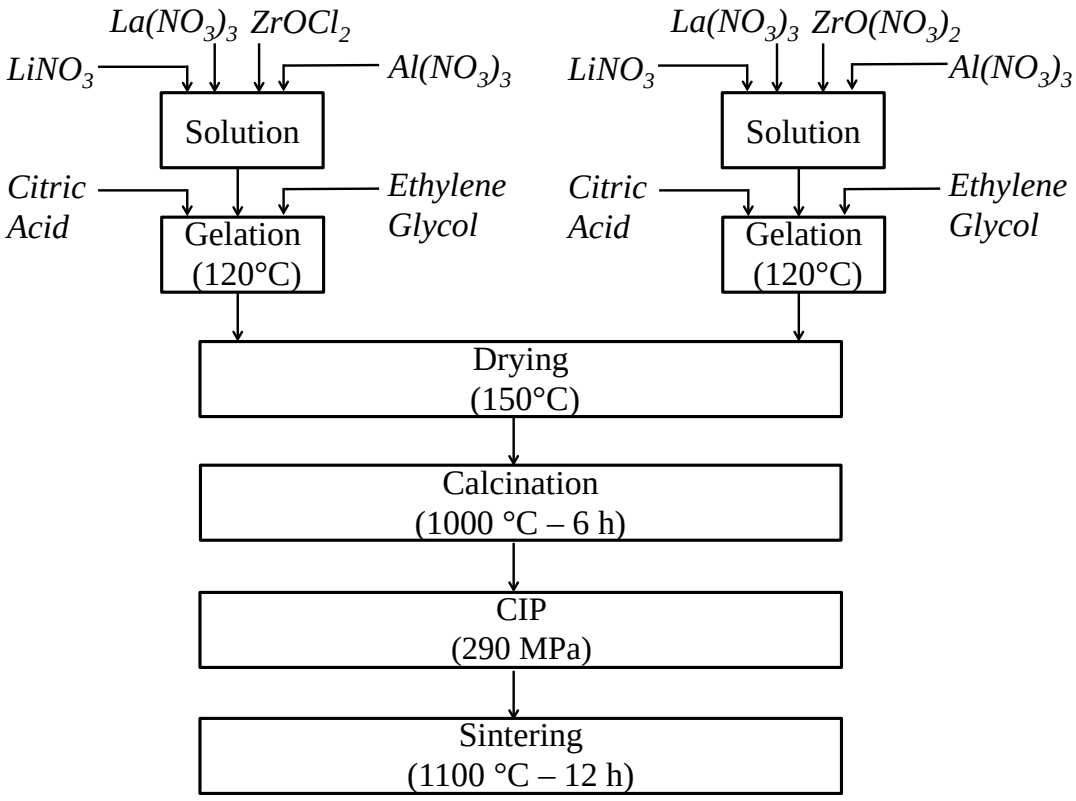

Figure 7.1. *Citrate-Nitrate synthesis flowchart*

Crystal structure of LLZO was still tetragonal. But, there was a background in the XRD pattern between 2θ = 50°-55° which might be a sign of cubic structure with a very small grain size. During tetragonal to cubic phase transformation, peak doublets indicating the existence of tetragonal phase were disappeared and a new peak formed. After 20 mole % Al addition, crystal structure turned out to be fully cubic LLZO (PDF No:01-078-6708) phase with a minor impurity of Li_2ZrO_3. Comparing the effect of 20 and 30 mole % Al addition, the content of minor impurity phase increased and additionally $La_2Zr_2O_7$ was formed. On the other hand, when Al addition was increased to 40 mole %, a small increase in Li_2ZrO_3 content and $LaAlO_3$ formation was observed.

Figure 7.3 showed the XRD patterns of powders calcined at 1000 °C for 6 hours for 0-40 mole % Al addition with $ZrO(NO_3)_2$ as Zr source. Tetragonal form of LLZO (PDF Card No: 01-080-6141) was obtained for all Al contents and there were also remnants of La_2O_3 (PDF Card No: 01-083-1344) as well as $La_2Zr_2O_7$ (PDF Card No: 01-071-2363) phases.

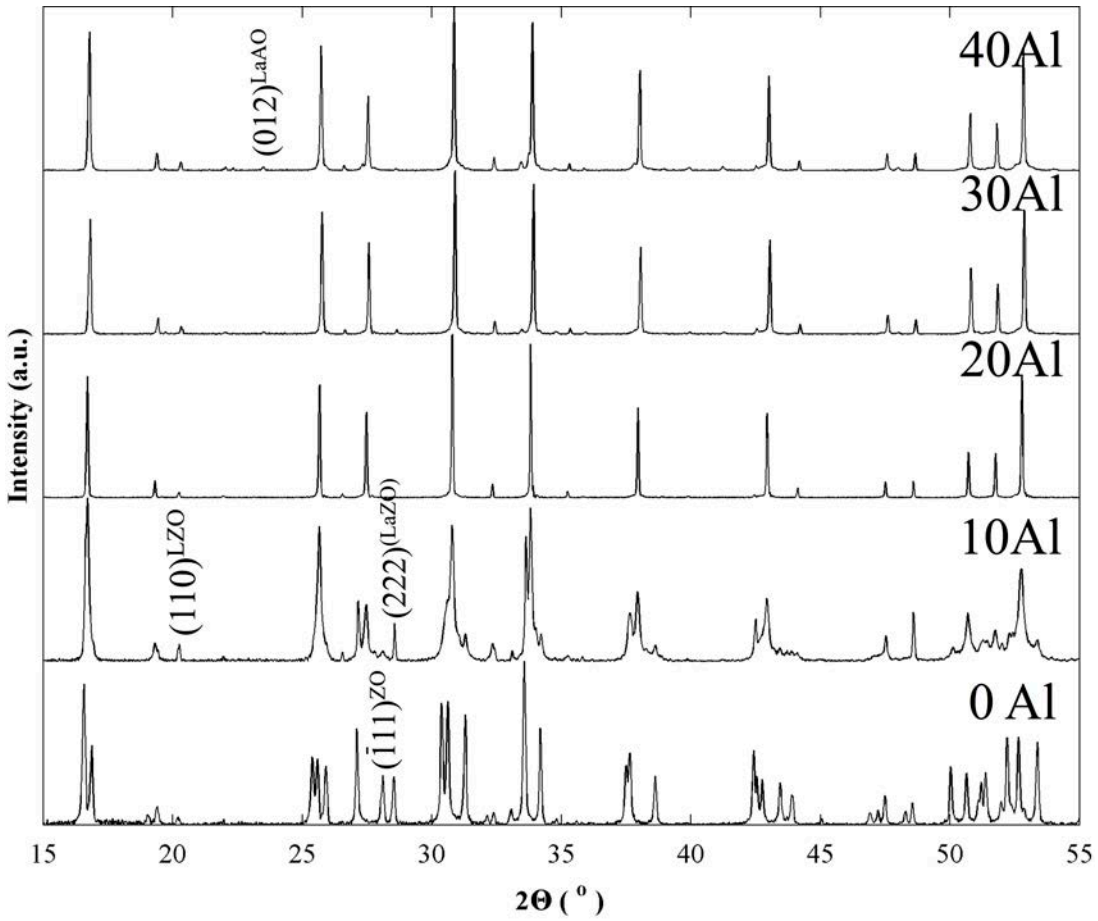

Figure 7.2. *XRD patterns of LLZO powders synthesized by using $ZrOCl_2$ with different amount of Al addition (LZO: Li_2ZrO_3, LaAO: $LaAlO_3$, LaZO: $La_2Zr_2O_7$, ZO: ZrO_2) –All the other peaks in 0Al and 10Al belong to tetragonal; in 20Al, 30Al and 40Al belong to cubic LLZO phase*

When Al was increased to 20 mole %, amount of La_2O_3 and $La_2Zr_2O_7$ were gradually decreased. On the other hand, Li_2CO_3 (PDF Card No: 01-080-1307) formation was detected for 20 mole % and the Li_2CO_3 formation increased until 40 mole % Al addition. $LaAlO_3$ (PDF Card No: 01-070-4122) amount was also increased with increasing Al content up to 40 mole %. In contrast, the La_2O_3 and $La_2Zr_2O_7$ contents were decreased with increasing Al content and disappeared at 30 mole % Al addition. There was no sign of ZrO_2 in the case of 0 mole % Al addition. However, when Al content was increased, ZrO_2 (PDF No: 00-037-0031) was also formed and kept increasing. $La_2Li_{0.5}Al_{0.5}O_4$ (PDF Card No: 01-084-1470) was formed at 40 mole % Al content which is above the maximum solubility of Al determined within LLZO structure [26]. Li_2CO_3 was formed beginning with 20 mole % Al and gradually increased with increasing Al content.

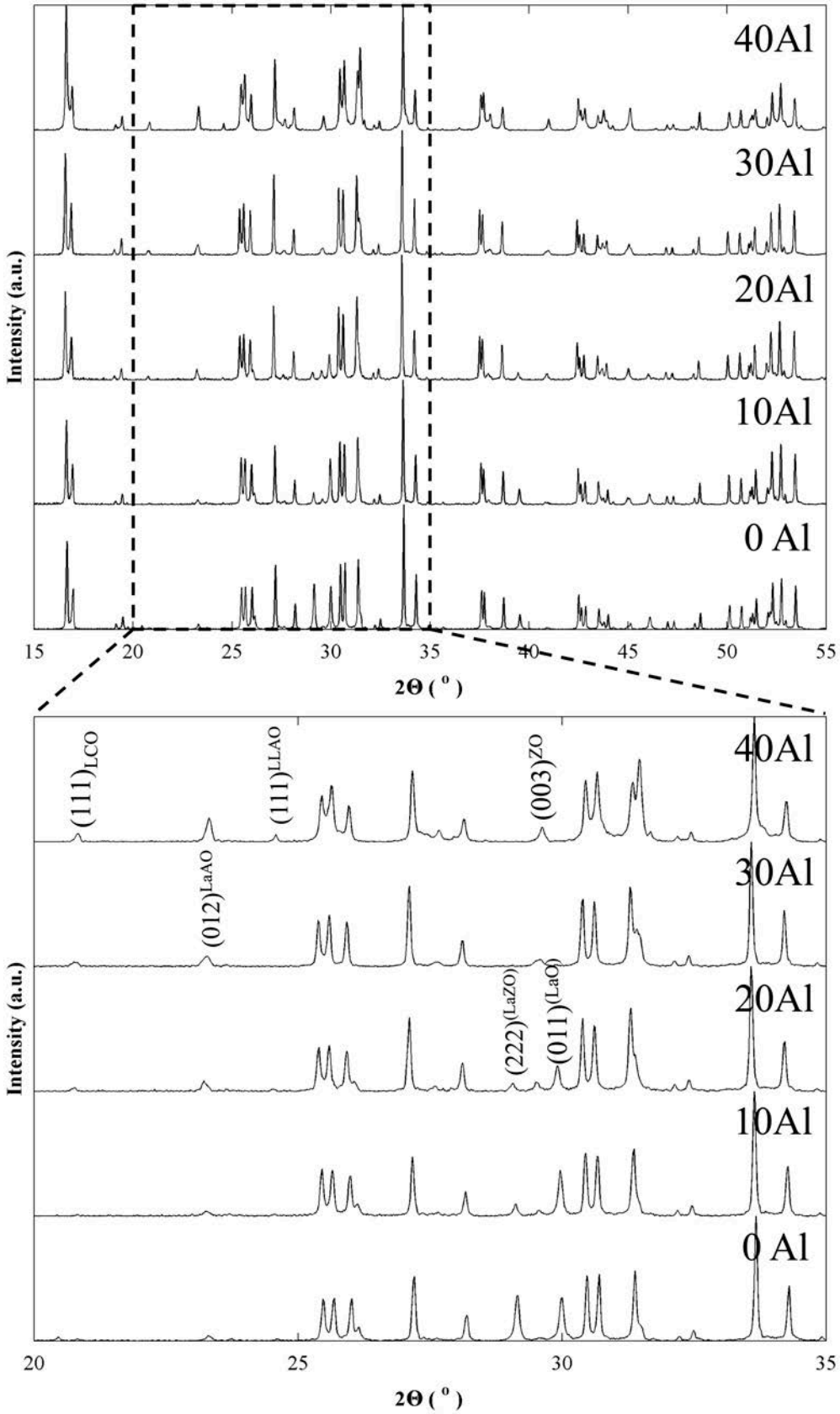

Figure 7.3. *XRD patterns of LLZO powders synthesized by using $ZrO(NO_3)_2$ with different amount of Al addition. (LCO: Li_2CO_3, LaO: La_2O_3, LLAO: $La_2Li_{0.5}Al_{0.5}O_4$) The remaining peaks belong to tetragonal LLZO. No cubic phase formation.*

When Al increases, $LaAlO_3$ and ZrO_2 formation was enhanced whereas the amount of $La_2Zr_2O_7$ was reduced. Considering the $LaAlO_3$ and $La_2Zr_2O_7$ formation reactions in Equation (7.1) and (7.2) below, La_2O_3 - Al_2O_3 reaction is more favored than La_2O_3 – ZrO_2 reaction (Unfortunately Gibbs Energy change data is not available in the open literature).

$$La_2O_3 + Al_2O_3 \rightarrow 2LaAlO_3 \quad (7.1)$$

$$La_2O_3 + 2ZrO_2 \rightarrow La_2Zr_2O_7 \quad (7.2)$$

When Al content exceeds the maximum solubility in LLZO, $La_2Li_{0.5}Al_{0.5}O_4$ starts to form resulting in an increase of ZrO_2 content.

It can be inferred from the findings above that cubic phase stabilization was inhibited in case of $ZrO(NO_3)_2$ was used as Zr source after calcination at 1000 °C for 6 hours. To enlighten this, three types of mechanisms could be offered.

Firstly, Al containing impurity phases could give an idea. Using $ZrO(NO_3)_2$ as Zr source resulted in $LaAlO_3$ and $La_2Li_{0.5}Al_{0.5}O_4$. However, $LaAlO_3$ is the only Al containing impurity phase in case of using $ZrOCl_2$ as Zr source. It was believed that the high tendency to form wide variety of Al containing impurity phases inhibited the diffusion of more Al into LLZO lattice which inhibits cubic phase stabilization.

Secondly, a specific attention to the tetragonal and cubic $Li_7La_3Zr_2O_{12}$ (LLZO) structure must be paid for the purpose of explaining the cubic phase stabilization mechanism. Figure 7.4 visualizes the Zr-O bonds in both tetragonal and Zr coordinations along [100] direction built by using CrystalMaker.

Zr atoms locate only at (0,0,0) positions with four and six Zr-O bond numbers in tetragonal and cubic LLZO lattices, respectively. $ZrOCl_2$, Zr salt that has a high degree of dissociation (Zr^{4+}), could stabilize cubic LLZO phase having a more Zr-O bond in the presence of minimum 20 mole % Al after 1000 °C for 6 hours calcination conditions.

Thirdly, anion concentration within solution has a crucial effect on phase transformation. A study related on tetragonal-monoclinic transformation of solution based synthesized ZrO_2 claimed that $(NO_3)^-$ ions present in the solution inhibited the monoclinic to tetragonal transformation [98].

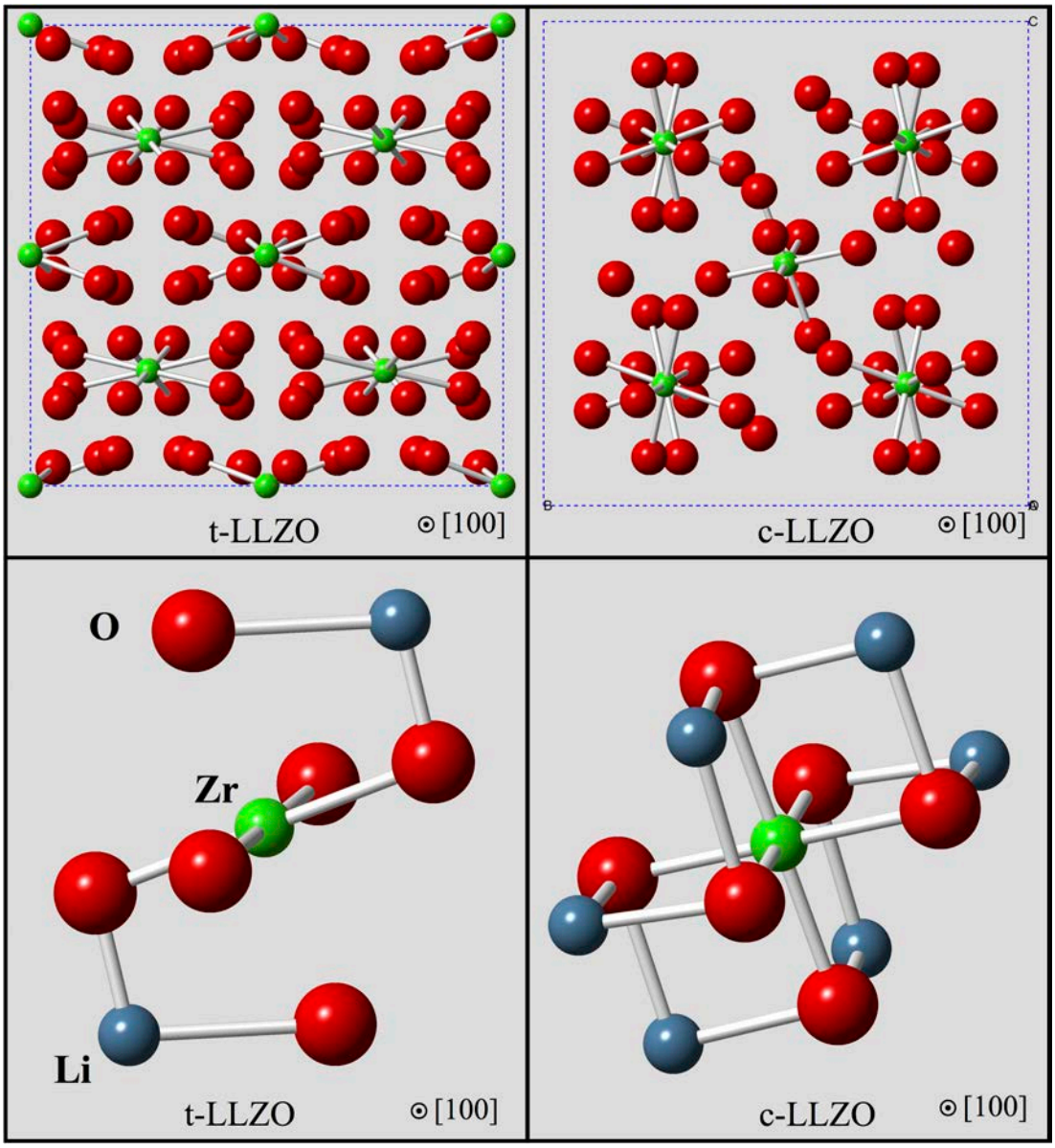

Figure 7.4. *Zr-O bonds in both tetragonal and cubic unit cell (upper side) and Zr coordinations (lower side) of tetragonal (t-LLZO) and cubic (c-LLZO) crystal structures along [100] direction.*

However, the study used $(NO_3)^-$ and Cl^- anions in different batches. The discussions on $(NO_3)^-$ and Cl^- containing mixed systems were inadequate.

In order to investigate the influence of $(NO_3)^-$ ion concentration in $(NO_3)^-$ and Cl^- containing mixed systems, the nitrate ion concentration for both precursors of $ZrOCl_2$ and $ZrO(NO_3)_2$ was kept constant by adding HNO_3 in $ZrOCl_2$ solution. In LLZO synthesis, 1 mole of 20 mole % Al containing $ZrO(NO_3)_2$ and $ZrOCl_2$ solution contains 21.05 and 17.05 moles of $(NO_3)^-$ ions in the solution, respectively. To subsidize nitrate ion deficit, an extra 4 mole of HNO_3, as $(NO_3)^-$ ion supply, per 1 mole LLZO were

added into the 20 mole % Al containing $ZrOCl_2$ system. pH value was also determined in the acidic region like those without HNO_3 addition. XRD pattern after the calcination at the same conditions (1000 °C for 6 hours) was given in Figure 7.5.

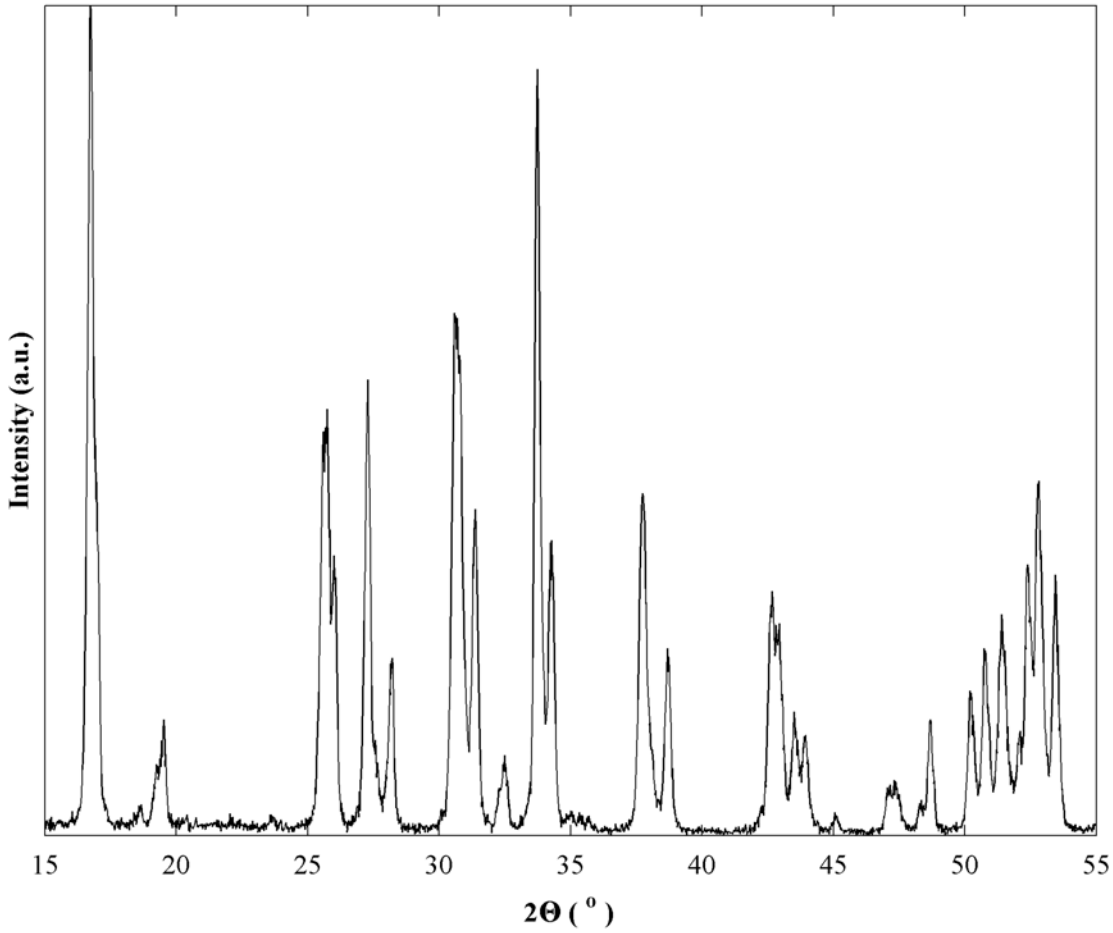

Figure 7.5. *The XRD pattern of 4 mole HNO3 per 1 mole LLZO added sample with the use of ZrOCl2 precursor when calcined at 1000 °C for 6 hours*

All the peaks in Figure 7.5 were attributed to tetragonal LLZO. In comparison to initial structure, which was cubic according to the XRD pattern given in Figure 7.2, results clearly indicated the inhibition effect of $(NO_3)^-$ ions on the formation and/or transformation from tetragonal to cubic phase.

In all, the presence of nitrate ions has a negative effect on the stabilization of cubic LLZO phase. When total nitrate ion concentration per 1 mole LLZO was set to 21.05, the tetragonal phase was stable after calcination at 1000 °C for 6 hours, no matter $ZrOCl_2$ or $ZrO(NO_3)_2$ was used as Zr source.

Considering anionic species, some anions could leave the system in a gaseous phase during calcination. For that purpose, identifying the gases, especially nitrogen containing gases, left during calcination was required in order to gain a full understanding on the role of nitrates during calcination.

The evolved gas analysis was conducted by using TGA-FTIR during calcination. Because of having both high nitrate ion and low impurity content, the sample obtained from $ZrO(NO_3)_2$ precursor having 30 % mole Al was selected and its IR spectrum as a function of time is given in Figure 7.6.

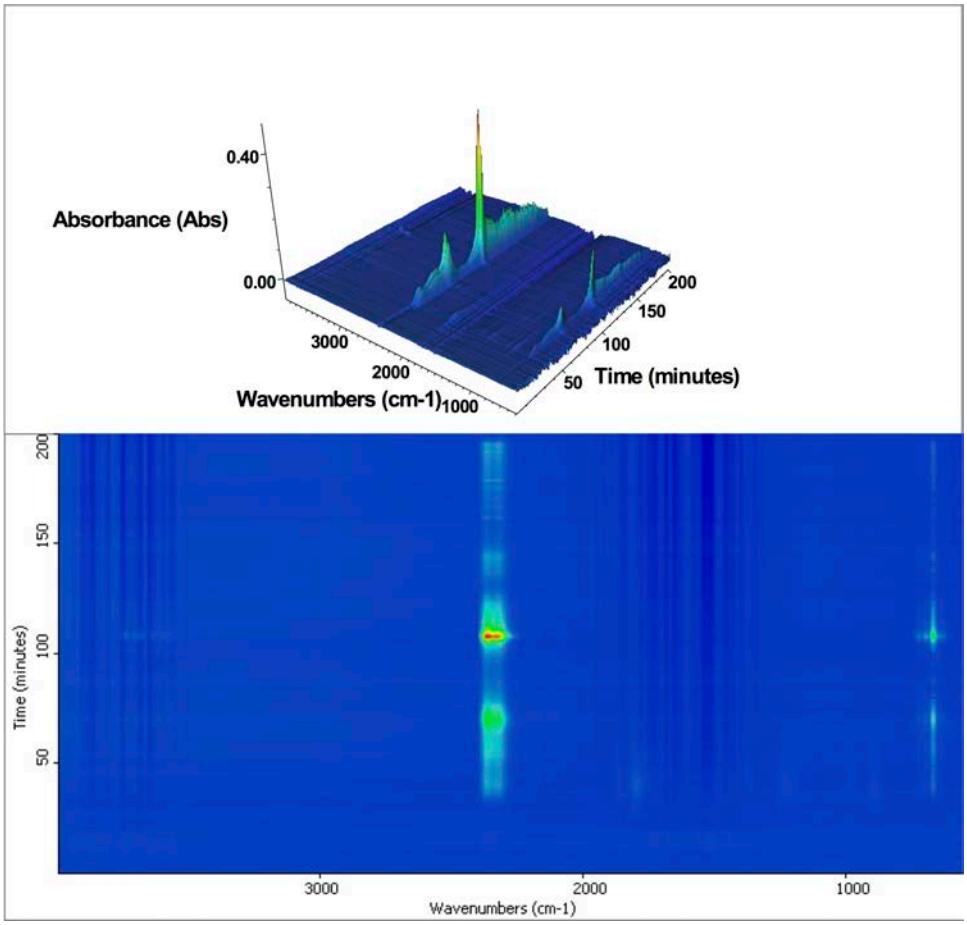

Figure 7.6. *TGA-FTIR analysis of evolved gases*

It can be deduced from the TGA-FTIR results that the highest absorbance value was 2360 cm^{-1} which belong to characteristic CO_2 spectrum. The data depicted in Figure 7.7 (a) showed the temperature distribution of the gaseous CO_2 obtained from its 2360 cm^{-1} peak. There was a stepwise release of CO_2 during calcination. The first four releases at 204, 287, 346 and 538 °C were attributed to the burning of residual organic components in the dried powder.

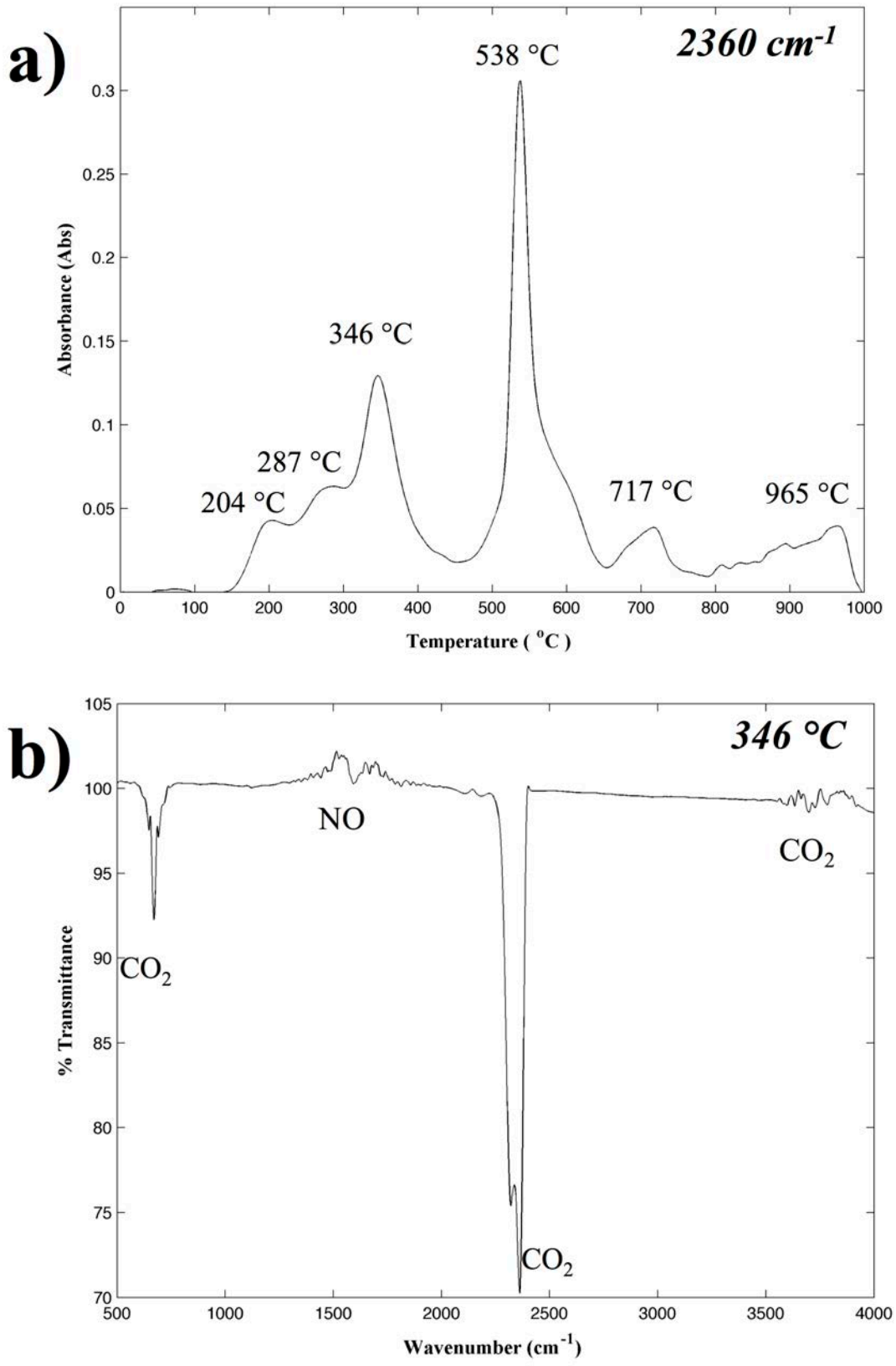

Figure 7.7. *Evolved gas analysis from TGA-FTIR: a) temperature distribution of CO_2 release based on 2360 cm^{-1} b) IR spectrum at 346 °C and c) at 538 °C*

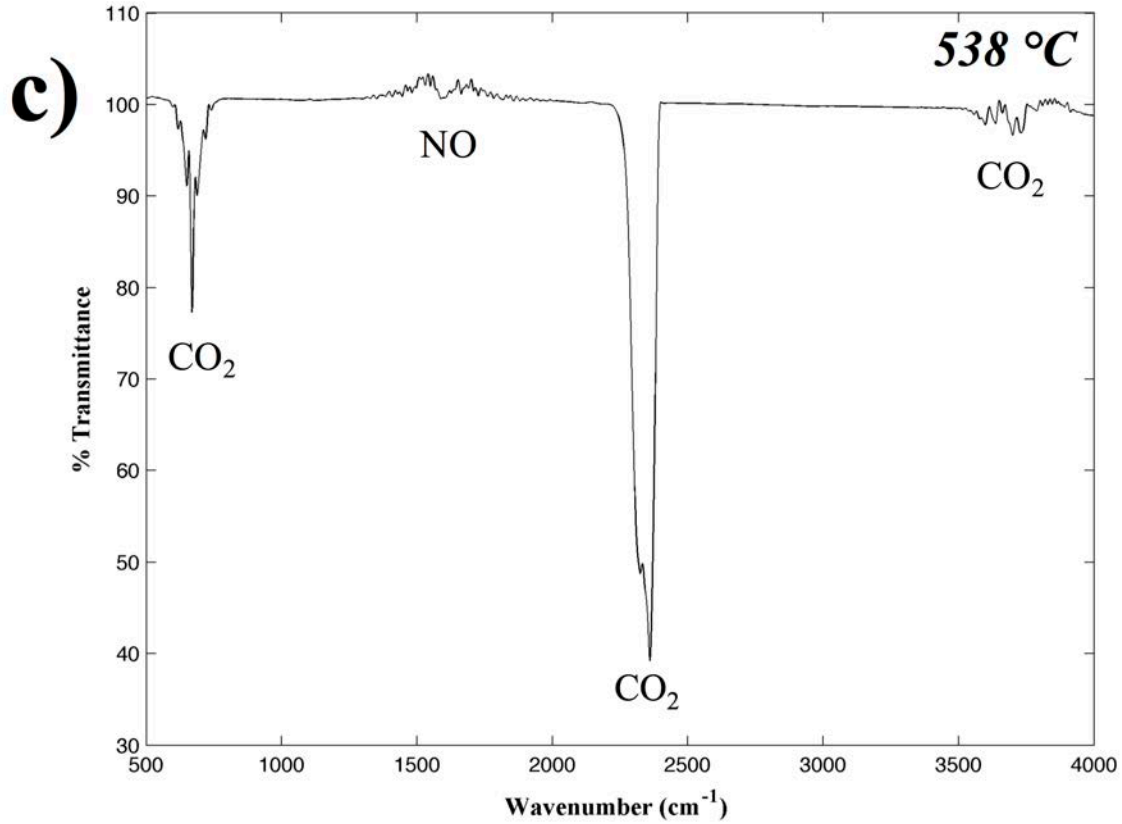

Figure 7.7. (continued) *Evolved gas analysis from TGA-FTIR: a) temperature distribution of CO_2 release based on 2360 cm^{-1} b) IR spectrum at 346 °C and c) at 538 °C*

However, the remaining CO_2 releases especially at 717 and 965 °C were due to thermal decomposition of metal carbonates present in the solution. CO_2 was released until 1000 °C during calcination. In Figure 7.7 (b) and (c), the IR spectra of gaseous releases at the temperatures of 346 and 538 °C, the highest two absorbance obtained, were evaluated. All the peaks were indexed as mostly CO_2. Nitric Oxide (NO) was also identified. Relatively small peaks of gaseous NO were due to the highly extensive CO_2 exhaust during calcination. To sum up the findings related to evolved gas analysis, carbon and nitrogen residuals left the system in the form of gaseous CO_2 and NO.

Microstructural analysis was performed on powders synthesized by using $ZrOCl_2$ precursor containing different amount of Al and given in Figure 7.8.

Particles in the sample synthesized without Al addition showed the least necking behavior than the others. Besides, micron size porosities were found in the microstructure. When Al content was increased to 20 mole %, necking was also increased. This is indicating that better sinterability behavior can be expected.

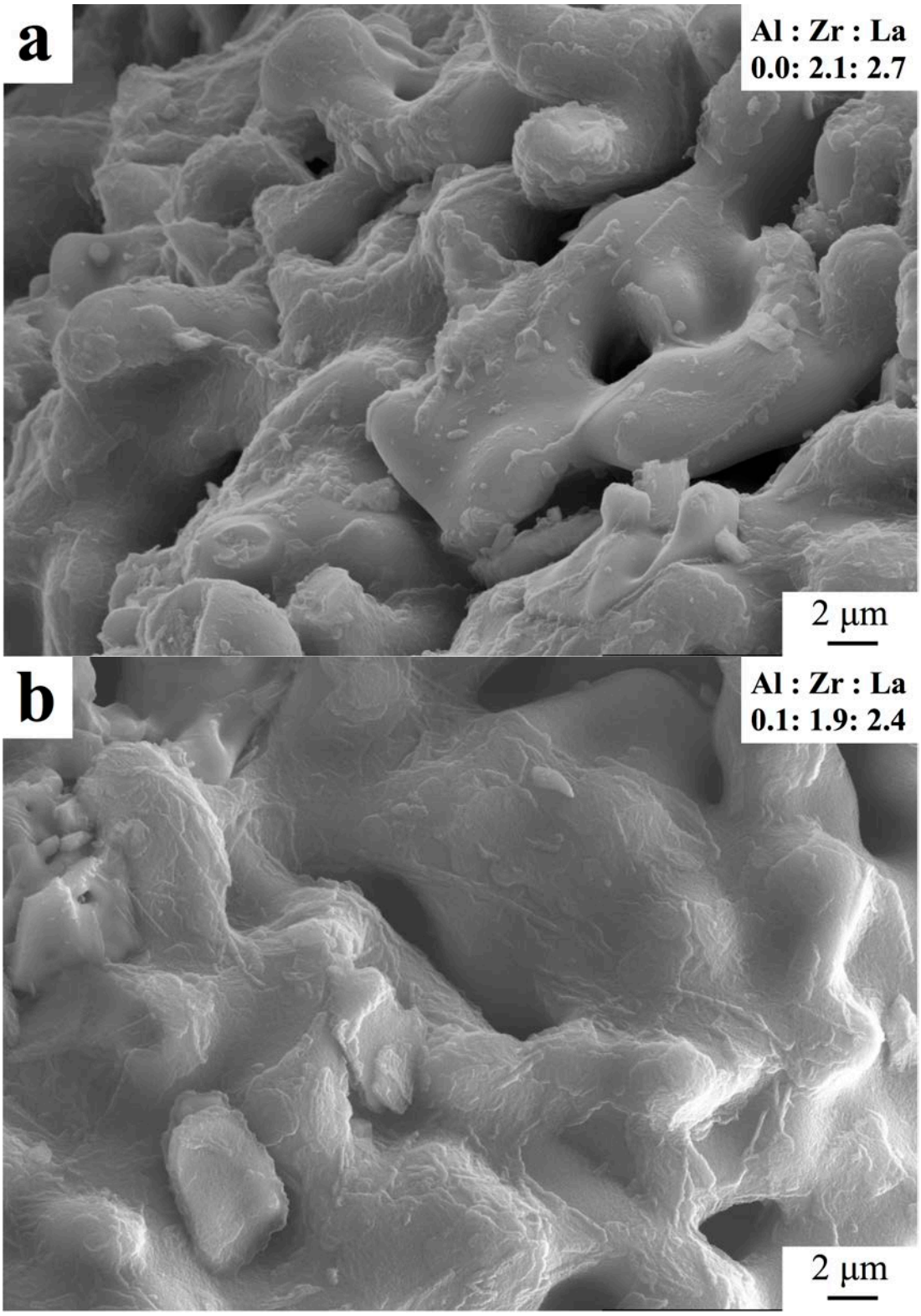

Figure 7.8. *SEM images of powders synthesized by ZrOCl2 precursor: a) without Al addition, b) 10, c) 20, d) 30 and e) 40 mole % Al containing LLZO compositions after calcination at 1000 °C for 6 hours.*

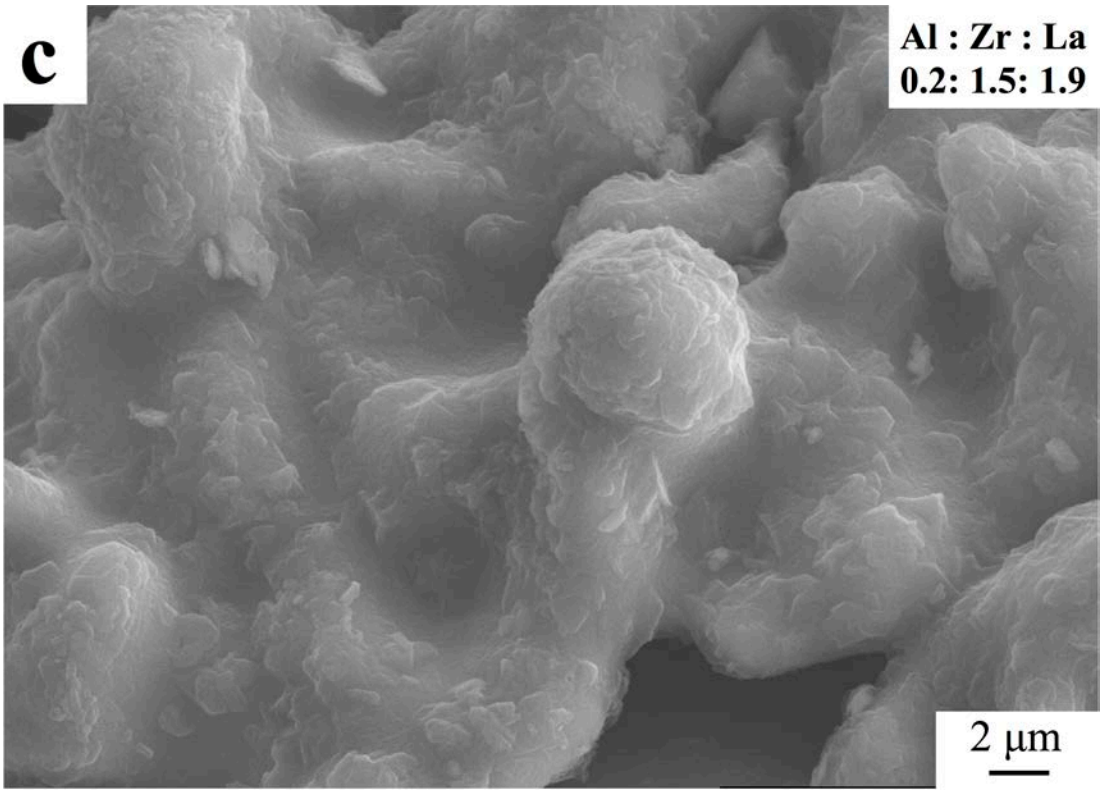

Figure 7.8. (continued) *SEM images of powders synthesized by $ZrOCl_2$ precursor: a) without Al addition, b) 10, c) 20, d) 30 and e) 40 mole % Al containing LLZO compositions after calcination at 1000 °C for 6 hours.*

On the other hand, primary particles were hardly seen for 20 mole % Al content (Figure 7.8 (c)). In the case of 30 mole % Al addition (Figure 7.8 (d)), both submicron and a few micron sized cube shaped $LaAlO_3$ crystals (according to EDS point analysis) were observed. Finally, in the 40 mole % Al containing LLZO powders, more and much bigger size of such crystals were observed (Figure 7.8 (e)).

Effect of Al amount on the performance of cubic stabilized LLZO phase was evaluated by using AC Impedance Method. Figure 7.9 showed the Nyquist plots of 20, 30 and 40 mole % Al containing LLZO pellets obtained through the use of $ZrOCl_2$.

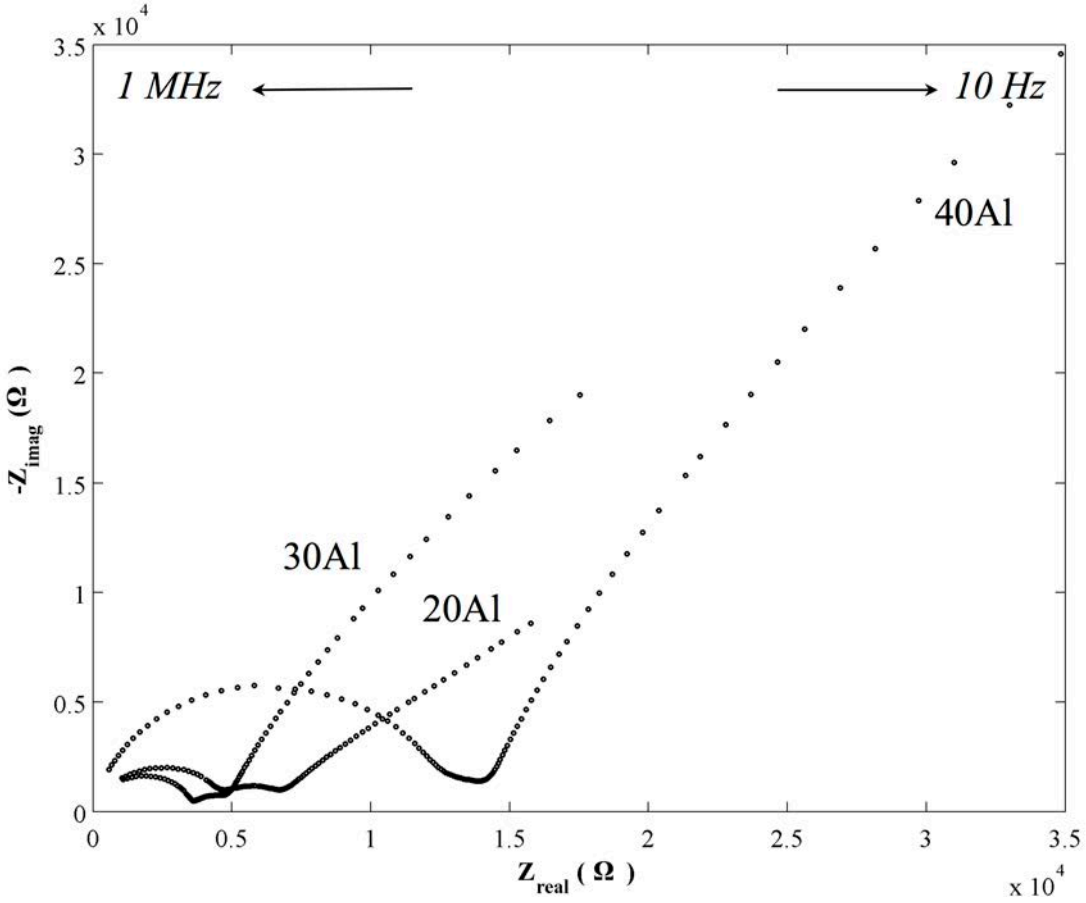

Figure 7.9. *Nyquist plots of 20, 30 and 40 mole % Al stabilized cubic LLZO (20Al: 20-$ZrOCl_2$; 30Al: 30-$ZrOCl_2$; 40Al: 40-$ZrOCl_2$)*

According to Figure 7.9, there were semicircles and linear-like tails. High-frequency semicircles were formed because of ionic resistance (R_i) contribution and lower frequency semicircles were formed due to the grain boundary resistance (R_{gb}). Total resistance is determined by the sum of both ionic and grain boundary resistance. A linear-like inclined tails were thought to be formed due to the presence of Li-ion blocking Au-Pd electrodes. The observed low-frequency tail corresponds to the impedance barrier to charge transfer between LLZO and Au-Pd Li-ion blocking electrodes [99]. Ionic resistance was decreased when the Al content was increased to 30 mole %, whereas ionic resistance was dramatically decreased for the sample containing 40 mole % Al which is due to the fact that maximum solubility limit of Al in cubic LLZO phase was exceeded. In all cases, total resistances were dominated by the ionic resistance. The highest ionic conductivity was obtained from 30 mole % Al containing sample.

Ionic conductivities (δ) can be calculated by using the ionic resistance (R_i) values and geometrical factors according to the equation given below:

$$\sigma = \frac{L}{R \times A} \tag{7.3}$$

where L and A are the thickness and surface area of the pellet respectively. The results calculated by using Equation (7.3) are presented in Table 7.1.

Table 7.1. *Calculated ionic conductivities of 20 - 40 mole % Al containing cubic LLZO powders*

Al Content (%)	Ionic Conductivity (mS/cm)
20	0.031
30	0.040
40	0.012

Ionic conductivities were calculated as 0.04 to 0.031 and 0.012 mS/cm for 20, 30 and 40 mole % Al content, respectively. The highest ionic conductivity (0.04 mS/cm) were determined on 30 % Al containing sample which was calcined at 1000 °C for 6 hours (Table 7.1).

It can be concluded that a slight increase on remnant Li_2ZrO_3 and $La_2Zr_2O_7$ phases in LLZO does not have a crucial influence on ionic conductivity of 20 and 30 mole % Al containing LLZO whereas the presence of $LaAlO_3$ that forms when the maximum solubility of Al in cubic LLZO structure exceeds, ionic conductivity decreases. $LaAlO_3$'s mixed type of electron-ion conductance mechanism is believed to the reason of such behavior [100].

Table 7.2 showed a brief overview on the electrochemical performance of LLZO samples synthesized via two different synthesis methods, solid-state reaction and citrate-nitrate methods.

Table 7.2. *Comparison of 30 mole % Al containing LLZO samples synthesized via different methods*

Synthesis Method	**Sintering Conditions**	**Impurity**	**Crystal Structure**	**Bulk Conductivity (mS/cm)**
Solid-State	1100 °C – 12h	-	T+C	0.072
Citrate-Nitrate	1100 °C – 12h	Li_2ZrO_3	C	0.040

It can be inferred from the Table 7.2 that the bulk conductivity of the solid-state reaction synthesized LLZO has improved bulk conductivity even if a mixture of poor conductive tetragonal and high conductive cubic LLZO phase presents. It should also be noted that Li_2ZrO_3 impurities present in LLZO samples synthesized via Citrate-Nitrate route. However, as explained in Section 7.3.1, Li_2ZrO_3 impurities do not have any crucial effect on bulk conductivity. Such a big difference on bulk conductivity can be attributed to the different densification behavior of LLZO samples synthesized via solid-state reaction and Citrate-Nitrate methods. For the purpose of assessing the densification behavior of LLZO samples synthesized via two different methods, optical dilatometer analysis was conducted and a shrinkage plot as a function of temperature were depicted in Figure 7.10.

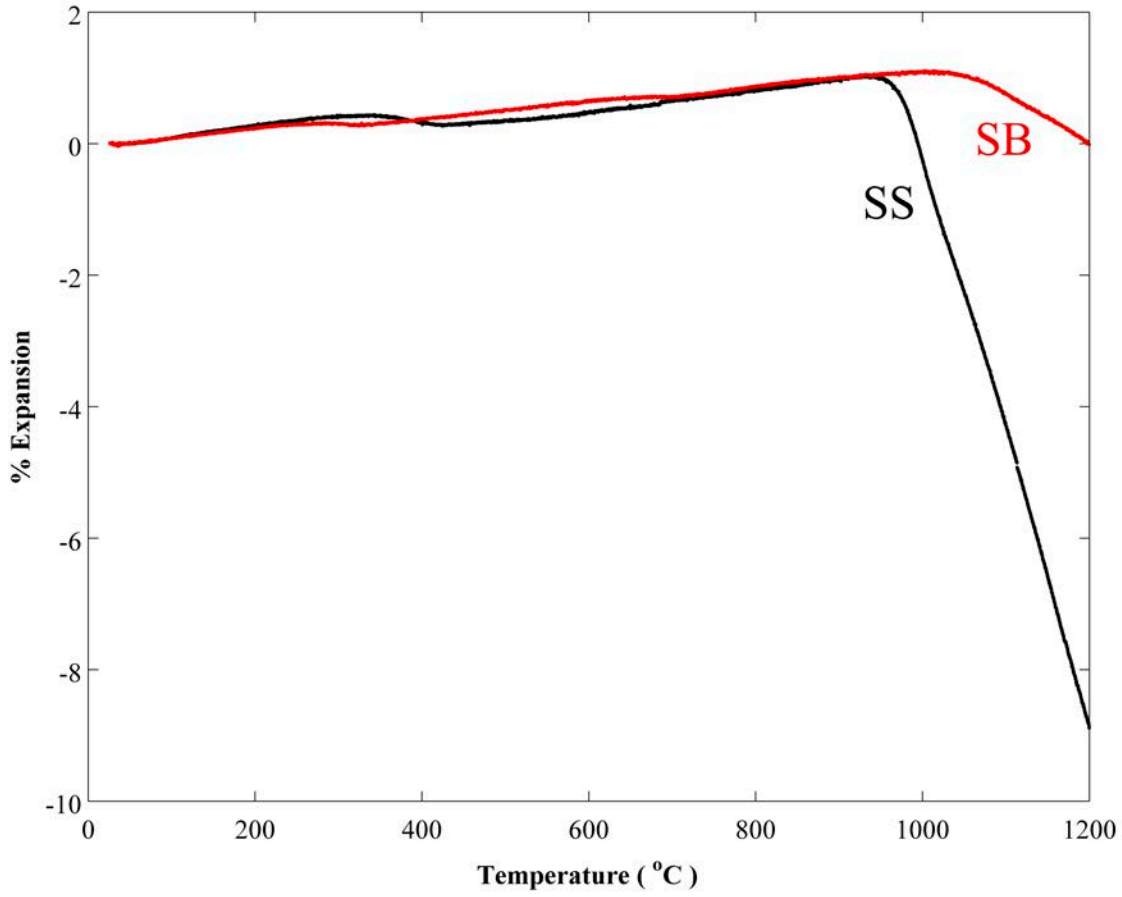

Figure 7.10. *Dilatometer curve of LLZO samples synthesized via solid-state and Citrate-Nitrate methods*

The ΔH-mix powders after 1000 °C – 6h calcination discussed in Section 3 were used to determine the densification behavior of Solid-State (denoted as SS) synthesized

tetragonal LLZO samples. Besides, powders after calcination at 1000 °C for 6h discussed in Section 7 were also used as Citrate-Nitrate synthesized cubic stabilized LLZO samples (denoted as CN). 30 mole % Al content was kept constant. According to the dilatometer curves of solid-state and Citrate-Nitrate synthesized LLZO samples, densification started earlier and rapidly reached 8.8 % shrinkage until 1200 °C for solid-state reaction synthesized LLZO samples. In case of Citrate-Nitrate synthesized LLZO, which has fully cubic crystal structure, a negligible amount of shrinkage was observed. Both LLZO samples were sintered at 1100 °C for 12 hours and their measured Archimedes densities were determined as 4.75 g/cm^3 for solid-state reaction and 3.62 g/cm^3 for Citrate-Nitrate method.

It can be concluded that starting from tetragonal LLZO powders, highly shrank dense sintered bodies can be obtained. Since porosities are unable to conduct any ionic species, denser sintered bodies can reach higher bulk conductivities, as it's shown in Table 7.2.

7.3.2. A modified Citrate-Nitrate method for $Li_7La_3Zr_2O_{12}$ synthesis

In Section 7.3.1, the negative effect of $(NO_3)^-$ ions during solution-based synthesis of LLZO was discussed. For the purpose of reducing total $(NO_3)^-$ ion, all of the precursors used so far and their contribution to total $(NO_3)^-$ ions were calculated in Table 7.3.

Table 7.3. *Nitrate ion contribution of each precursor used for solution-based LLZO synthesis*

	$ZrO(NO_3)_2$ Precursor	**$ZrOCl_2$ Precursor**
$LiNO_3$	8.05	8.05
$La(NO_3)_3$	9	9
$ZrO(NO_3)_2$	4	-
$ZrOCl_2$	-	-
$Al(NO_3)_3$	0.9	0.9
Total $(NO_3)^-$ ions	21.05 mole	17.05 mole
Crystal Structure	Tetragonal	Cubic

According to Table 7.3, the highest $(NO_3)^-$ ions came from $La(NO_3)_3$. The possible usage of La_2O_3 in solution-based synthesis of LLZO has a drawback. La_2O_3 was known as an insoluble Lanthanum compound in neutral and/or slightly acidic and soluble in acidic solutions. Since it could not be obtained sufficient acidic environment during the flowchart given in Figure 7.1, replacing La_2O_3 instead of $La(NO_3)_3$ as a

Lanthanum source requires a modification in the synthesis procedure. Figure 7.11 represented the modified flowchart of solution-based LLZO synthesis by using La_2O_3 as a Lanthanum source.

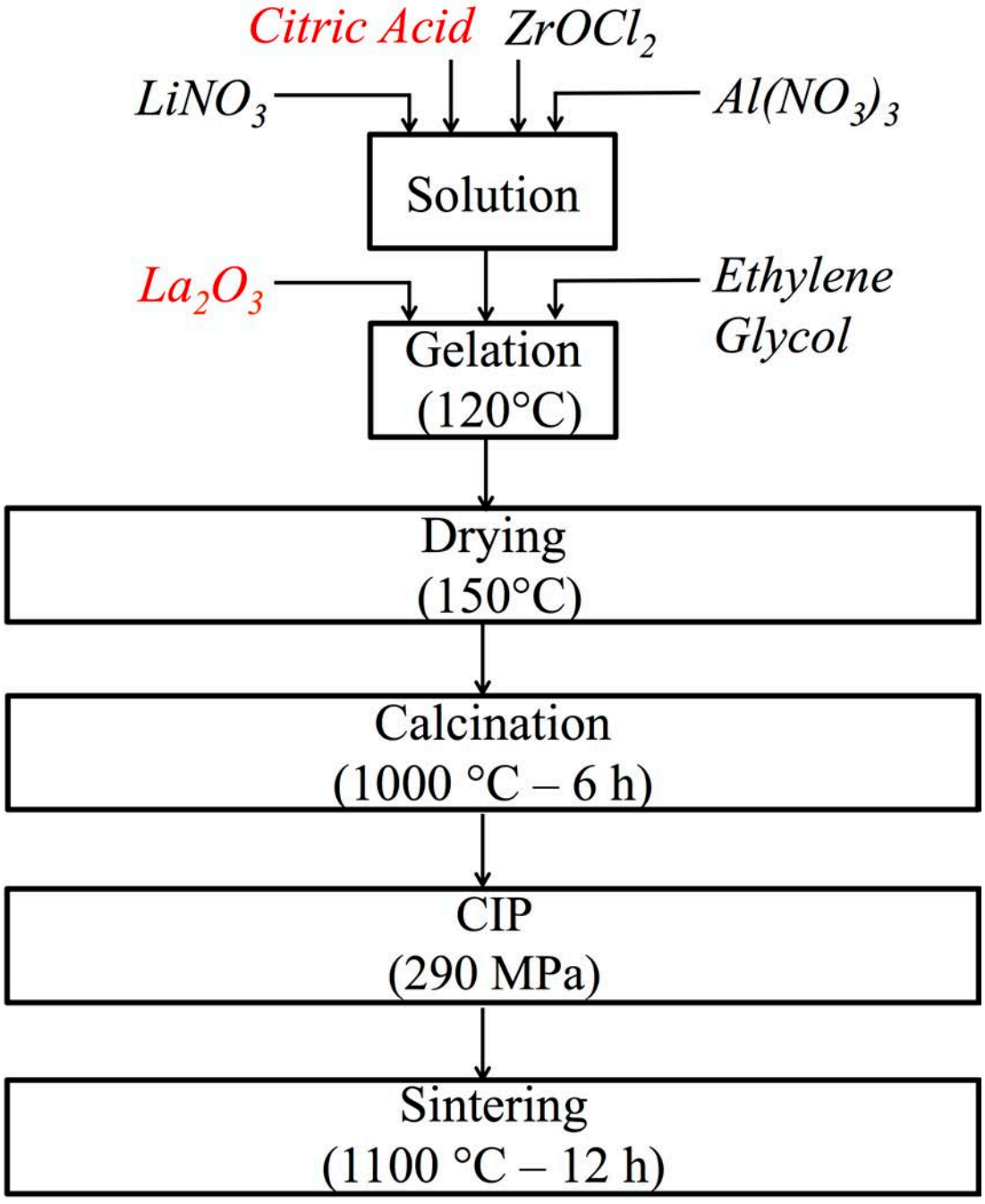

Figure 7.11. *Modified flowchart of solution-based LLZO synthesis by using La_2O_3 as a La source*

Figure 7.12 showed the XRD patterns of calcined powders at a lower calcination temperature between 700 and 800 °C by using Lanthanum nitrate and Lanthanum oxide

precursors for 6 hours. It can be obtained from the Figure 7.12 that all the patterns were dominated by cubic LLZO phase. Since no sign of tetragonal was observed, it can be concluded that tetragonal to cubic transformation due to heat treatment was not the case for Citrate-Nitrate synthesis. The common impurity phases obtained was $LaAlO_3$, $La_2Zr_2O_7$, Li_2ZrO_3 and Li_2CO_3.

Table 7.4 presented the quantitative analysis obtained from Reference Intensity Reduced (RIR) Method.

Table 7.4. *Quantitave analysis of Citrate-Nitrate synthesized LLZO by using RIR Method*

	$La(NO_3)_3$			**La_2O_3**		
	700 °C (%)	**750 °C (%)**	**800 °C (%)**	**700 °C (%)**	**750 °C (%)**	**800 °C (%)**
c-$Li_7La_3Zr_2O_{12}$	56.1	83.3	88.2	91	92.5	96
$LaAlO_3$	3.7	4.8	4.0	1.4	1.5	0.5
Li_2ZrO_3	2.7	2.0	2.8	0.7	1.9	0.7
$La_2Zr_2O_7$	16.1	4.7	5.0	2.2	0.9	3.4
Li_2CO_3	21.4	5.2	0.0	4.7	3.2	2.7

It was apparent that using La_2O_3 instead of $La(NO_3)_3$ resulted with a huge increase on cubic LLZO amount. When $La(NO_3)_3$ was used, the amount of cubic LLZO phase was increased from 56.1 % to 88.2 % and unreacted Li_2CO_3 was disappeared at 800 °C calcination temperature. With increasing calcination temperature to 800 °C, dramatically changes were observed from $La_2Zr_2O_7$ and Li_2CO_3. $La_2Zr_2O_7$ was decreased from 16.1 % to 5.0 % and the amount of Li was also decreased from 21.4 % and disappeared.

7.4. Conclusion

To conclude all the findings above, two different Zr sources $ZrO(NO_3)_2$ and $ZrOCl_2$ that has a different degree of dissociation were used in citrate-nitrate method with 0-40 mole % Al addition. Cubic phase stabilization after calcination at 1000 °C for 6 hours can only occur when $ZrOCl_2$ was used where Zr^{4+} cations were present in the solution and no phase transformation took place when $ZrO(NO_3)_2$ was used where ZrO^{2+} ions were present at calcination conditions of 1000 °C – 6 hours.

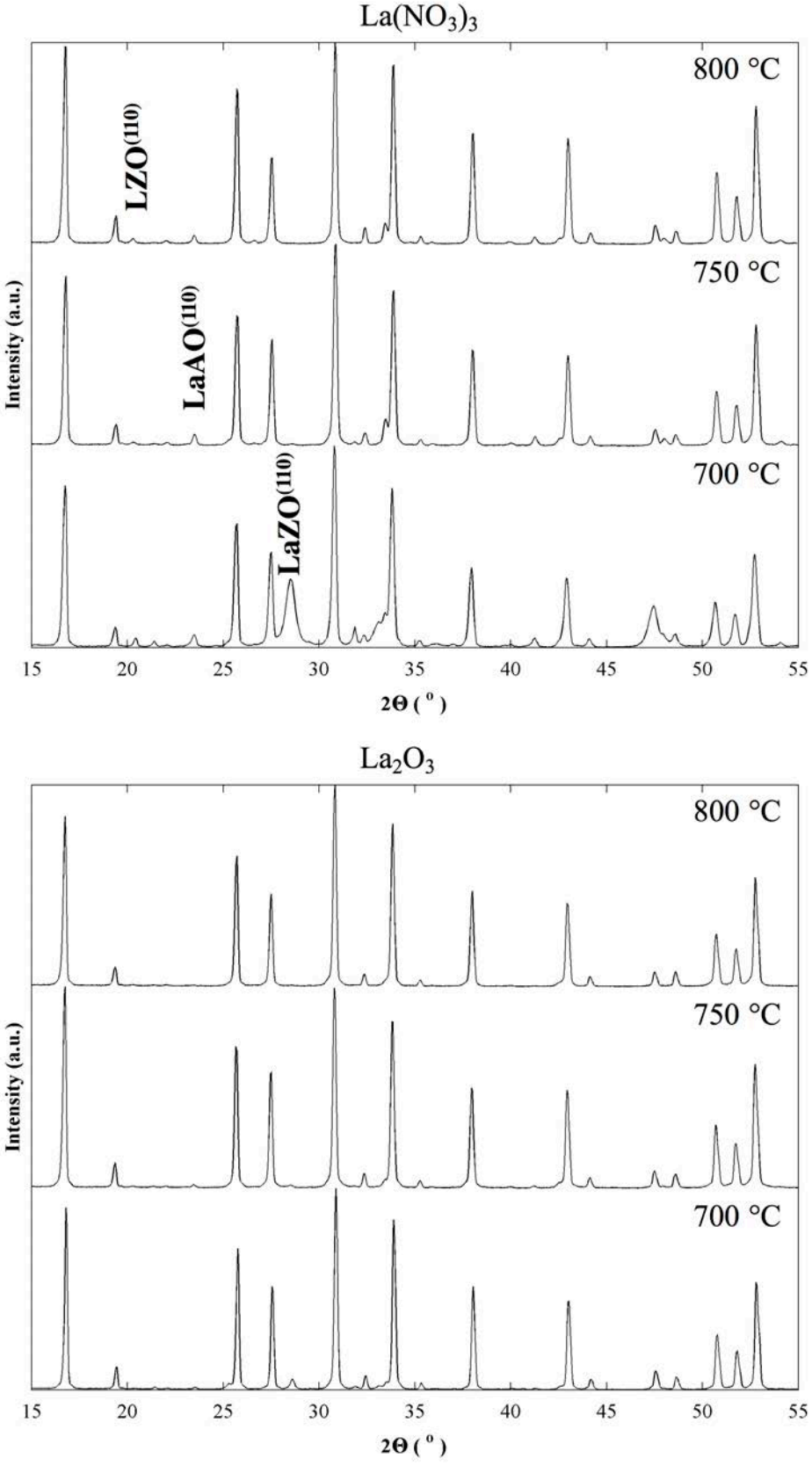

Figure 7.12. *XRD patterns of calcined powders by using $La(NO_3)_3$ and La_2O_3 precursors between 700-800 °C calcination temperature for 6 hours*

Tetragonal LLZO with various amounts of Li_2CO_3, La_2O_3, ZrO_2, $LaAlO_3$, $La_2Zr_2O_7$ and $La_2Li_{0.5}Al_{0.5}O_4$ impurities were seen for all different Al contents when $ZrO(NO_3)_2$ used as a Zr precursor. However, the use of $ZrOCl_2$, resulted in the formation of much less impurities of ZrO_2, Li_2ZrO_3 and $LaAlO_3$ in comparison to $ZrO(NO_3)_2$.

Tetragonal to cubic phase transformation were discussed in terms of Al containing impurity phases, different dissociation behavior of $ZrOCl_2$ and $ZrO(NO_3)_2$ and existances of anions within the solution. Using $ZrO(NO_3)_2$, as a Zr source lead to form more Al containing impurity phases that prevents Al to incorporate within LLZO structure inhibiting formation of cubic phase and/or the tetragonal to cubic phase transformation. Zr atoms can locate (0,0,0) positions in both tetragonal and cubic LLZO phase but it has different bonding numbers. Zr can bind 4 and 6 oxygen atoms in tetragonal and cubic LLZO structure, respectively. So, high bonding capability of Zr^{4+} ions, formed in $ZrOCl_2$ systems, has a tendency to form more Zr-O bond containing cubic structure. The nitrate ions in solution inhibit the tetragonal-cubic phase transformation and when total nitrate ion was increased from 17.05 to 21.05 mole per 1 mole of LLZO in $ZrOCl_2$ system, cubic LLZO phase was not obtained even in cubic phase forming $ZrOCl_2$ precursor and undesirable tetragonal LLZO phase was formed.

Besides, according to the TGA-FTIR evolved gas analysis, CO_2 was extensively exhausted along with relatively lower NO gases. By using $ZrOCl_2$ as a Zr precursor, Al addition increases interparticular necking to have a better sinterability of powders. Cube shaped $LaAlO_3$ crystals were become apparent starting from 30 mole % Al addition. Impedance measurements on various Al participated LLZO shows that $LaAlO_3$ impurities have more influence on decreasing the ionic conductivity than Li_2ZrO_3 or $La_2Zr_2O_7$.

Dilatometer measurements stated that more dense sintered pellets in terms of both shrinkage and Archimedes density could be obtained when starting powders were in the form of tetragonal LLZO.

8. CONCLUSION & FUTURE REMARKS

In this study, two different synthesis methods and performance comparison of solid-state reaction and Citrate-Nitrate synthesized $Li_7La_3Zr_2O_{12}$ was covered. Since solid-state reaction is based on milling and particle size reduction of precursor powders, the method is an example of top-down material synthesis. On the other hand, Citrate-Nitrate method is also known as bottom-up type of material synthesis. In this regard, this study also compares the pros and cons of two different approaches in case of LLZO synthesis.

First of all, with extensive use of thermal analysis and thermodynamic calculations, solid-state LLZO synthesis parameters are optimized in terms heat-treatment steps, heating rate and precursor types. Results indicated that 2-step calcination does not have any influence on the purity of the calcined powders and can be minimized to the one single calcination step. Lower heating rates can facilitate impurity and/or intermediate phase formation after calcination. Thus, higher heating rate such as 10 °C/min results in reduced amount of impurity phases. The total heat treatment time is greatly reduced after such modifications. Since tetragonal to cubic phase transformation is time-requiring process, the obtained phase is determined as tetragonal LLZO when shorter calcination times were used. After that, the effect of starting powders are discussed by using the optimized parameters. Oxide formation reactions of various Li, La and Al precursors that have been used during LLZO synthesis are compared in terms of Gibbs Free Energy change and Enthalpy change. Results showed that bulk conductivities were higher when the oxides of both La and Al are used rather than their hydroxides.

A new tool, radial shrinkage, is introduced for the densification assessments of LLZO pellets. Archimedes method, the widely used density measurement method used for densification assessments of LLZO, is not appropriate tool since typical microstructure of LLZO consists of many porosities within grains and Archimedes method is unable to detect them. The findings point out even if the measured Archimedes density stays stable with increasing temperature, pellet keeps on densification because radial shrinkage continues increasing. In this regard, a novel densification model is offered according to the microstructural changes at different sintering temperatures. With increasing sintering temperature, closed porosities are combined with each other to form bigger closed porosities. At some point, when pores

are combined in a 3D order, a smaller grain is ruptured from the bigger grain and the amount of open porosities that can be measured by Archimedes density is increased.

The dissertation also brings a novel understanding on Lithium detection and suitability of Xe ions in the field of Li containing materials in electron microscopy. Excavation from the deliberately prepared Li-rich impurity containing LLZO sample with Xenon ion enables to collect Lithium at a high yield with ToF-SIMS attachment in FIB-SEM systems. Elemental maps reveal approximately same resolution of Li when compared with Al maps.

Since ToF-SIMS attached FIB-SEM allows separation of atoms and collection at the same time, it is considered as a versatile method for near surface analysis. In this regard, the air stability of as-synthesized LLZO pellets were also studied. Results emphasized the Lanthanum stability on the aged LLZO structure but Lithium and Zirconium instability since LiF, LiOH and Li_2ZrO_3 are seen according to the positive and negative mass spectra obtained from ToF-SIMS on the aged LLZO surface.

In Citrate-Nitrate synthesis of LLZO, two common Zirconium sources which are having a different dissociation behavior on the tetragonal to cubic phase transformation of LLZO is covered. $ZrOCl_2$ which dissolves by producing Zr^{4+} ions stabilizes cubic LLZO phase with a minimum of 20 mole % Al addition whereas $ZrO(NO_3)_2$, which dissolves by producing ZrO^{2+} ions, produces tetragonal LLZO at all Al addition up to 40 mole % and unable to stabilize cubic LLZO phase at 1000 °C – 6h calcination condition. The higher bonding ability of $ZrOCl_2$ and lower overall $(NO_3)^{2-}$ ion concentration is found as the main reason underlying the cubic phase transformation. The negative influence of nitrate ions in the solution on cubic phase stabilization is also discussed.

In this study, the performance of the LLZO synthesized with two different approaches (solid-state reaction and Citrate-Nitrate) was compared. However, the bulk conductivities were significantly different. The LLZO sample synthesized by using Citrate-Nitrate method shows relatively low conductivity. The reason is found as the huge shrinkage difference obtained from optical dilatometer between powders calcined with two different methods. Starting from tetragonal LLZO phase, a higher shrinkage results in denser microstructure having improved bulk conductivity. On this subject, Citrate-Nitrate method is suitable only if LLZO is used in a powder form. When LLZO

solid electrolytes must be used in a bulk form, solid-state synthesis of LLZO should be preferred.

Undoubtedly, ionic conductivity is insufficient for evaluating the battery performance. There should be several crucial points scientists need to pay attention. First of all, the interfacial resistance between electrodes and LLZO solid electrolyte should be lowered.

Stability of the Lithium should also be assessed. Li/LLZO/Li symmetric cell assembly could give an idea about the Li dendrite suppression. During cycling of Li/LLZO/Li, there is a specified time passed to short-circuit the cell. This time determines the Lithium stability. In order to prevent the potential short-circuit, the time passed until short-circuit should be as long as possible. The preliminary works on symmetric cell assembly showed insufficient isolation since metallic Lithium is degraded and oxidized in air atmosphere of the assembled battery prototype.

The Lithium wettability is also an important factor to reduce interfacial resistance of an all-solid-state Li-ion battery and should be lowered as low as possible. A very thin layer of the coatings that enhance wettability of LLZO with various deposition techniques such as ALD needs to be carried out.

REFERENCES

[1] Bruce, P.G., *Energy storage beyond the horizon: Rechargeable lithium batteries.* Solid State Ionics, 2008. **179**(21-26): p. 752-760.

[2] Arthur, T.S., Bates, D.J., Cirigliano, N., Johnson, D.C., Malati, P., Mosby, J.M., Perre, E., Rawls, M.T., Prieto, A.L., and Dunn, B., *Three-dimensional electrodes and battery architectures.* MRS Bulletin, 2011. **36**(07): p. 523-531.

[3] Scrosati, B. and Garche, J., *Lithium batteries: Status, prospects and future.* Journal of Power Sources, 2010. **195**(9): p. 2419-2430.

[4] Tietz, F., Wegener, T., Gerhards, M.T., Giarola, M., and Mariotto, G., *Synthesis and Raman micro-spectroscopy investigation of $Li_7La_3Zr_2O_{12}$.* Solid State Ionics, 2013. **230**(0): p. 77-82.

[5] R. M., D.D.A.J.R., *Understanding Batteries*. 2001: RSC Paperbacks.

[6] Aifantis, K.E. and Hackney, S.A., *Current and Potential Applications of Secondary Li Batteries*, in *High Energy Density Lithium Batteries*. 2010, Wiley-VCH Verlag GmbH & Co. KGaA. p. 81-101.

[7] Tarascon, J.M. and Armand, M., *Issues and challenges facing rechargeable lithium batteries.* Nature, 2001. **414**(6861): p. 359-67.

[8] Delaizir, G., Viallet, V., Aboulaich, A., Bouchet, R., Tortet, L., Seznec, V., Morcrette, M., Tarascon, J.-M., Rozier, P., and Dollé, M., *The Stone Age Revisited: Building a Monolithic Inorganic Lithium-Ion Battery*. Advanced Functional Materials, 2012. **22**(10): p. 2140-2147.

[9] Wang, Y., Li, B., Ji, J., Eyler, A., and Zhong, W.-H., *A Gum-Like Electrolyte: Safety of a Solid, Performance of a Liquid.* Advanced Energy Materials, 2013. **3**(12): p. 1557-1562.

[10] Park, M., Zhang, X., Chung, M., Less, G.B., and Sastry, A.M., *A review of conduction phenomena in Li-ion batteries.* Journal of Power Sources, 2010. **195**(24): p. 7904-7929.

[11] Huggins, R., *Advanced batteries: materials science aspects*. 2008: Springer.

[12] Knauth, P., *Inorganic solid Li ion conductors: An overview.* Solid State Ionics, 2009. **180**(14-16): p. 911-916.

[13] Nazri, G.-A. and Pistoia, G., *Lithium batteries: science and technology*. 2008: Springer Science & Business.

[14] Yao, X.Y., Huang, B.X., Yin, J.Y., Peng, G., Huang, Z., Gao, C., Liu, D., and Xu, X.X., *All-solid-state lithium batteries with inorganic solid electrolytes: Review of fundamental science.* Chinese Physics B, 2016. **25**(1).

[15] Lobe, S., Dellen, C., Finsterbusch, M., Gehrke, H.G., Sebold, D., Tsai, C.L., Uhlenbruck, S., and Guillon, O., *Radio frequency magnetron sputtering of $Li_7La_3Zr_2O_{12}$ thin films for solid-state batteries.* Journal of Power Sources, 2016. **307**: p. 684-689.

[16] Park, J.S., Cheng, L., Zorba, V., Mehta, A., Cabana, J., Chen, G.Y., Doeff, M.M., Richardson, T.J., Park, J.H., Son, J.W., and Hong, W.S., *Effects of crystallinity and impurities on the electrical conductivity of Li-La-Zr-O thin films.* Thin Solid Films, 2015. **576**: p. 55-60.

[17] Sharafi, A., Kazyak, E., Davis, A.L., Yu, S.H., Thompson, T., Siegel, D.J., Dasgupta, N.P., and Sakamoto, J., *Surface Chemistry Mechanism of Ultra-Low Interfacial Resistance in the Solid-State Electrolyte $Li_7La_3Zr_2O_{12}$.* Chemistry of Materials, 2017. **29**(18): p. 7961-7968.

[18] Shao, Y.J., Wang, H.C., Gong, Z.L., Wang, D.W., Zheng, B.Z., Zhu, J.P., Lu, Y.X., Hu, Y.S., Guo, X.X., Li, H., Huang, X.J., Yang, Y., Nan, C.W., and Chen, L.Q., *Drawing a Soft Interface: An Effective Interfacial Modification Strategy for Garnet Type Solid-State Li Batteries.* Acs Energy Letters, 2018. **3**(6): p. 1212-1218.

[19] Gao, Z.H., Sun, H.B., Fu, L., Ye, F.L., Zhang, Y., Luo, W., and Huang, Y.H., *Promises, Challenges, and Recent Progress of Inorganic Solid-State Electrolytes for All-Solid-State Lithium Batteries.* Advanced Materials, 2018. **30**(17).

[20] Thangadurai, V., Narayanan, S., and Pinzaru, D., *Garnet-type solid-state fast Li ion conductors for Li batteries: critical review.* Chem Soc Rev, 2014. **43**(13): p. 4714-27.

[21] Cheng, L., Crumlin, E.J., Chen, W., Qiao, R.M., Hou, H.M., Lux, S.F., Zorba, V., Russo, R., Kostecki, R., Liu, Z., Persson, K., Yang, W.L., Cabana, J., Richardson, T., Chen, G.Y., and Doeff, M., *The origin of high electrolyte-electrode interfacial resistances in lithium cells containing garnet type solid electrolytes.* Physical Chemistry Chemical Physics, 2014. **16**(34): p. 18294-18300.

[22] Cussen, E.J., *Structure and ionic conductivity in lithium garnets.* Journal of Materials Chemistry, 2010. **20**(25): p. 5167-5173.

[23] Janani, N., Ramakumar, S., Dhivya, L., Deviannapoorani, C., Saranya, K., and Murugan, R., *Synthesis of cubic $Li_7La_3Zr_2O_{12}$ by modified sol–gel process.* Ionics, 2011. **17**(7): p. 575-580.

[24] Awaka, J., Kijima, N., Hayakawa, H., and Akimoto, J., *Synthesis and structure analysis of tetragonal $Li_7La_3Zr_2O_{12}$ with the garnet-related type structure.* Journal of Solid State Chemistry, 2009. **182**(8): p. 2046-2052.

[25] Murugan, R., Thangadurai, V., and Weppner, W., *Fast lithium ion conduction in garnet-type $Li_7La_3Zr_2O_{12}$.* Angewandte Chemie-International Edition, 2007. **46**(41): p. 7778-7781.

[26] Rangasamy, E., Wolfenstine, J., and Sakamoto, J., *The role of Al and Li concentration on the formation of cubic garnet solid electrolyte of nominal composition $Li_7La_3Zr_2O_{12}$.* Solid State Ionics, 2012. **206**: p. 28-32.

[27] Cheng, L., Park, J.S., Hou, H.M., Zorba, V., Chen, G.Y., Richardson, T., Cabana, J., Russo, R., and Doeff, M., *Effect of microstructure and surface impurity segregation on the electrical and electrochemical properties of dense Al-substituted $Li_7La_3Zr_2O_{12}$.* Journal of Materials Chemistry A, 2014. **2**(1): p. 172-181.

[28] Fuglein, E. and Walter, D., *Thermal analysis of lanthanum hydroxide.* Journal of Thermal Analysis and Calorimetry, 2012. **110**(1): p. 199-202.

[29] Ren, Y.Y., Deng, H., Chen, R.J., Shen, Y., Lin, Y.H., and Nan, C.W., *Effects of Li source on microstructure and ionic conductivity of Al-contained $Li_{6.75}La_3Zr_{1.75}Ta_{0.25}O_{12}$ ceramics.* Journal of the European Ceramic Society, 2015. **35**(2): p. 561-572.

[30] Kotobuki, M., Munakata, H., Kanamura, K., Sato, Y., and Yoshida, T., *Compatibility of $Li_7La_3Zr_2O_{12}$ Solid Electrolyte to All-Solid-State Battery Using Li Metal Anode.* Journal of The Electrochemical Society, 2010. **157**(10): p. A1076-A1079.

[31] Sakamoto, J., Rangasamy, E., Kim, H., Kim, Y., and Wolfenstine, J., *Synthesis of nano-scale fast ion conducting cubic $Li_7La_3Zr_2O_{12}$.* Nanotechnology, 2013. **24**(42): p. 424005.

[32] Bai, L.X., Xue, W.D., Li, Y., Liu, X.G., Li, Y., and Sun, J.L., *The surface behaviour of an Al-$Li_7La_3Zr_2O_{12}$ solid electrolyte.* Ceramics International, 2017. **43**(17): p. 15805-15810.

[33] Yang, C., Yi-Qiu, L., and Xiang-Xin, G., *Densification and lithium ion conductivity of garnet-type $Li_{7-x}La_3Zr_{2-x}Ta_xO_{12}$ (x= 0.25) solid electrolytes.* Chinese Physics B, 2013. **22**(7): p. 078201.

[34] Rao, R.P., Gu, W.Y., Sharma, N., Peterson, V.K., Avdeev, M., and Adams, S., *In Situ Neutron Diffraction Monitoring of $Li_7La_3Zr_2O_{12}$ Formation: Toward a Rational Synthesis of Garnet Solid Electrolytes.* Chemistry of Materials, 2015. **27**(8): p. 2903-2910.

[35] Yang, X., Kong, D., Chen, Z., Sun, Y., and Liu, Y., *Low-temperature fabrication for transparency Mg doping $Li_7La_3Zr_2O_{12}$ solid state electrolyte.* Journal of Materials Science: Materials in Electronics, 2017: p. 1-7.

[36] Rettenwander, D., Geiger, C.A., and Amthauer, G., *Synthesis and Crystal Chemistry of the Fast Li-Ion Conductor $Li_7La_3Zr_2O_{12}$ Doped with Fe.* Inorganic Chemistry, 2013. **52**(14): p. 8005-8009.

[37] Li, C.L., Liu, Y.F., He, J., and Brinkman, K.S., *Ga-substituted $Li_7La_3Zr_2O_{12}$: An investigation based on grain coarsening in garnet-type lithium ion conductors.* Journal of Alloys and Compounds, 2017. **695**: p. 3744-3752.

[38] Larraz, G., Orera, A., and Sanjuán, M.L., *Cubic phases of garnet-type $Li_7La_3Zr_2O_{12}$: the role of hydration.* Journal of Materials Chemistry A, 2013. **1**(37): p. 11419.

[39] Bachman, J.C., Muy, S., Grimaud, A., Chang, H.H., Pour, N., Lux, S.F., Paschos, O., Maglia, F., Lupart, S., Lamp, P., Giordano, L., and Shao-Horn, Y., *Inorganic Solid-State Electrolytes for Lithium Batteries: Mechanisms and Properties Governing Ion Conduction.* Chemical Reviews, 2016. **116**(1): p. 140-162.

[40] Angulakshmi, N., Yoo, D.J., Nahm, K.S., Gerbaldi, C., and Stephan, A.M., *$MgAl_2SiO_6$-incorporated poly(ethylene oxide)-based electrolytes for all-solid-state lithium batteries.* Ionics, 2014. **20**(2): p. 151-156.

[41] Bates, A., Mukherjee, S., Schuppert, N., Son, B., Kim, J.G., and Park, S., *Modeling and simulation of 2D lithium-ion solid state battery.* International Journal of Energy Research, 2015. **39**(11): p. 1505-1518.

[42] Tan, J.J. and Tiwari, A., *Synthesis of Cubic Phase $Li_7La_3Zr_2O_{12}$ Electrolyte for Solid-State Lithium-Ion Batteries.* Electrochemical and Solid State Letters, 2012. **15**(3): p. A37-A39.

[43] Murugan, R., Ramakumar, S., and Janani, N., *High conductive yttrium doped $Li_7La_3Zr_2O_{12}$ cubic lithium garnet.* Electrochemistry Communications, 2011. **13**(12): p. 1373-1375.

[44] Ahn, J.H., Park, S.Y., Lee, J.M., Park, Y., and Lee, J.H., *Local impedance spectroscopic and microstructural analyses of Al-in-diffused $Li_7La_3Zr_2O_{12}$.* Journal of Power Sources, 2014. **254**: p. 287-292.

[45] Chen, R.J., Huang, M., Huang, W.Z., Shen, Y., Lin, Y.H., and Nan, C.W., *Effect of calcining and Al doping on structure and conductivity of $Li_7La_3Zr_2O_{12}$.* Solid State Ionics, 2014. **265**: p. 7-12.

[46] Dermenci, K.B., Cekic, E., and Turan, S., *Al stabilized $Li_7La_3Zr_2O_{12}$ solid electrolytes for all-solid state Li-ion batteries.* International Journal of Hydrogen Energy, 2016. **41**(23): p. 9860-9867.

[47] Chen, Y., Rangasamy, E., dela Cruz, C.R., Liang, C.D., and An, K., *A study of suppressed formation of low-conductivity phases in doped $Li_7La_3Zr_2O_{12}$ garnets by in situ neutron diffraction.* Journal of Materials Chemistry A, 2015. **3**(45): p. 22868-22876.

[48] Düvel, A., Kuhn, A., Robben, L., Wilkening, M., and Heitjans, P., *Mechanosynthesis of Solid Electrolytes: Preparation, Characterization, and Li Ion Transport Properties of Garnet-Type Al-Doped $Li_7La_3Zr_2O_{12}$ Crystallizing with Cubic Symmetry*. The Journal of Physical Chemistry C, 2012. **116**(29): p. 15192-15202.

[49] Hitz, G.T., Wachsman, E.D., and Thangadurai, V., *Highly Li-Stuffed Garnet-Type $Li_{7+x}La_3Zr_{2-x}Y_xO_{12}$.* Journal of the Electrochemical Society, 2013. **160**(8): p. A1248-A1255.

[50] Deviannapoorani, C., Ramakumar, S., Janani, N., and Murugan, R., *Synthesis of lithium garnets from $La_2Zr_2O_7$ pyrochlore.* Solid State Ionics, 2015. **283**: p. 123-130.

[51] Kumar, P.J., Nishimura, K., Senna, M., Duvel, A., Heitjans, P., Kawaguchi, T., Sakamoto, N., Wakiya, N., and Suzuki, H., *A novel low-temperature solid-state*

route for nanostructured cubic garnet $Li_7La_3Zr_2O_{12}$ and its application to Li-ion battery. Rsc Advances, 2016. **6**(67): p. 62656-62667.

[52] Rettenwander, D., Welzl, A., Cheng, L., Fleig, J., Musso, M., Suard, E., Doeff, M.M., Redhammer, G.J., and Amthauer, G., *Synthesis, Crystal Chemistry, and Electrochemical Properties of $Li_{7-2x}La_3Zr_{2-x}Mo_xO_{12}$ (x=0.1-0.4): Stabilization of the Cubic Garnet Polymorph via Substitution of Zr^{4+} by Mo^{6+}*. Inorganic Chemistry, 2015. **54**(21): p. 10440-10449.

[53] Kunc, K., Loa, I., Grzechnik, A., and Syassen, K., *Li_2O at high pressures: structural properties, phase-transition, and phonons.* Physica Status Solidi B-Basic Solid State Physics, 2005. **242**(9): p. 1857-1863.

[54] Raskovalov, A.A., Il'ina, E.A., and Antonov, B.D., *Structure and transport properties of $Li_7La_3Zr_{2-0.75x}Al_xO_{12}$ superionic solid electrolytes.* Journal of Power Sources, 2013. **238**: p. 48-52.

[55] Cheng, E.J., Sharafi, A., and Sakamoto, J., *Intergranular Li metal propagation through polycrystalline $Li_{6.25}Al_{0.25}La_3Zr_2O_{12}$ ceramic electrolyte.* Electrochimica Acta, 2017. **223**: p. 85-91.

[56] Sahu, G., Rangasamy, E., Li, J.C., Chen, Y., An, K., Dudney, N., and Liang, C.D., *A high-conduction Ge substituted Li_3AsS_4 solid electrolyte with exceptional low activation energy.* Journal of Materials Chemistry A, 2014. **2**(27): p. 10396-10403.

[57] Jung, Y.-C., Kim, S.-K., Kim, M.-S., Lee, J.-H., Han, M.-S., Kim, D.-H., Shin, W.-C., Ue, M., and Kim, D.-W., *Ceramic separators based on Li^+-conducting inorganic electrolyte for high-performance lithium-ion batteries with enhanced safety.* Journal of Power Sources, 2015. **293**: p. 675-683.

[58] Ramakumar, S., Deviannapoorani, C., Dhivya, L., Shankar, L.S., and Murugan, R., *Lithium garnets: Synthesis, structure, Li^+ conductivity, Li^+ dynamics and applications.* Progress in Materials Science, 2017. **88**: p. 325-411.

[59] Han, X., Gong, Y., Fu, K.K., He, X., Hitz, G.T., Dai, J., Pearse, A., Liu, B., Wang, H., and Rubloff, G., *Negating interfacial impedance in garnet-based solid-state Li metal batteries.* Nature materials, 2017. **16**(5): p. 572.

[60] Li, Y., Wang, Z., Li, C., Cao, Y., and Guo, X., *Densification and ionic-conduction improvement of lithium garnet solid electrolytes by flowing oxygen sintering.* Journal of Power Sources, 2014. **248**: p. 642-646.

[61] Hanc, E., Zajac, W., Lu, L., Yan, B.G., Kotobuki, M., Ziabka, M., and Molenda, J., *On fabrication procedures of Li-ion conducting garnets.* Journal of Solid State Chemistry, 2017. **248**: p. 51-60.

[62] Kudela, S., Oswald, S., Kudela, S., Baunack, S., and Wetzig, K., *The ion exchange promoted interfacial strength in magnesium based composites.* Journal of Alloys and Compounds, 2004. **378**(1-2): p. 127-131.

[63] Wang, P.C., Shih, Y.T., Lin, M.C., Lin, H.C., Chen, M.J., and Lin, K.M., *Improvement of wear and cavitation-erosion by ALD-deposited $LiAl_xO_y$ films on an Mg-10Li-0.5Zn alloy.* Surface & Coatings Technology, 2010. **204**(21-22): p. 3707-3712.

[64] Chang, T.C., Wang, J.Y., Chu, C.L., and Lee, S., *Mechanical properties and microstructures of various Mg-Li alloys.* Materials Letters, 2006. **60**(27): p. 3272-3276.

[65] Fanovich, M.A. and Lopez, J.M.P., *Influence of temperature and additives on the microstructure and sintering behaviour of hydroxyapatites with different Ca/P ratios.* Journal of Materials Science-Materials in Medicine, 1998. **9**(1): p. 53-60.

[66] Kamitsos, E.I., Patsis, A.P., Karakassides, M.A., and Chryssikos, G.D., *Infrared Reflectance Spectra of Lithium Borate Glasses.* Journal of Non-Crystalline Solids, 1990. **126**(1-2): p. 52-67.

[67] Daou, K., Wang, R.Z., and Xia, Z.Z., *Desiccant cooling air conditioning: a review.* Renewable & Sustainable Energy Reviews, 2006. **10**(2): p. 55-77.

[68] Hackney, S.A., *Li-Ion Cathodes: Materials Engineering through Chemistry*, in *High Energy Density Lithium Batteries*. 2010, Wiley-VCH Verlag GmbH & Co. KGaA. p. 103-127.

[69] Oshima, Y., *The special issue of Microscopy on challenges for lithium detection.* Microscopy, 2017. **66**(1): p. 1-2.

[70] Findlay, S.D., Huang, R., Ishikawa, R., Shibata, N., and Ikuhara, Y., *Direct visualization of lithium via annular bright field scanning transmission electron microscopy: a review.* Microscopy, 2017. **66**(1): p. 3-14.

[71] Ma, C. and Chi, M.F., *Novel Solid Electrolytes for Li-Ion Batteries: A Perspective from Electron Microscopy Studies.* Frontiers in Energy Research, 2016. **4**.

[72] Brunetti, G., Robert, D., Bayle-Guillemaud, P., Rouviere, J.L., Rauch, E.F., Martin, J.F., Colin, J.F., Bertin, F., and Cayron, C., *Confirmation of the Domino-Cascade Model by $LiFePO_4/FePO_4$ Precession Electron Diffraction.* Chemistry of Materials, 2011. **23**(20): p. 4515-4524.

[73] Hadermann, J., Abakumov, A.M., Turner, S., Hafideddine, Z., Khasanova, N.R., Antipov, E.V., and Van Tendeloo, G., *Solving the Structure of Li Ion Battery Materials with Precession Electron Diffraction: Application to Li_2CoPO_4F.* Chemistry of Materials, 2011. **23**(15): p. 3540-3545.

[74] Terauchi, M., Koshiya, S., Satoh, F., Takahashi, H., Handa, N., Murano, T., Koike, M., Imazono, T., Koeda, M., Nagano, T., Sasai, H., Oue, Y., Yonezawa, Z., and Kuramoto, S., *Chemical State Information of Bulk Specimens Obtained by SEM-Based Soft-X-Ray Emission Spectrometry.* Microscopy and Microanalysis, 2014. **20**(3): p. 692-697.

[75] Brodusch, N., Zaghib, K., and Gauvin, R., *Electron Backscatter Diffraction Applied to Lithium Sheets Prepared by Broad Ion Beam Milling.* Microscopy Research and Technique, 2015. **78**(1): p. 30-39.

[76] Yabuuchi, N., Yoshii, K., Myung, S.T., Nakai, I., and Komaba, S., *Detailed Studies of a High-Capacity Electrode Material for Rechargeable Batteries, Li_2MnO_3-$LiCo_{1/3}Ni_{1/3}Mn_{1/3}O_2$.* Journal of the American Chemical Society, 2011. **133**(12): p. 4404-4419.

[77] Lee, J.T., Nitta, N., Benson, J., Magasinski, A., Fuller, T.F., and Yushin, G., *Comparative study of the solid electrolyte interphase on graphite in full Li-ion battery cells using X-ray photoelectron spectroscopy, secondary ion mass spectroscopy, and electron microscopy (vol 52, pg 388, 2013).* Carbon, 2013. **56**: p. 397-398.

[78] Ota, H., Akai, T., Namita, H., Yamaguchi, S., and Nomura, M., *XAFS and TOF-SIMS analysis of SEI layers on electrodes.* Journal of Power Sources, 2003. **119**: p. 567-571.

[79] Sui, T., Song, B.H., Dluhos, J., Lu, L., and Korsunsky, A.M., *Nanoscale chemical mapping of Li-ion battery cathode material by FIB-SEM and TOF-SIMS multi-modal microscopy.* Nano Energy, 2015. **17**: p. 254-260.

[80] Karen, A., Ito, K., and Kubo, Y., *TOF-SIMS analysis of lithium air battery discharge products utilizing gas cluster ion beam sputtering for surface stabilization.* Surface and Interface Analysis, 2014. **46**: p. 344-347.

[81] Loho, C., Djenadic, R., Bruns, M., Clemens, O., and Hahn, H., *Garnet-Type $Li_7La_3Zr_2O_{12}$ Solid Electrolyte Thin Films Grown by CO_2-Laser Assisted CVD for All-Solid-State Batteries.* Journal of The Electrochemical Society, 2017. **164**(1): p. A6131-A6139.

[82] Song, M.S., Kim, R.H., Baek, S.W., Lee, K.S., Park, K., and Benayad, A., *Is $Li_4Ti_5O_{12}$ a solid-electrolyte-interphase-free electrode material in Li-ion batteries? Reactivity between the $Li_4Ti_5O_{12}$ electrode and electrolyte.* Journal of Materials Chemistry A, 2014. **2**(3): p. 631-636.

[83] Wang, D.W., Zhong, G.M., Dolotko, O., Li, Y.X., McDonald, M.J., Mi, J.X., Fu, R.Q., and Yang, Y., *The synergistic effects of Al and Te on the structure and Li^+-mobility of garnet-type solid electrolytes.* Journal of Materials Chemistry A, 2014. **2**(47): p. 20271-20279.

[84] Bassim, N., Scott, K., and Giannuzzi, L.A., *Recent advances in focused ion beam technology and applications.* Mrs Bulletin, 2014. **39**(4): p. 317-325.

[85] Kamaya, N., Homma, K., Yamakawa, Y., Hirayama, M., Kanno, R., Yonemura, M., Kamiyama, T., Kato, Y., Hama, S., Kawamoto, K., and Mitsui, A., *A lithium superionic conductor.* Nat Mater, 2011. **10**(9): p. 682-6.

[86] David, I.N., Thompson, T., Wolfenstine, J., Allen, J.L., and Sakamoto, J., *Microstructure and Li-Ion Conductivity of Hot- Pressed Cubic $Li_7La_3Zr_2O_{12}$.* Journal of the American Ceramic Society, 2015. **98**(4): p. 1209-1214.

[87] Inada, R., Kusakabe, K., Tanaka, T., Kudo, S., and Sakurai, Y., *Synthesis and properties of Al-free $Li_{7-x}La_3Zr_{2-x}Ta_xO_{12}$ garnet related oxides.* Solid State Ionics, 2014. **262**: p. 568-572.

[88] Jin, Y. and McGinn, P.J., *$Li_7La_3Zr_2O_{12}$ electrolyte stability in air and fabrication of a $Li/Li_7La_3Zr_2O_{12}/Cu_{0.1}V_2O_5$ solid-state battery.* Journal of Power Sources, 2013. **239**: p. 326-331.

[89] Shimonishi, Y., Toda, A., Zhang, T., Hirano, A., Imanishi, N., Yamamoto, O., and Takeda, Y., *Synthesis of garnet-type $Li_{7-x}La_3Zr_2O_{12-1/2x}$ and its stability in aqueous solutions.* Solid State Ionics, 2011. **183**(1): p. 48-53.

[90] Langer, F., Glenneberg, J., Bardenhagen, I., and Kun, R., *Synthesis of single phase cubic Al-substituted $Li_7La_3Zr_2O_{12}$ by solid state lithiation of mixed hydroxides.* Journal of Alloys and Compounds, 2015. **645**: p. 64-69.

[91] Wolfenstine, J., Rangasamy, E., Allen, J.L., and Sakamoto, J., *High conductivity of dense tetragonal $Li_7La_3Zr_2O_{12}$.* Journal of Power Sources, 2012. **208**: p. 193-196.

[92] Jin, Y. and McGinn, P., *Al-doped $Li_7La_3Zr_2O_{12}$ synthesized by a polymerized complex method.* Journal of Power Sources, 2011. **196**(20): p. 8683-8687.

[93] Rosenkiewitz, N., Schuhmacher, J., Bockmeyer, M., and Deubener, J., *Nitrogen-free sol-gel synthesis of Al-substituted cubic garnet $Li_7La_3Zr_2O_{12}$ (LLZO).* Journal of Power Sources, 2015. **278**: p. 104-108.

[94] Choy, J.H., Yoon, J.B., and Park, J.H., *In situ XAFS study at the Zr K-edge for SiO_2/ZrO_2 nano-sol.* Journal of Synchrotron Radiation, 2001. **8**: p. 782-784.

[95] Liu, Q.H., Wang, C.X., Qu, W., Wang, B.C., Tian, Z.J., Ma, H.J., and Xu, R.S., *The application of Zr incorporated Zn-Al dehydrated hydrotalcites as solid base in transesterification.* Catalysis Today, 2014. **234**: p. 161-166.

[96] Lu, J., Li, Y., and Deng, C.H., *Facile synthesis of zirconium phosphonate-functionalized magnetic mesoporous silica microspheres designed for highly selective enrichment of phosphopeptides.* Nanoscale, 2011. **3**(3): p. 1225-1233.

[97] Chang, Y.-C., Lee, M.-C., Kao, W.-X., Lin, T.-N., and The American Ceramic, S., *Preparation of a Nanoscale/SOFC-Grade Yttria-Stabilized Zirconia Material: A Quasi-Optimization of the Hydrothermal Coprecipitation Process,* in *Progress in Nanotechnology*. 2009, John Wiley & Sons, Inc. p. 13-23.

[98] Kanno, Y., *Stability of Metastable Tetragonal ZrO_2 in Compound Powders and Nucleation Arguments.* Journal of Materials Science, 1990. **25**(4): p. 1987-1990.

[99] Irvine, J.T., Sinclair, D.C., and West, A.R., *Electroceramics: characterization by impedance spectroscopy.* Advanced Materials, 1990. **2**(3): p. 132-138.

[100] Pirovano, C., Rolle, A., and Vannier, R.-N., *Perovskite and Derivative Compounds as Mixed Ionic–Electronic Conductors.* Perovskites and Related Mixed Oxides: Concepts and Applications, 2015.